UNIVERSITY OF OKLAHOMA

GRADUATE COLLEGE

EXAMINING ENVIRONMENTAL CONDITIONS, STORM-SCALE CHARACTERISTICS, AND TORNADO POTENTIAL IN OBSERVED AND SIMULATED SUPERCELL THUNDERSTORMS

A DISSERTATION

SUBMITTED TO THE GRADUATE FACULTY

in partial fulfillment of the requirements for the

Degree of

DOCTOR OF PHILOSOPHY

By

MATTHEW DOUGLAS FLOURNOY
Norman, Oklahoma
2020

EXAMINING ENVIRONMENTAL CONDITIONS, STORM-SCALE CHARACTERISTICS, AND TORNADO POTENTIAL IN OBSERVED AND SIMULATED SUPERCELL THUNDERSTORMS

A DISSERTATION APPROVED FOR THE
SCHOOL OF METEOROLOGY

BY THE COMMITTEE CONSISTING OF

Dr. Michael Coniglio, Chair

Dr. Erik Rasmussen

Dr. Cameron Homeyer

Dr. Michael Biggerstaff

Dr. Xuguang Wang

Dr. Carol Silva

Acknowledgments

My journey to the PhD was anything but a solo mission. Hundreds of people supported me along the way both professionally and personally. I will do my best to thank these people here in what will surely be an incomplete list. To all those mentioned here and all those that are not: thank you. I could not have done this without you.

First I thank my advisors, Michael Coniglio and Erik Rasmussen, who have somehow managed to put up with me for the last five years in graduate school. You both have supported me in many ways, including navigating the graduate program, participating in field work, and my involvement in outreach and volunteer activities, to name a few. From you I learned how to conduct independent research, use different analysis techniques, create and lead a field mission, and balance work and personal life. Most importantly, I learned how to be a scientist. Thank you for supporting me during this entire process.

Thank you to many others who professionally helped me along the way, including my committee members: Carol Silva, Cameron Homeyer, Xuguang Wang, and Michael Biggerstaff. Your guidance and support have been helpful in completing the research and writing that went into this dissertation. To Kent Knopfmeier, Brett Roberts, Jordan Laser, and especially Burkely Gallo, thank you for making the Hall of Science a fun and productive work environment. Thank you also to Adam Clark, Jens Redemann, and Jeff Basara for your professional guidance and being an outlet for my passion for football (not the American version). Thanks are due to many other faculty and associates of the School of Meteorology during the past few years, in particular Elinor Martin, Evgeni Fedorovich, Howie Bluestein, Jason Furtado, Petra Klein, Steven Cavallo, Alan Shapiro, Lans Rothfusz, Harold Brooks, Pam Heinselman, Elizabeth Smith, Steve Koch, Lou Wicker, Conrad Ziegler, and Robert Coggins. Graduate school is always challenging, but you all made it an enjoyable one, too. Thank you for your professional support of my coursework, teaching positions, outreach activities, and research ideas.

Thank you to the staff of the School of Meteorology, Cooperative Institute for Mesoscale Meteorological Studies, and National Severe Storms Laboratory. Christie Upchurch, it is difficult to express how much I appreciated your insight during graduate school, relating to anything from which courses to enroll in to how to attend different conferences to attaining a work-life balance and many other personal matters. You went to infinity and well-beyond in your role as the Coordinator of Graduate Programs for me and every graduate student. Thank you for that. Thank you also to Shelby Hill for your support, whether it be buying bedding for all of us when we travelled to Reading or my involvement in addressing student fees and the School of Meteorology website. I also thank Debbie Barnhill, Nancy Campbell, Julie Dahlgren, and Shawn Riley for your help in dealing with financial matters, room assignments, scheduling meetings, and technical issues. Thank you to Tracy Reinke, Tanya Riley, and Jamie Foucher for your assistance in any and all CIMMS matters, even when I was not technically affiliated with CIMMS. Thank you also to Ryan Hastings for providing the pressure decomposition code used in the first part of this dissertation.

Thank you especially to my friends and peers. In my best attempt to remain concise but comprehensive, this includes Addison Alford, Rachel Miller, Andy and Heather Wade, Drew Rickels, Kristen Perez-Rickels, Josh and Kat Gebauer, Allie Brannan, Jackson Anthony, Sean Ernst, Michael and Shannon Johnson, Blake and Emily Kuenzi, Preston Rothfusz, Mel Redemann, Mike Lowe, and Matt Gropp. Thank you to each of you and many others for your friendship. Your personal support made my professional success in graduate school possible.

Lastly, thank you to my family. Lori and Doug, do you remember the day that I looked up and pointed out the cloud in the sky that looked like a piano? Well, I still like clouds and I still like playing the piano, so that all worked out. It worked out because you two never stopped supporting me all of those years, and for that I will be forever grateful. Dave and Amy, thank you for being there for me for all but 1.5 years of my life. Thank you also to Nana, Phil, Edie, and Leslie. To Nancy, Bob, Maddie, and Sean, thank you for

letting me join the club. I felt like family from the first time Kenzie and I drove home to visit, and I hope to one day convey just how much that meant to me.

Finally, thank you to Kenzie Krocak, my partner and better half. You are an incredible person and an incredible scientist, and I cherish these and many other aspects of our relationship. Thank you for always chasing adventure, dreams, and happiness with me. We have some rolled up maps and PhDs in meteorology, what more could we need?

Table of Contents

List of Figures

Abstract

Despite advancements in our understanding of supercell thunderstorms, numerous questions remain regarding relationships between their environment, storm-scale characteristics, and tornado potential. In particular, quantifying the range of storms possible in a given environment is an active area of research, and examining these relationships in time remains even more unexplored. This dissertation addresses these two research foci using a blend of numerical modelling and observational analysis.

First, two 15-member ensembles of high-resolution, idealized simulations are conducted to explore the sensitivity of supercellular tornado production to small, storm-scale variations. The composite near- and far-field tornadic VORTEX2 profiles (Parker 2014) are used as the base-state for each of these two ensembles. Within each environment, the initial wind profile is perturbed slightly, resulting in 15 slightly different storms evolving within each environment. Based on my definition of a "tornado" in the simulation, all members in the near-field environment produce a tornado while only 40% of those in the far-field environment produce a tornado. Important storm-scale characteristics differ between the two ensembles, especially in terms of low-level updraft strength and surface outflow temperature. These results also show that storm-environment modifications can result in a local environment much more supportive of tornado potential.

Next, an observational dataset consisting of 902 soundings and 220 supercell tracks is analyzed to better understand storm-track characteristics, particularly related to the right turn, and their relationship to environmental conditions. No significant correlations were found between the environmental parameters examined here and the time of the right turn. However, larger values of 0–1 km AGL streamwise horizontal vorticity magnitude (e.g., > 0.010–$0.015\ s^{-1}$) tended to coincide with cells turning right within the first 65 minutes of their lifetime, and vice versa for smaller values of streamwise horizontal vorticity. The mean time between the cell's first appearance on radar and the right turn was around 45 minutes for all supercells with a standard deviation of 25–30 minutes. Mean streamwise

horizontal vorticity was significantly larger in the tornadic environments in the 0–1 and 0–3 km AGL layers, but not the 0–0.5 km AGL layer. Interestingly, mean crosswise horizontal vorticity was not significantly different between the tornadic and nontornadic subsets.

A goal of this work was to identify relationships and/or processes linking environmental conditions to supercell characteristics that may be relevant to real-time forecasters, either immediately or in the near-future. Some conclusions from this work that are relevant to this goal include further quantifying what range of storms, in terms of tornado production, are possible in different environments and mean statistics regarding characteristics of the right turn in supercells. Future work will continue to use a blend of analysis methods to further examine supercell environments, storm-scale characteristics, and tornado potential in ways that will most efficiently benefit operational forecasting, emergency management, and other audiences.

Chapter 1

Introduction

Uncovering the secrets of tornadogenesis has been a "Holy Grail" in the severe weather community since the first tornado forecast was issued for Tinker Air Force Base in Oklahoma County, Oklahoma on 25 March 1948 (Doswell III et al. 1999). Since then, the community has made significant progress on multiple fronts with regards to better protecting life and property during tornado events. Through laboratory experiments, evolving observing systems, theoretical studies, and high-resolution computer simulations, scientists have uncovered processes influencing supercells and tornadoes on various atmospheric scales. These findings have aided operational forecasters in better predicting severe weather events from minutes to days in advance and issuing products for a variety of audiences. These aid broadcast meteorologists and others in informing the public and help local emergency managers and personnel prepare for upcoming severe weather events.

However, many questions remain regarding how supercell tornadoes form, are maintained, and decay, what observing systems are required to best anticipate their occurrence minutes to days in advance, how to coordinate modelling efforts to focus on processes relevant to protect lives and property, how to synthesize these findings and make them useful for the operational forecaster in a stressful, real-time setting, and how to efficiently convey this information to the public, just to name a few.

This dissertation focuses on better understanding supercellular evolution and tornado potential in different environments in the central U.S. Both numerical model output and observations are analyzed to address this focus. High-resolution idealized modelling is used to simulate supercell evolution and tornado production and examine their sensitivity to very small changes in environmental conditions. What ranges of storm-scale characteristics and vortex production are possible in certain environments? This question is the

primary focus of this modelling work. Next, over 900 soundings collected during past field campaigns from 1994–2019 are analyzed to better understand supercell environments and their influences on storm morphology. Exploring relationships between environmental conditions and supercell track characteristics, like the initial cell motion, time of the right turn and (if relevant) tornadogenesis, storm acceleration during the right turn, etc., is the primary focus of this observational study. Ultimately, this work yields insight into factors influencing supercell evolution and tornado potential and is relevant to operational forecasters in better predicting storm morphology and hazards in real-time.

1.0.1 Research background

The first schematics of airflow within supercell thunderstorms arose from observational analysis of the severe Wokingham hailstorm in England (Browning and Ludlam 1962). Several years and many radar, surface, and sounding observations later, Lemon and Doswell III (1979) produced a schematic of surface supercell characteristics that is still used today (Lemon and Doswell III 1979; their Fig. 7). This conceptual model features a central, rotating storm updraft ("UP") flanked by rear- and forward-flank downdrafts ("RFD" and "FFD"). Storm-scale boundaries demarcating regions of storm-cooled air and warmer environmental inflow are shown, along with the location of the possible tornado at the inflection point of the surface boundaries near the back edge of the main updraft. In the present day, small modifications to this schematic might include neglecting the FFD boundary on the eastern extent of the storm. Otherwise, this conceptual model of surface airflow within supercells remains mostly unchanged.

Since then, theoretical work and advancements in numerical modeling and observing capabilities have greatly improved our understanding of processes influencing supercell morphology and tornado potential, especially related to environmental conditions. Given

discrete convection initiation, supercell formation is expected if the background environment contains sufficient convective available potential energy (CAPE; $\geq$ 1000 J kg^{-1}), vertical wind shear (0–6 km AGL shear $\geq$ 15–20 m s^{-1}), and 0–3 km storm-relative helicity (SRH; $\geq$ 100 m^2 s^{-2}). These general thresholds (not met stringently in all cases) have been found in multiple studies analyzing soundings in the vicinity of supercells (e.g., Rasmussen and Blanchard 1998; Thompson et al. 2003; Craven et al. 2004). The physical processes driving these relationships have been well explored. For example, increased SRH is associated with greater streamwise horizontal vorticity, resulting in greater vertical vorticity tendencies via tilting (e.g., Lilly 1982; Weisman and Klemp 1982; Davies-Jones 1984; Lilly 1986), and greater storm-relative flow, promoting wider updrafts (Peters et al. 2019) and limiting the deleterious effects of hydrometeor loading and entrainment (Peters et al. 2019; Peters et al. 2020). Greater CAPE values also yield greater vertical accelerations due to buoyancy that, although partially compensated by downward-directed buoyant pressure perturbation gradients, increase updraft speeds.

Environmental conditions and forecast parameters like these are used daily by forecasters to predict supercell occurrence and associated hazards. However, less is known about how these conditions influence supercell morphology *in time*. A few studies have examined how changes in the background environment result in changes in supercell characteristics, including the effects of horizontally varying vertical wind shear (Richardson et al. 2007; Davenport and Parker 2015; Gropp and Davenport 2018), a developing stable layer near the surface (Ziegler et al. 2010; Coffer and Parker 2015), and differences in SRH (Klees et al. 2016)). Bluestein and Parker (1993) analyzed the life cycles of supercells forming along the dryline in the central U.S. and found that, on average, roughly two hours passed between convective initiation and the time of the first severe weather occurrence. Supercell morphology during this developmental phase remains a largely unexplored topic.

Certain storm-scale characteristics are known to strongly influence supercellular tornado potential, including a strong, low-level, rotating updraft, near-surface rotation, and

significant intensification of that rotation to tornadic intensity at the surface (Davies-Jones 2015). The formation of the rotating updraft aloft, or mesocyclone (Glickman and Walter 2000), is perhaps best understood. Horizontal vorticity in the near-storm environment is tilted into the vertical and stretched by a convective updraft (Rotunno 1981; Lilly 1982; Davies-Jones 1984; Dahl 2017) to form the mid-level mesocyclone. A similar process is responsible for the formation of the low-level mesocyclone based on observational (Markowski et al. 2012a) and modeling studies (e.g., Markowski and Richardson 2014; Coffer and Parker 2017), augmented to some degree by baroclinic generation within the storm (e.g., Klemp and Rotunno 1983; Rotunno and Klemp 1985).

Regarding the initial development of near-surface vertical vorticity, it appears that many supercells (both tornadic and nontornadic) contain similar surface characteristics, including kinematic fields like vorticity (e.g., Trapp et al. 1999; Wakimoto and Cai 2000; Markowski et al. 2011). Given that the only requirements for near-surface vertical vorticity production are a downdraft and downdraft-relative horizontal flow (Parker and Dahl 2015), it is likely that near-surface vertical vorticity is present in most if not all supercells. The emerging theory is thus not entirely focused on how that vorticity forms but whether or not the supercell will act on it "enough" to produce a tornado.

In the final moments preceding tornadogenesis, an intense low-level updraft is required to stretch near-surface vertical vorticity to tornadic intensity. This stretching is a function of both the density (or buoyancy) of the outflow air within which said vertical vorticity resides as well as the strength of the low-level updraft. To this degree, tornadic supercells generally contain warmer outflow than nontornadic supercells (e.g., Markowski et al. 2002; Grzych et al. 2007; Hirth et al. 2008). Warmer outflow is favored in environments with higher boundary-layer humidity (Rasmussen and Blanchard 1998; Rasmussen 2003; Thompson et al. 2003; Craven et al. 2004) owing to less evaporational cooling (Kumjian 2011; French et al. 2015). Increased boundary-layer humidity also tends to lower the level of free convection, strengthening low-level updraft speeds. Recent work has also shown that larger

streamwise horizontal vorticity nearer to the surface (e.g., 0–500 m AGL) favors steadier, more robust low-level updrafts (e.g., Coffer and Parker 2017). This is consistent with prior studies of observed soundings near tornadic and nontornadic supercells (Thompson and Edwards 2000; Esterheld and Giuliano 2008).

However, both tornadic and nontornadic supercells often coexist in closer proximity to each other (e.g., Klees et al. 2016; Markowski and Richardson 2017). On other days, it seems that nearly every supercell that forms produces a tornado. This shows that supercellular tornado potential is a function of background environmental conditions as well as intra-storm characteristics. Coffer et al. (2017) simulated several idealized supercells in composite tornadic and nontornadic environments sampled during the second Verification of the Origins of Rotation in Tornadoes Experiment (VORTEX2; Wurman et al. 2012) and found the tornadic environment to support tornado production every time while the nontornadic environment supported tornado production 40 % of the time. This difference in tornado production was attributed to larger low-level SRH in the tornadic environment, promoting stronger, more robust low-level updrafts. In light of these findings, what other conditions may support more or less consistent tornado production within a given environment? How do storm-environment modifications (e.g., Parker 2014; Nowotarski and Markowski 2016; Wade et al. 2018; con) influence the volatility of tornadogenesis? Answering questions like these will better our understanding of supercell morphology, tornado potential, and the physical processes associated with these relationships.

1.0.2 Research questions

This work addresses ongoing questions regarding supercell morphology and tornado potential in different environments common in the central U.S. These include the following:

- What patterns of variability in storm characteristics and tornado potential exist between storms forming in essentially the same environment?

- Is the volatility of tornadogenesis different in the near- and far-field VORTEX2 environments?

- If so, what drives differences in the volatility of tornadogenesis in these environments?

- How long does it take for a developing supercell to turn right? How is this timescale influenced by environmental characteristics?

- Is the initial cell motion (prior to the right turn) generally aligned with the mean wind? Are deviations in initial cell motion from the mean wind related to environmental characteristics?

- How large is the difference between initial cell motion and right-moving supercell motion? How does this difference relate to the difference between the 0–6 km pressure-weighted mean wind and Bunkers estimated storm motion?

- Are the answers to the above questions different for supercells destined to be tornadic or nontornadic?

The first three questions are addressed using two ensembles of high-resolution, idealized supercell simulations. Findings from this study are presented in the next chapter, which has been submitted to *Monthly Weather Review* and is currently in revision. The remaining five questions are addressed using an observational dataset consisting of over 900 soundings launched in the vicinity of 220 supercells. Environmental conditions and forecast parameters obtained from the soundings are related to storm characteristics, especially those of the right turn. These results are presented in Chapter 3 and will be submitted to *Monthly Weather Review*. Finally, concluding remarks and thoughts on future work are provided in the last chapter.

Chapter 2

Modes of storm-scale variability and tornado potential in VORTEX2 near- and far-field tornadic environments

2.1 Introduction and Background

Storm-scale characteristics and processes necessary for tornadogenesis in supercells include a) a low-level[1], rotating updraft, b) near-surface[2] rotation, and c) significant intensification of that near-surface rotation to tornadic intensity at the surface (Davies-Jones 2015). Our current understanding of each of these characteristics differs. The formation of the rotating updraft, or mesocyclone (Barnes 1978; Doswell and Burgess 1993; Glickman and Walter 2000), is well understood, at least at mid-levels[3]. Horizontal vorticity in the near-storm environment is tilted into the vertical and stretched by a convective updraft (Rotunno 1981; Lilly 1982; Davies-Jones 1984; Dahl 2017). The spatial correlation between vertical velocity and vorticity increases as the angle between the environmental horizontal vorticity vector and wind vectors decreases (i.e., as the streamwise horizontal vorticity component increases; Davies-Jones 1984). This environmental vorticity is enhanced by baroclinic vorticity generation along parcel trajectories entering the updraft (Klemp and Rotunno 1983; Rotunno and Klemp 1985; Markowski et al. 2012b; Dahl et al. 2014). Forecasters use storm-relative helicity (SRH), a measure of the amount of streamwise vorticity at a given location in a certain layer of the atmosphere, to help diagnose environments that are more kinematically conducive for the development of rotation in convective updrafts (e.g., Thompson et al. 2003; Thompson et al. 2007). These same processes are also

[1] In this paper, "low-level" roughly refers to the 0–1 km AGL layer or to the 1 km AGL level.

[2] In this paper, "near-surface" roughly refers to the lowest tens of meters AGL.

[3] In this paper, "mid-level" roughly refers to the 3–6 km AGL layer.

thought to be responsible for the formation of the low-level mesocyclone in a few observational (Markowski et al. 2012a) and modeling studies (Markowski and Richardson 2014; Coffer and Parker 2015; Coffer and Parker 2017; Coffer and Parker 2018; Coffer et al. 2017).

Mechanisms influencing the formation of near-surface rotation have been the focus of many modeling and observational studies. A few processes may contribute, including baroclinic vorticity generation and tilting in storm-scale downdrafts (e.g., Davies-Jones and Brooks 1993; Wicker and Wilhelmson 1995; Markowski and Richardson 2009; Dahl et al. 2014; Markowski and Richardson 2014; Parker and Dahl 2015) and the generation and modification of vorticity via surface friction (Schenkman et al. 2014; Roberts et al. 2016). Regardless of the processes at work, unless preexisting near-surface vertical vorticity is present, a downdraft is theorized to be required for the development of near-surface vertical vorticity (Davies-Jones 1982b; Davies-Jones 1982a). Supporting this work, numerous observations exist of rear-flank downdrafts (RFDs; Markowski et al. 2002) and downdrafts associated with descending reflectivity cores (Rasmussen et al. 2006; Markowski et al. 2012a; Markowski et al. 2012b; Markowski et al. 2018) in the vicinity of tornadoes. However, Rotunno et al. (2017) showed that "rapid near-surface amplification of vertical vorticity" can occur solely due to tilting of initially horizontal vorticity and subsequent stretching. Furthermore, some observational and modeling studies have shown similarities between near-surface kinematic fields in tornadic and nontornadic supercells (e.g., Trapp et al. 1999; Wakimoto and Cai 2000; Markowski 2008; Markowski et al. 2011, Coffer et al. 2017). Given that "the only fundamental requirement for downdrafts to produce surface vertical vorticity is the existence of downdraft-relative flow" (Parker and Dahl 2015), near-surface vertical vorticity probably exists in the vast majority of, if not all, supercells. Thus, it is likely that a deciding factor in tornadogenesis is not whether or not near-surface vertical vorticity exists, but how that vorticity is modified by the supercell.

In the final moments of tornadogenesis, an intense, low-level updraft stretches near-surface vertical vorticity and wind speeds increase to tornadic intensity. The resulting magnitude of vertical vorticity stretching is related to the strength of the low-level updraft, because vertical velocities vanish to zero at the surface. The buoyancy of near-surface air within which the stretched vorticity resides also plays a role in modulating vertical vorticity tendency (e.g., Markowski and Richardson 2014); generally, more buoyant air experiences larger upward displacements due to vertical pressure perturbation gradient forces associated with the low-level updraft, and the opposite is true for less buoyant air. As discussed previously, low-level updraft strength and associated dynamic lift is linked to the magnitude and orientation of the low-level, environmental vertical wind shear. Storm outflow buoyancy is at least partially related to low-level, environmental moisture content (Rasmussen and Blanchard 1998; Rasmussen 2003; Thompson et al. 2003; Craven et al. 2004), with lower lifted condensation levels (LCLs) favoring less negatively buoyant outflow. The physical reasoning for this relationship involves less evaporational cooling in more humid environments (Kumjian 2011; French et al. 2015). This in turn is more favorable for tornadogenesis than supercells with more negatively buoyant outflow (Markowski et al. 2002). In nontornadic supercells, it appears that the low-level updraft fails to draw air upwards far from the surface (e.g., Markowski and Richardson 2014; Coffer and Parker 2017), suggesting the presence of a weaker low-level updraft and/or more negatively buoyant outflow. Recent studies have also found that increased spatial overlap between the surface circulation maximum and low- and mid-level mesocyclones, modulated by low-level wind shear (Guarriello et al. 2018) and humidity (Brown and Nowotarski 2019) in the environment, increases tornado potential.

Some severe weather outbreaks conducive for supercells are characterized by nearly every supercell producing a tornado, while others may include both tornadic and nontornadic supercells in close proximity to each other (e.g., Klees et al. 2016; Markowski and Richardson 2017). The reason for the latter may be due to mesoscale differences in the

background environment (e.g., Markowski et al. 1998; Klees et al. 2016), stochasticity in storm-scale features and evolution (e.g., Coffer et al. 2017), or a combination of both. Specifically, Coffer et al. (2017) examined the "volatility of tornadogenesis" in composite tornadic and nontornadic supercell environments (Parker 2014) sampled during VORTEX2 (Wurman et al. 2012). The study used high resolution CM1 (Cloud-Model 1; Bryan and Fritsch 2002) experiments to create two 15-member ensembles that simulated supercells in both of these environments. All 15 of the supercells initialized in the tornadic near-field environment produced a tornado (defined in Coffer et al. 2017), and six produced a tornado in the nontornadic near-field environment. Thus, at least in simulations, the tornadic environments sampled during VORTEX2 appear to be strongly favorable for tornadogenesis regardless of storm-scale stochasticity, while the sampled nontornadic environments appear to be conditionally favorable for tornadogenesis given fortunate (or unfortunate) variations in storm-scale features. The difference in tornado production between the simulated storms was mostly attributed to variations in rotation-induced dynamic lift, with storms initialized in the tornadic environment containing stronger low-level updrafts than those in the nontornadic environment. This difference was related to variations in the environmental low-level wind profile in both environments; while both contained similar effective SRH, the tornadic environment was characterized by more streamwise horizontal vorticity (and SRH) in the lowest 500 m AGL than the nontornadic environment (e.g., Thompson and Edwards 2000; Esterheld and Giuliano 2008; Coffer et al. 2019). Tilting and subsequent stretching of this vorticity resulted in the development of a longer-lived, more intense low-level updraft in the tornadic environment.

In this study, I explore the volatility of tornadogenesis further by analyzing an ensemble of simulations in the near- and far-field composite tornadic environments from VORTEX2 (Coffer et al. 2017 only examine the near-field environment in their simulations). As described in Parker (2014), the tornadic near-field environment was extracted roughly 40 km

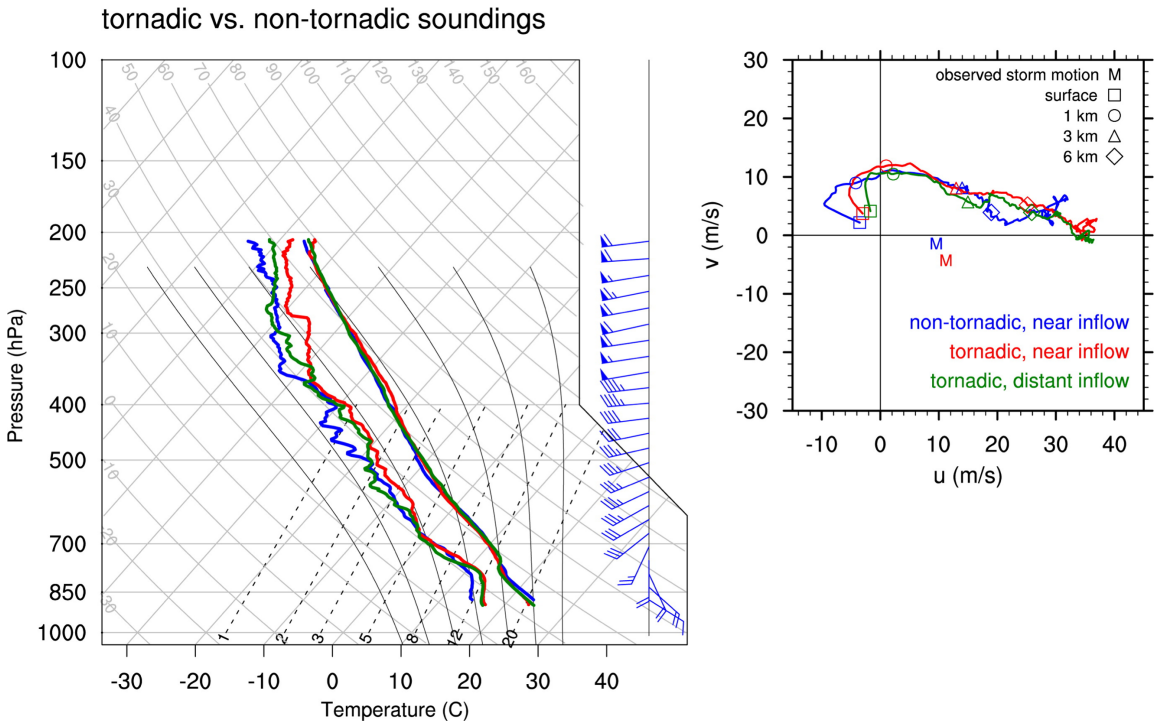

Figure 2.1: Soundings extracted from composite environments sampled during VORTEX2 in the vicinity of tornadic and nontornadic supercell thunderstorms. The mean storm motion of all tornadic storms is indicated by the red "M", and the mean storm motion of all nontornadic storms is indicated by the blue "M". Near-inflow (far-inflow) soundings were extracted roughly 40 km (80 km) away from the storm updraft. Tornadic (nontornadic) soundings were extracted from the composite environment sampled in the vicinity of tornadic (nontornadic) supercells. The tornadic and nontornadic near-inflow soundings were used in Coffer et al. (2017), and the tornadic near- and far-inflow soundings are used in this study. From Parker (2014).

upstream of the supercell updraft in the inflow region (the same as in Coffer et al. 2017) whereas the far-field environment was extracted roughly 80 km upstream (see Fig. 2.1). Comparing these two environments allows us to address a couple of questions in addition to those presented in Coffer and Parker (2017), Coffer et al. (2017), and Coffer and Parker (2018). In particular, I am interested in how the spatial evolution from the far-field to

the near-field environments impacts the volatility of tornadogenesis and, since low-level horizontal vorticity characteristics are similar in both cases (Fig. 2.3), assessing kinematic characteristics influencing any differences in the volatility of tornadogenesis. With this in mind, this study aims to address the following questions:

1. What patterns of variability in storm characteristics and tornado potential exist between storms forming in essentially the same environment?

2. Is the volatility of tornadogenesis different in the near- and far-field VORTEX2 environments?

3. If so, what drives differences in the volatility of tornadogenesis in these environments?

2.2 Data and Methods

2.2.1 Model setup

The simulations used in this study were created using the Bryan cloud model (CM1; Bryan and Fritsch 2002), release 19.5. CM1 is an idealized, three-dimensional, non-hydrostatic model useful for studying small-scale atmospheric phenomena such as supercell thunderstorms and tornadoes. Simulated storms were initiated in horizontally homogeneous environments using the updraft nudging technique outlined in Naylor and Gilmore (2012). Rather than a warm bubble, this technique applied a volume of updraft characterized by a maximum vertical velocity of 15 m s^{-1} at 1.5 km AGL at the beginning of the simulation. This nudging diminished with horizontal and vertical extent and was applied consistently for 15 minutes before exponentially decreasing toward 0 m s^{-1} 20 minutes into the simulation. Each simulation was run for 2 hours.

A stretched 200 x 200 km horizontal grid was used with a minimum grid spacing of 125 m in the inner 100 x 100 km domain stretched to 3875 m on the edges. Grid motion was set to the approximate storm motion in order to keep each simulated storm near the center of

the grid. 115 vertical levels were present, with vertical grid spacing stretching from 20 m in the lowest 300 m AGL to 280 m at the model top (18160 m). The lowest model level was 10 m AGL. I used a 0.6 s timestep along with a 5^{th} order advection scheme. The National Severe Storms Laboratory 2-moment microphysics scheme was used (Ziegler 1985; Mansell 2010; Mansell et al. 2010) and a semi-slip condition was applied to the bottom boundary with a constant drag coefficient (C_d) of 0.0014. This value is consistent with a few recent simulation studies (Coffer and Parker 2017; Coffer et al. 2017; Coffer and Parker 2018) and was derived from the rear-flank outflow composite sounding shown in Parker (2014). Acknowledging the concerns of Markowski and Bryan (2016) in that simulated surface drag may excessively modify near-ground vertical wind shear, I applied this small constant drag coefficient to my simulations in the hope of increasing physical realism and to more directly compare my results with recent modeling studies. In an effort to best preserve the base-state environment, the Coriolis force was applied to the perturbation winds (Roberts et al. 2016).

2.2.2 Ensemble configuration

The composite, tornadic near-field (far-field) thermodynamic profile found in Parker (2014) was used as the base-state thermodynamic profile for each member of the near-field (far-field) ensemble (shown by the red and green lines in Fig. 2.1). The base-state wind profile for each member in the near-field (far-field) tornadic ensemble was generated by perturbing the composite near-field (far-field) tornadic wind profile observed in VORTEX2 ((Parker 2014)). The original composite wind profiles are bolded in Fig. 2.3. Commonly used parameters for each environment are shown in Fig. 2.2[4]; unsurprisingly, both exhibit characteristics typical of environments in the vicinity of tornadic supercells, although the

[4]The near-field environmental parameters presented here are slightly different than those in Coffer and Parker (2017). the parameters shown here were calculated using MetPy (May et al. 2017) whereas those shown in Coffer and Parker (2017) were calculated using SHARPpy (Blumberg et al. 2017).

	SB CAPE	SB CIN	SB LCL	0–1 km SRH	0–3 km SRH	ESRH	Critical Angle	SCP	STP
Near-field	2156	-86	733	186	296	257	92	9.0	2.7
Far-field	2224	-84	733	126	243	191	99	5.9	1.9

Figure 2.2: Commonly used parameters associated with the tornadic near- and far-field composite VORTEX2 environments. Convective available potential energy (CAPE; $J\ kg^{-1}$), convective inhibition (CIN; $J\ kg^{-1}$), and lifted condensation level (LCL; m) are all calculated using the surface-based (SB) parcel. 0–1 and 0–3 km SRH ($m^2\ s^{-2}$) are shown as well as SRH calculated within the effective layer (CAPE ¿ 100 $J\ kg^{-1}$ and CIN ¿ -250 $J\ kg^{-1}$) of the storm (ESRH; $m^2\ s^{-2}$). Critical angle is calculated as the angle (in degrees) between the 10 m AGL storm-relative wind vector and the 10–500 m AGL shear vector (as defined in Esterheld and Giuliano (2008)). The significant tornado parameter (STP; dimensionless) and supercell composite parameter (SCP; dimensionless) are also calculated as defined in Thompson et al. (2003).

significant tornado parameter and supercell composite parameter in the near-field environment are larger. This is due to the larger low-level shear in the near-field environment, resulting in greater SRH.

Perturbations applied to the wind profile were randomly drawn from a normal distribution of velocities ranging from -2 m s^{-1} to 2 m s^{-1} and applied to each vertical level (115 total) of the wind profile. The velocity range of 2 m s^{-1} was chosen to best represent radiosonde observational error and sampling inconsistencies (e.g., Dawson II et al. 2012) and the average of all perturbations applied to any profile was essentially zero. This resulted in two ensembles (near-field and far-field) consisting of 15 members each. Each ensemble consisted of one control member with a base-state wind profile characterized by the non-perturbed sounding from Parker (2014) and 14 members with slightly perturbed base-state wind profiles as described above (Fig. 2.3). The only difference between each member in the near- or far-field ensemble is the background wind profile. The thermodynamic profiles used to represent each member in each ensemble were identical, and the thermodynamic

profiles differed only slightly between the near- and far-field composite environments (see Fig. 2.1). Differences within these two ensembles (i.e., intra-ensemble differences) yield insight into the sensitivity of tornadogenesis to different storm-scale characteristics (which are present in this case due to very small differences in the background environment).

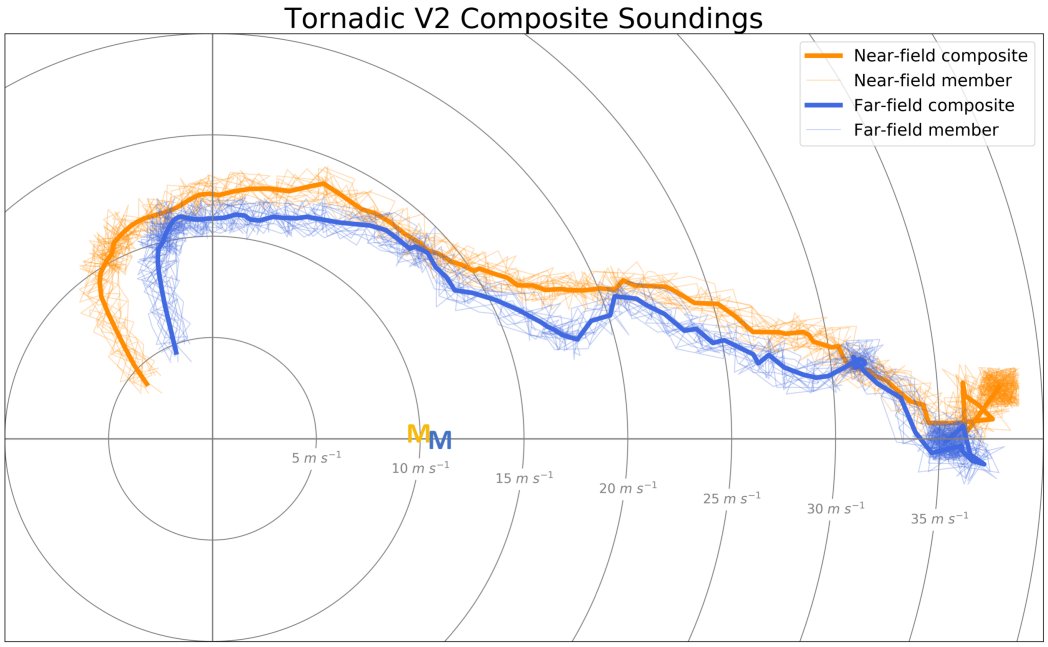

Figure 2.3: The tornadic near-inflow (thick orange line) and far-inflow (thick blue line) control hodographs (also shown in 2.1) used in this study. Thin lines indicate the 14 hodographs, derived from each control hodograph, used as the base-state, homogeneous wind profile in each ensemble member. The mean storm motion of all supercells in the near-field ensemble is indicated by the orange "M", and the mean storm motion of all supercells in the far-field ensemble is indicated by the blue "M".

2.2.3 Definition of tornado genesis and failure

Because my simulation setup is almost identical to that of Coffer and Parker (2017), Coffer et al. (2017), and Coffer and Parker (2018), I use the same criteria to define the occurrence of tornado genesis and failure. A tornado is defined when grid points with:

1. 10 m AGL vertical vorticity ≥ 0.3 s^{-1}

2. 0–1 km AGL pressure perturbations $\leq$ -10 hPa, and

3. 10 m AGL wind speeds ≥ 35 m s^{-1} (low-end EF0)

occur within 4 km of each other for at least two consecutive minutes (using output every minute). The time of tornadogenesis is defined as the first time these criteria are met. If these criteria are not met during the two-hour simulation, the time of tornado failure is defined as the time of maximum 10 m AGL vertical vorticity.

2.2.4 EOF analysis

To analyze spatial patterns of variance in the simulated supercells, empirical orthogonal function (EOF; Lorenz 1956) analysis was performed on different output variables. This type of composite analysis has previously been performed in meteorological studies (e.g., Richman 1980) and used in severe weather studies primarily to analyze synoptic-scale patterns supportive of tornadoes (e.g., Schaefer and Doswell 1984; Mercer et al. 2012). Using this technique, large datasets are reduced to a smaller set of normal characteristic patterns, or EOFs. In this study, singular value decomposition (e.g., Bretherton et al. 1992) was used to compute the principal component (PC) timeseries. Spatial patterns of the fields were then obtained by regressing the original spatial field of each variable within 10 km of the near-surface vortex with the corresponding standardized leading PC timeseries. The leading EOF pattern (EOF1) explains the largest fraction of variance in the original dataset and subsequent EOF patterns explain decreasing fractions of variance. While the orthogonal nature of the EOFs limits their applicability to the real atmosphere, I examine EOF1s that explain the most variance and are aligned with known, physical features.

This study examines EOF patterns of simulated variables in the near- and far-field ensemble at the time of tornadogenesis or tornadogenesis failure, including near-surface vertical vorticity (ζ), density potential temperature perturbation (θ'_ρ), and wind direction.

This approach differs from most meteorological applications of EOF analysis in that the grid spacing is smaller (125 m) and the number of input datasets is smaller (15 for each EOF pattern for each ensemble). As will be discussed in the next section, some EOFs in this study contain significant small-scale structure due to the small grid spacing used and turbulence present in the simulated storm outflow. However, insight can be drawn from examining regions of the domain characterized by greater or lesser amplitudes of small-scale variability and where demarcations between these two regions are present. Due to the small number of input datasets and the fact that time or spatial means were not subtracted from the dataset, EOF1s that explain a large amount of variance will appear similar to a composite map constructed by simple ensemble-averaging. Regardless, the EOF analysis will yield leading patterns of variance for each field in addition to providing analytical support for spatial patterns that emerge in each 15-member ensemble.

2.3 Results

2.3.1 Bulk ensemble characteristics

Every member of both the near- and far-field ensembles develops a right-moving supercell with similar aggregate characteristics during the two-hour simulation. This supercell develops around 40–50 minutes into each simulation. By the time of tornado genesis or failure, classic observed and simulated supercellular characteristics are evident in each member, including a reflectivity hook and strong mid-level updraft (Figs. 2.4 and 2.5). These supercells remain discrete for the remainder of the two-hour simulation.

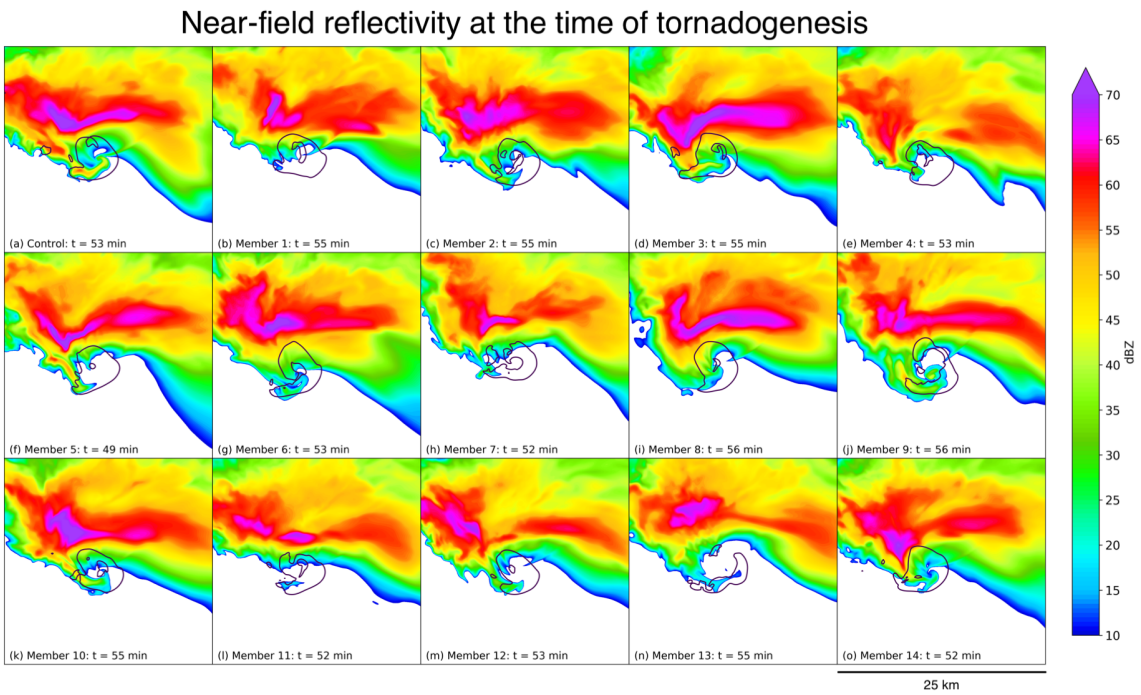

Figure 2.4: Simulated radar reflectivity (10 m AGL, shaded) and updraft (20 m s^{-1} at 3 km AGL, black contour) in the 15 near-field ensemble members. Variables are plotted at the time of tornadogenesis or tornadogenesis failure. These times are indicated in the bottom-left corner of each panel.

The two ensembles differ in terms of tornado production. Based on the criteria (described in Section 2.2.3), all near-field ensemble members produce a tornado and five far-field ensemble members produce a tornado. Fig. 2.4 shows surface[5] reflectivity and the location of the mid-level updraft for each ensemble at the time of tornadogenesis in each near-field ensemble member (ranging from 49–56 minutes). Although all members are initialized in essentially the same environment (Fig. 2.3), each storm is slightly different (as expected, given the nature of error growth on convective scales; Cintineo and Stensrud 2013). In general, all storms contain a strong mid-level updraft bounded by a hook echo to the west (more evident in some members than others) and large reflectivity to the north.

[5]In this paper, "surface" refers either to the surface or the lowest model level (10 m AGL).

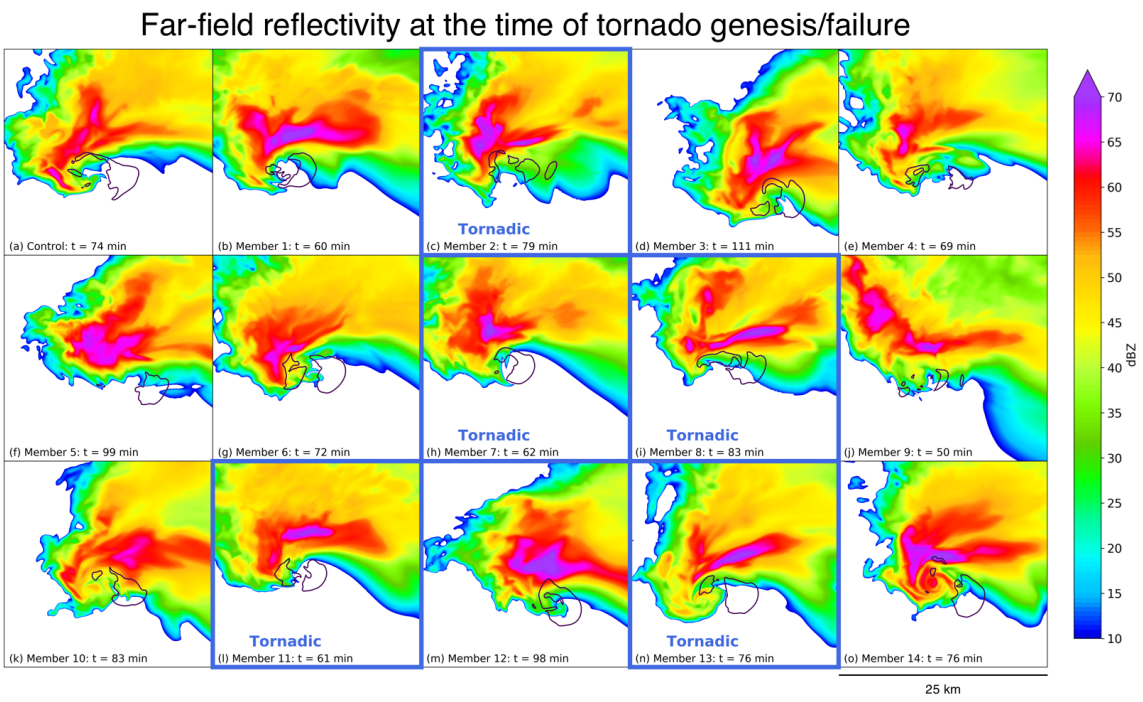

Figure 2.5: As in Fig. 2.4 except for the 15-member far-field ensemble. The five tornadic members are outlined in blue.

Reflectivity hook echoes and mid-level updrafts are also present in the far-field ensemble at the time of tornado genesis or failure, although they are not as pronounced in all of the individual members (Fig. 2.5). Compared to the near-field ensemble, some mid-level updrafts are weaker and smaller (e.g., Fig. 2.5e, j), but overall the reflectivity and mid-level updraft presentation does not differentiate well between the tornadic and nontornadic members within the far-field ensemble. In particular, some mid-level updrafts in nontornadic members (e.g., Fig. 2.5o) appear just as strong and expansive as those in tornadic members (e.g., Fig. 2.5n).

Surface outflow characteristics also differ between the two ensembles at the time of tornado genesis or failure (Figs. 2.6 and 2.7). Both ensembles contain very cold ($\theta'_\rho \leq$ -5 K) surface air by this time in the rear-flank downdraft—consistent with the observational analyses of Markowski et al. (2002)—and cool air (θ'_ρ around -1 to -3 K) in the forward-flank region to the east. However, the coldest outflow is generally constrained farther away

from the surface vortex in the near-field ensemble (Fig. 2.6) than in the far-field ensemble (Fig. 2.7). Localized, zonally oriented cooling due to forward-flank precipitation is also more evident in the near-field ensemble than in the far-field ensemble (e.g., Fig. 2.6i). Some of this is due to the smaller range of tornadogenesis (or failure) times in the near-field ensemble than those in the far-field ensemble (these times are indicated at the bottom left of the figure panels). However, some far-field members that produce strong surface vortices earlier in their lifecycle do not exhibit localized forward-flank cooling like the near-field members (e.g., Fig. 2.7e, h, j, l).

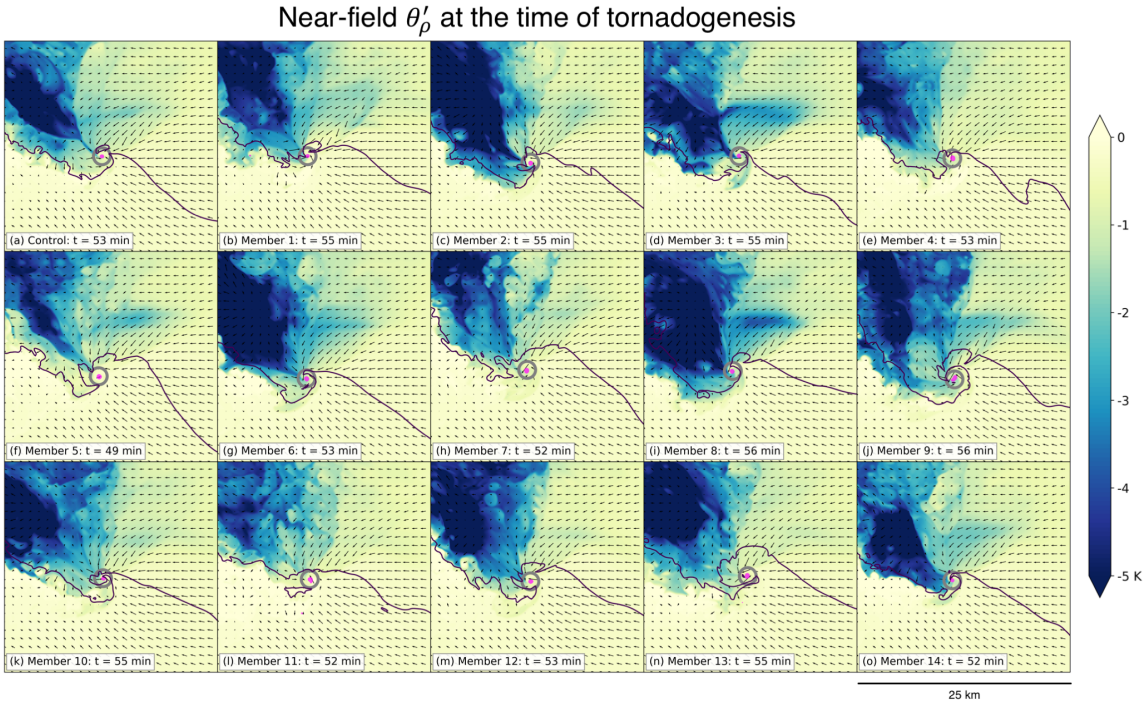

Figure 2.6: Simulated surface θ'_ρ (shaded), 10 dBZ reflectivity (solid black line), and storm-relative wind direction (arrows) in the 15 near-field ensemble members. As in Fig. 2.4, variables are plotted at the time of tornadogenesis or tornadogenesis failure for each member. Surface vertical vorticity exceeding 0.1 s^{-1} is shaded in pink, and the surface vertical vorticity maximum is circled for clarity.

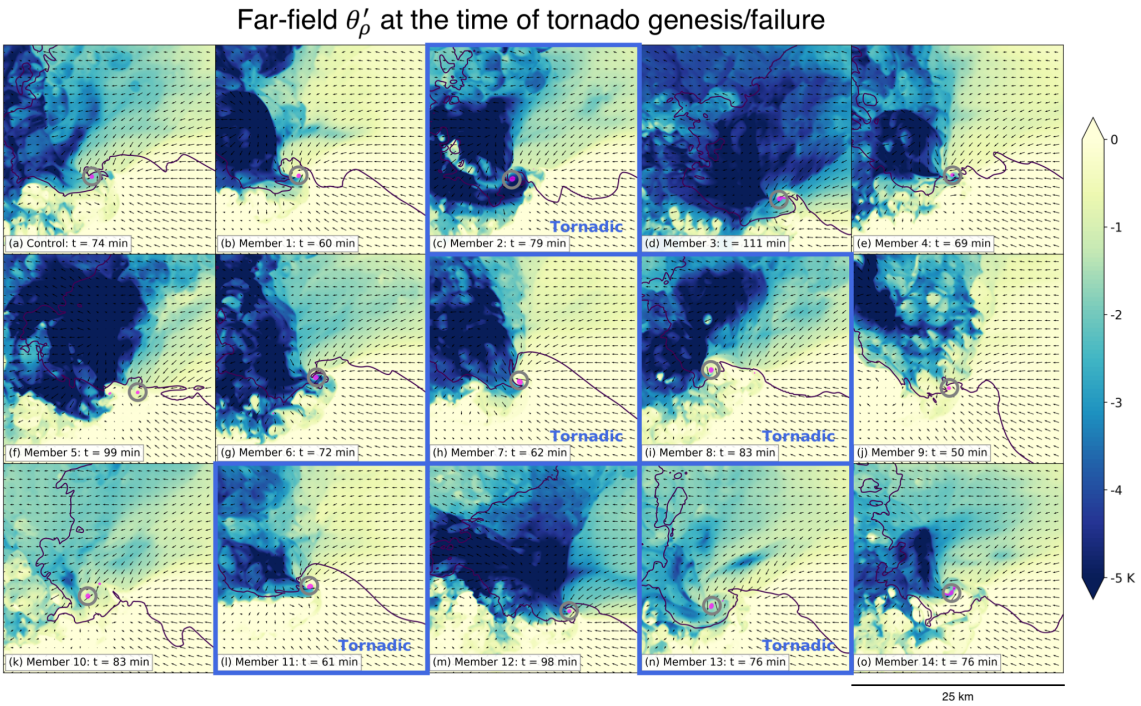

Figure 2.7: As in Fig. 2.6 except for the 15-member far-field ensemble. The five tornadic members are outlined in blue.

Timeseries of 1 km AGL updraft flux, minimum surface θ'_ρ, and maximum surface ζ within a 50 km^2 domain centered on the mid-level updraft of the supercell in each ensemble member are presented in Fig. 2.8. Median ζ in the near-field ensemble is slightly larger than that in the far-field ensemble until around t = 50 minutes (Fig. 2.8a). At this point, maximum surface vertical vorticity magnitudes increase dramatically in the near-field ensemble to over twice those in the near-field ensemble around t = 55 minutes. Thereafter, near-field magnitudes generally decrease until around t = 100 minutes. Meanwhile, maximum surface vertical vorticity magnitudes in the far-field ensemble are not nearly as peaked and gradually increase until around t = 75 minutes. After this point, the two distributions remain similar until around t = 105 minutes when the near-field median grows slightly larger than the far-field median through the rest of the simulation period.

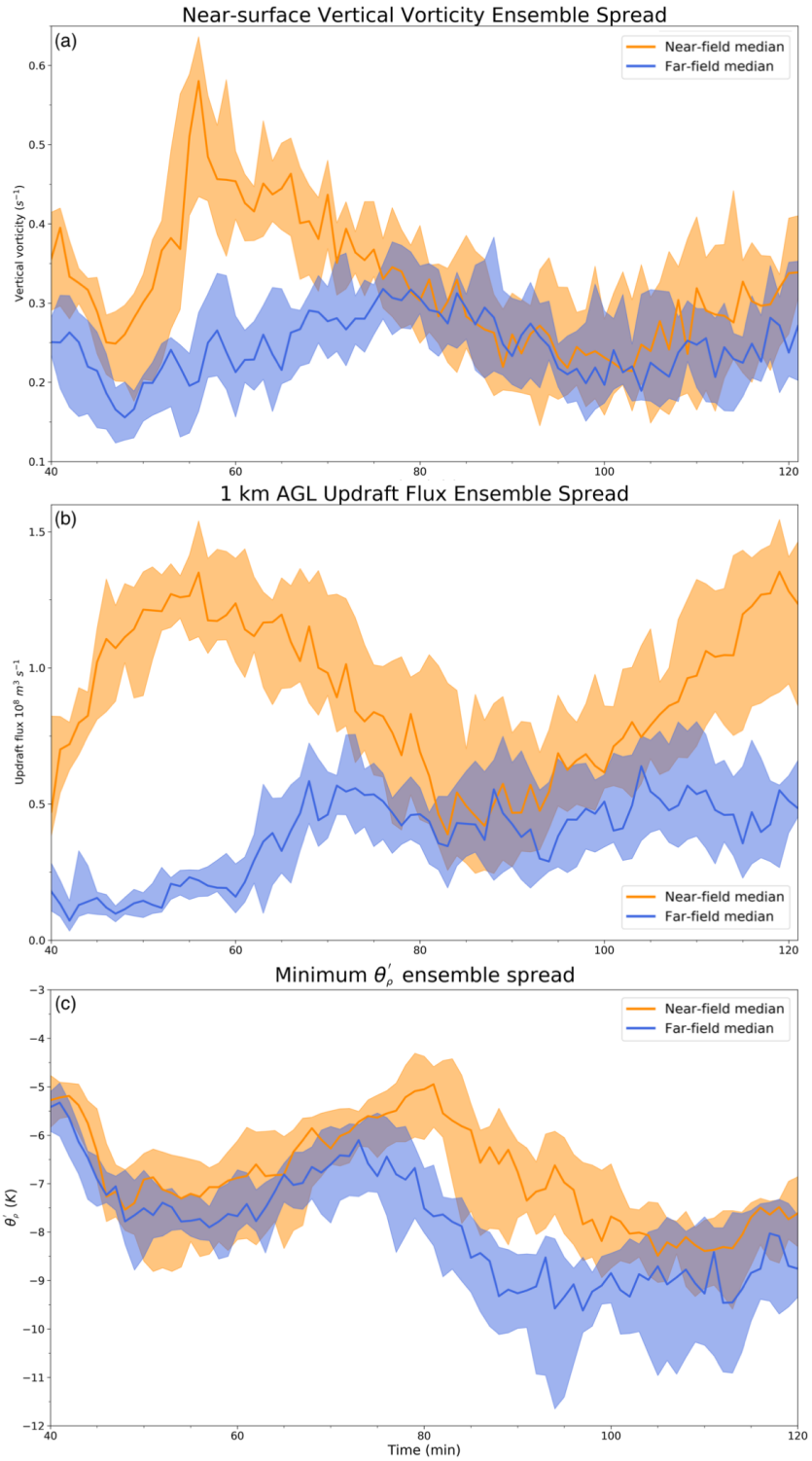

Figure 2.8: (Continued on the following page.)

Figure 2.8: Timeseries of (a) maximum surface vertical vorticity, (b) 1 km AGL updraft flux where vertical velocity exceeds 10 m s^{-1}, and (c) minimum surface θ'_ρ within a 50 km^2 domain centered on the mid-level updraft of the right-moving supercell in each ensemble member from 40–120 minutes into the simulation. The first 40 minutes are excluded due to unphysical model output associated with initialization. The solid blue (orange) line in each panel indicates the median of the specified variable for the far-field (near-field) ensemble. The blue (orange) shading indicates the range of the 10th–90th percentiles of the specified variable for the far-field (near-field) ensemble. Gray shading indicates the 56–100-minute time period in which all members of both ensembles either experience tornado genesis or failure.

1 km AGL updraft fluxes are stronger in the near-field ensemble than in the far-field ensemble (Fig. 2.8b). This difference is present from the beginning of the time period and peaks around t = 55–60 minutes (during tornado production in all near-field members). At this point, updraft fluxes in the near-field ensemble are 6–7 times stronger than those in the far-field ensemble. Afterwards, 1 km AGL updraft fluxes in the near-field ensemble gradually decrease until around t = 85–90 minutes, at which point they increase again until the end of the simulations. Both increases in near-field updraft fluxes (t = 40–50 minutes and 85–120 minutes) begin several minutes before an increase in maximum surface vertical vorticity magnitudes (t = 50–55 minutes and 100–120 minutes). Meanwhile, far-field updraft fluxes gradually increase until around t = 70 minutes and remain constant thereafter.

Minimum surface θ'_ρ is similar between the ensembles through around t = 70 minutes (Fig. 2.8c). Based on the timeseries, cold downdrafts reach the surface in both ensembles at the same time, around t = 40–45 minutes. During the next few minutes, θ'_ρ in both ensembles decreases by 2–4 K and gradually warms until around t = 75 minutes. At this time, median values of the minimum θ'_ρ in the near-field ensemble are around 0.5–1 K

warmer than those in the far-field ensemble. After t = 75–80 minutes, a second round of cold downdrafts reaches the surface that results in decreasing θ'_ρ in both ensembles until t = 90–100 minutes. The minimum surface θ'_ρ is substantially lower in the far-field ensemble during this period.

These bulk ensemble characteristics reveal a few key relationships between the ensembles (Fig. 2.8). First, the interquartile range is generally similar in both ensembles. This suggests that the influence of intra-storm processes (i.e., those not strongly governed by the background environment) on supercell characteristics is similar in both composite VORTEX2 environments. Next, at least in the near-field ensemble, increases in low-level updraft flux occur simultaneously with decreases in surface θ'_ρ (t = 45–50 minutes and 80–100 minutes), which precede increases in surface vertical vorticity. Finally, some of the signals in the ensembles are similar but lagged in time. In particular, the near-field ensemble rapidly peaks in surface vertical vorticity magnitudes and low-level updraft fluxes around t = 55 minutes, and those in the far-field ensemble gradually increase and peak around t = 70–75 minutes. Perhaps this is evidence of larger streamwise vorticity in the background environment (Fig. 2) supporting more rapid low-level mesocyclone development and, in this case, a peak in tornado potential earlier in the storms' lifecycles. On the other hand, the second round of cold downdrafts reach the surface 5–10 minutes earlier in the far-field ensemble (t = 70–75 minutes) than in the near-field ensemble (t = 80 minutes). Ultimately, although the observed hodographs were both associated with tornadic storms in VORTEX2, the character of the simulated ensembles is different enough that one ensemble is significantly more supportive of simulated tornadoes.

2.3.2 Storm-scale characteristics influencing tornado genesis and failure

To assess what local factors influence tornado genesis or failure in the ensemble members, mean surface θ'_ρ and maximum 1 km AGL vertical velocities within 4 km of the surface vortex are analyzed. Fig. 8 shows violin plots of these variables during the ten-minute

period leading up to tornado genesis or failure (i.e., the times indicated in Figs. 2.4 and 2.5). Unsurprisingly, 1 km updrafts near the developing vortex are stronger in the near-field ensemble during most of the ten-minute period (Fig. 2.9a). The difference between the medians of these distributions is statistically significant at the 90% confidence level at t-2 and at t=0 using a Monte Carlo test with 10,000 iterations. This difference maximizes at the time of tornado genesis or failure. Low-level updrafts strengthen in both ensembles from t-10 to t-2, but in the final minutes preceding tornado genesis or failure, updrafts in the near-field ensemble continue to strengthen while those in the nontornadic far-field members weaken. The five tornadic far-field members exhibit varying low-level updraft strengths, with some above the distribution of nontornadic far-field members (e.g., Members 2 and 7) and one below (Member 8).

Interestingly, all surface vortices in the ten nontornadic far-field members achieved surface vertical vorticity greater than 0.3 s^{-1}. Of these ten, seven members achieved all tornadogenesis criteria except that the vortex was not sustained at that strength for at least two minutes (Members 5, 6, and 9 did not). This vortex evolution shows that the failure of the far-field ensemble to produce tornadoes was not due to an inability to produce strong vortices, but rather due to an inability to sustain strong vortices.

First, outflow near the developing vortex in the near-field ensemble members is warmer than that in the far-field ensemble. The difference between the means of both distributions is statistically significant at the 99% confidence level during this time period using a Monte Carlo test with 10,000 iterations. This result is consistent with the understanding that warmer outflow in the vicinity of the vortex (i.e., within 4 km) is associated with increased tornado potential (Markowski et al. 2002). The range of the θ_ρ' distribution is also much smaller in the near-field ensemble, especially in the minutes preceding tornadogenesis. These findings combined with the interpretation of Fig. 7c show that, although

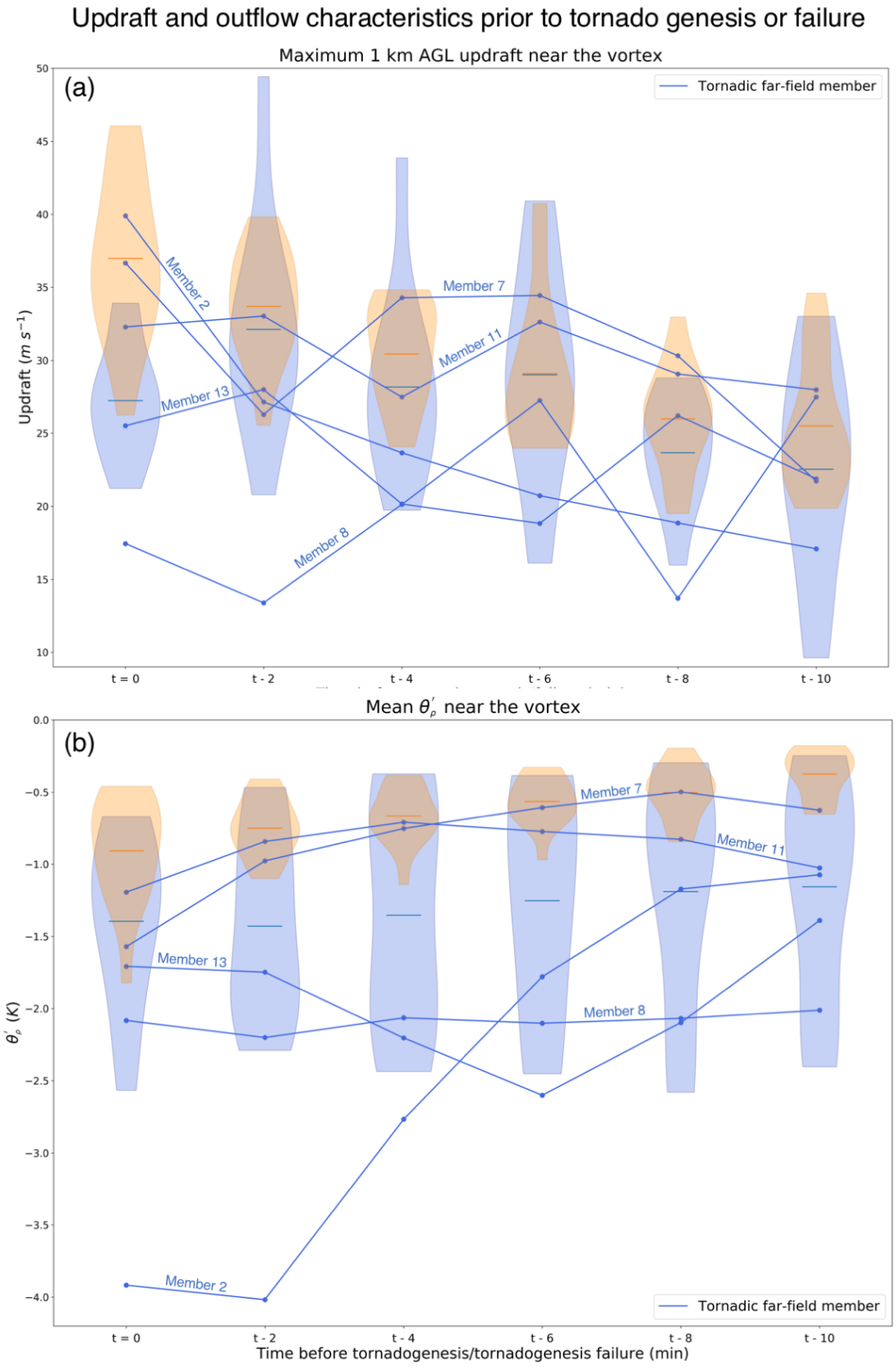

Figure 2.9: (Continued on the following page.)

Figure 2.9: a) Violin and scatter plots of 1 km AGL vertical velocity within 4 km of the surface vortex in the near-field (orange) and far-field (blue) ensembles during the ten-minute period prior to tornado genesis or failure. "t = 0" represents the time of tornado genesis or failure. The near-field violin plots (orange) are comprised of maximum vertical velocities from the tornadic members (n = 15). The far-field violin plots (blue) are comprised of maximum vertical velocities from the nontornadic members (n = 10) and the five tornadic members are represented with blue lines. b) As in (a) except for mean surface AGL θ'_ρ.

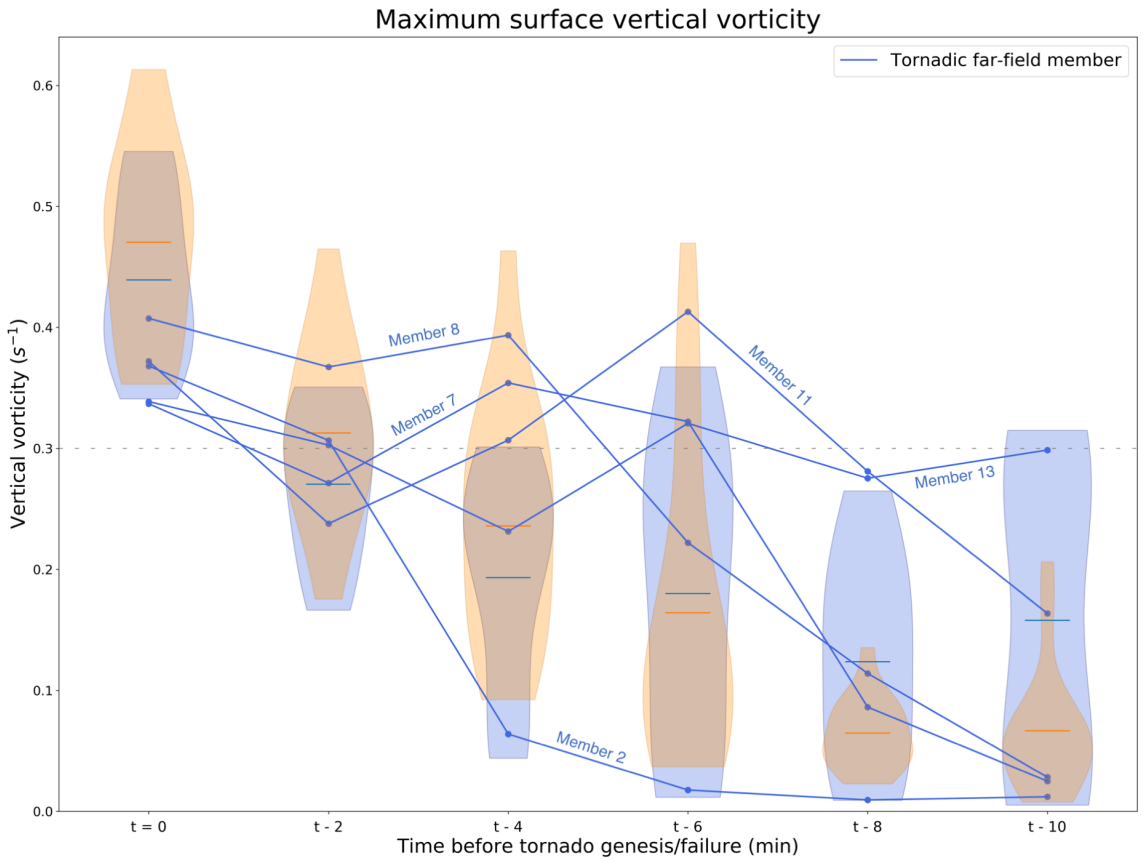

Figure 2.10: As in Fig. 2.9 except for surface ζ. ζ = 0.25 s^{-1} is highlighted because exceeding that value is one of the three criteria for tornado genesis in the simulation. It is a necessary but not sufficient condition.

the range of outflow temperatures within the entire storm is similar between the two ensembles (e.g., the interquartile range in Fig. 7c), storms in the near-field ensemble more successfully restrain colder air away from the developing vortex, resulting in warmer outflow there than in the far-field ensemble. θ_ρ' in the tornadic far-field members does not differ from the nontornadic members, except for Member 2. It appears the strength of the low-level updraft (the strongest of the far-field ensemble) was sufficient for tornadogenesis within this negatively buoyant outflow. These results also show that, in addition to the presence of stronger low-level updrafts, the success of the near-field ensemble in sustaining intense vortices at t=0 was influenced by warmer outflow in the vicinity of the vortices.

2.3.3 Storm-scale variability within both ensembles

To further quantify differences between the near- and far-field ensembles and to examine spatial features and processes influencing tornado genesis or demise, EOF1 analyses of surface characteristics are presented next. Fig. 2.11 shows the regression of surface ζ in the near- and far-field ensembles at the time of tornado genesis or failure. Larger magnitudes of the EOF1 (either positive or negative) indicate regions with greater variance within each ensemble, while smaller magnitudes indicate regions with less variance. Regions of large variance with opposing magnitudes indicates that the variance in these regions is anticorrelated. The leading modes explain over 62% and 53% of the variance in the near- and far-field ensembles, respectively. The second and third EOFs are qualitatively similar to the leading EOF except that they explain roughly one order of magnitude less variance (not shown). Substantial small-scale structure is present in the supercell outflow west of the vortex because ζ is a spatial derivative field and thus is influenced by turbulent flow in these areas. Across the 15-member ensemble, increased (decreased) turbulence will coincide with increased (decreased) variance. Meanwhile, near-zero magnitudes are present in the environment east of the vortex. Large gradients between these regions in both ensembles are subjectively highlighted, including a demarcation extending from the east side

of the vortex curling around to the southwest. This is consistent with the location of the rear-flank downdraft gust front in each of the ensemble members
(see the storm-relative wind vectors in Figs. 2.6 and 2.7). A cyclonic wind shift is also present along the rear-flank gust front with southeasterly environmental winds shifting to near-zero wind speeds within the rear-flank outflow (Fig. 2.12). [These wind speeds are not actually near-zero in each individual ensemble member (Fig. 2.6); compositing the large spatial variability in wind direction (Fig. 2.12a) simply results in a near-zero velocity vector.]

A second boundary appears in both ensembles extending northward from the vortex into the core of the storm (Fig. 2.11). The gradient in EOF1 magnitudes across it is smaller than that across the rear-flank downdraft, with EOF1 magnitudes increasing to the west. This is consistent with the location of storm-scale boundaries present in some past supercell simulations including left-flank convergence boundaries (Beck and Weiss 2013), vortex sheets (Markowski et al. 2014), vorticity rivers (Dahl et al. 2014; Coffer and Parker 2017), and streamwise vorticity currents (Orf et al. 2017). These boundaries, particularly vorticity rivers and streamwise vorticity currents, have been theorized to increase tornado potential in supercells by either interacting with the low-level updraft or the tornado itself. In this study, this boundary is present in both the tornadic near-field ensemble and largely nontornadic far-field ensemble. It is also present in EOF analyses of vertical vorticity in the ten nontornadic, far-field members (not shown). It is closer to the surface vortex in the near-field ensemble, whereas in the far-field ensemble it appears farther east.

The physical nature of the demarcations revealed in the vertical vorticity EOF1s (Fig. 2.11) is examined in Fig. 2.12 with the characteristic patterns of the leading mode of variability of surface θ_ρ' and storm-relative wind direction. A gradient in θ_ρ' variability is present in both ensembles EOF1 (Fig. 2.12) along the southern edge of the storm, generally consistent with the location of the rear-flank gust front. This signal is collocated with increased variance in storm-relative wind direction, indicative of varying flow behind the

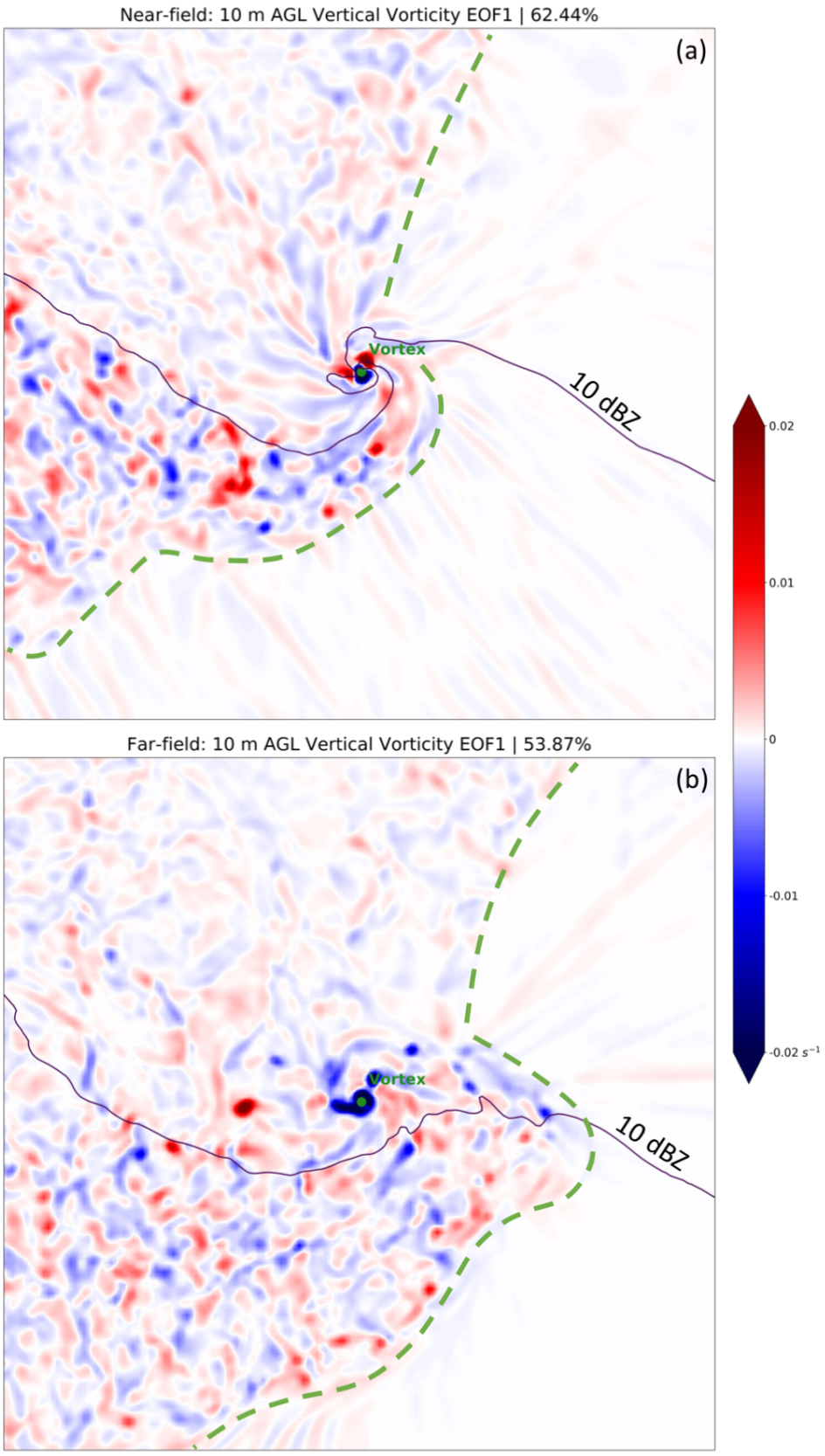

Figure 2.11: (Continued on the following page.)

Figure 2.11: Regression of 10 m AGL ζ onto the leading PC timeseries of (shaded) for the (a) near-field ensemble and (b) far-field ensemble. Ensemble-composited 10 dBZ radar reflectivity at 10 m AGL is contoured in black and the location of the vortex is indicated. PC timeseries for each ensemble were derived from the 15 ensemble members at the times indicated in Fig. 2.4. Green dashed lines subjectively indicate local regions with large gradients in the magnitude of the EOF1.

rear-flank gust front in each storm. As above, these qualitative signals also exist in the second and third EOF modes (not shown).

Gradients in θ'_ρ and wind direction also exist to the north of the vortex in both ensembles. These gradients are clearer in the near-field ensemble (Fig. 2.12a). A gradient in the θ'_ρ EOF1 extends northwestward and then northward from the vortex, along with a gradient in storm-relative wind direction to the east (extending due north from the vortex). Both of these features lie to the west of the gradient in ζ EOF1 (Fig. 2.11a). The region is also characterized by a broad cyclonic wind shift in storm-relative winds (Fig. 2.12a). These features are not as clear in the far-field ensemble (Fig. 2.12b). A cyclonic wind shift is present, but any gradients in the θ'_ρ EOF1 in this region are smaller. Increased variance in storm-relative wind direction is present farther west and northwest of the vortex. This gradient is displaced well to the west of the gradient in ζ EOF1 (Fig. 2.11b).

Finally, the forward-flank region to the northeast of the surface vortex differs between these two ensembles, particular with respect to variance in θ'_ρ. In the near-field ensemble, less variability exists and is spatially confined within the core of the storm (Fig. 2.12a). This signal is collocated with a zonally oriented region of larger θ'_ρ present in many near-field members (e.g., Fig. 2.6, all members except for 4, 11, and 13), likely due to evaporative cooling from forward-flank precipitation (e.g., Fig. 2.4). The orientation of the resulting meridional θ'_ρ gradient with respect to storm-relative winds in this region (Fig. 2.12a) is consistent with baroclinic reorientation of vorticity along parcels bound for the

low-level updraft and/or tornado (e.g., Davies-Jones and Brooks 1993). Increased variance exists in the forward-flank in the far-field ensemble in terms of both the magnitude and spatial extent of the θ'_ρ EOF1; this is related to the lack of consistent forward-flank cooling in the far-field ensemble (Fig. 2.7). This also applies to the ten nontornadic far-field members (not shown). As such, it appears that in this region of the storm, critical for processes influencing supercellular tornado potential, more variability exists in the far-field ensemble than in the near-field ensemble.

2.3.4 Low-level vertical pressure perturbation gradient accelerations

In addition to differences in outflow characteristics and storm-scale variability, I have shown that low-level updraft fluxes are much larger in the near-field ensemble than in the far-field ensemble (Fig. 2.8b). To assess factors influencing updraft strength in these simulations, the pressure perturbation field (p') was decomposed into its dynamic (p'_D) and buoyant (p'_B) components. Furthermore, the dynamic component can be expressed as the sum of the linear (p'_L) and nonlinear (p'_{NL}) components. Using these terms, p' can be expressed as

$$p' \propto (e'_{ij})^2 - \frac{1}{2}|\boldsymbol{\omega'}|^2 + 2\left(\frac{\partial w'}{\partial x}\frac{\partial \overline{u}}{\partial z} + \frac{\partial w'}{\partial y}\frac{\partial \overline{v}}{\partial z}\right) - \frac{\partial B}{\partial z} \tag{2.1}$$

where B is the buoyancy, $\overline{u}$ and $\overline{v}$ are the horizontal, base-state wind components, w' is the vertical velocity (note that $\overline{w}$=0), $\boldsymbol{\omega'}$ is the perturbation vorticity, and e'_{ij} is the stress tensor for the perturbation winds (also called the deformation or the rate-of-strain tensor), which is expressed as

$$e'_{ij} = \frac{1}{2}\left(\frac{\partial u'_i}{\partial x_j} + \frac{\partial u'_j}{\partial x_i}\right). \tag{2.2}$$

The first two terms on the right-hand side of Eq. 2.1 contribute to $p_N L'$, the third represents p'_L, and the fourth represents p'_B (Markowski and Richardson 2011, p. 30). Using the methodology of Hastings and Richardson (2016), p'_L and p'_B are solved using Neumann conditions at the lateral boundaries with a discrete cosine transform and boundary conditions at the top and bottom in order to have no vertical accelerations at the surface, $\frac{\partial \pi'_L}{\partial z} = 0$

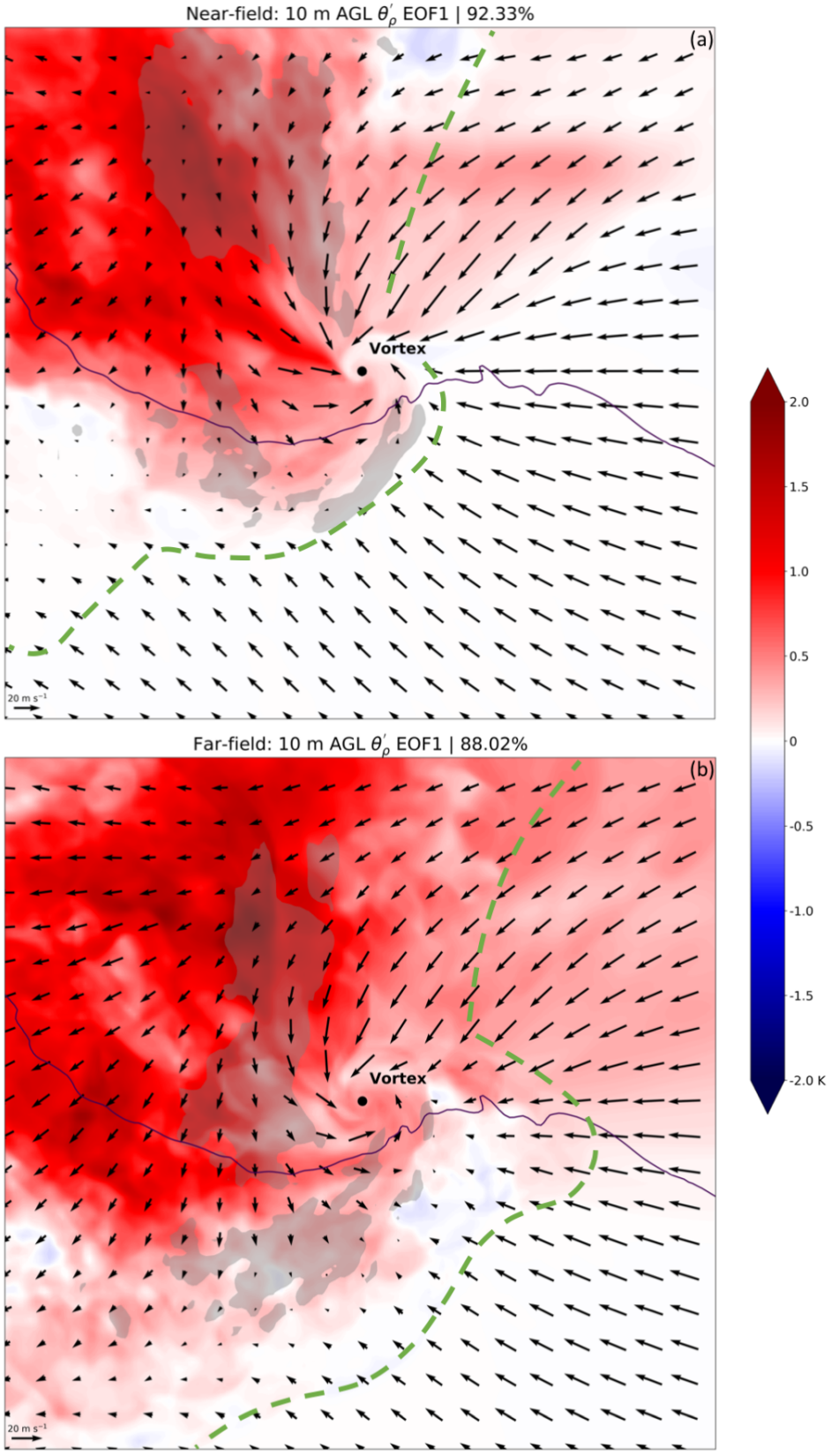

Figure 2.12: (Continued on the following page.)

Figure 2.12: As in Fig. 2.11 except for 10 m AGL θ'_ρ (color fill). The gray shading in each plot indicates regions where the regression of the 10 m AGL wind direction field onto their leading PC timeseries exceeds 50° in each ensemble. Arrows indicate composite, storm-relative 10 m AGL winds for each ensemble at the time of tornadogenesis or tornadogenesis failure. These composite storm-relative wind fields for each ensemble were calculated by averaging the storm-relative winds (centered on the vortex) from all members of that ensemble. The heavy, green dashed lines are identical to those in Fig. 2.11, and the subjectively-drawn green dotted lines in (b) indicate regions to the north of the vortex characterized by weak gradients in the θ'_ρ EOF1 analyses, wind direction EOF1 analyses, and the composite wind fields.

and $c_p\theta_p\frac{\partial\pi'_B}{\partial z} = 0$. Due to non-uniqueness, a constant is added to p'_L and p'_B such that the averages over the domain are zero. p'_{NL} is found as the residual. Lastly, to examine vertical accelerations due to these terms, the vertical pressure perturbation gradient acceleration (VPPGA) for each term is $\frac{-1}{\rho_o}\frac{\partial p'}{\partial z}$, where p' refers to the component of interest. In this case, I calculate 0–1 km AGL VPPGAs and composite them in the ten-minute period leading up to tornado genesis or failure.

0–1 km AGL composite VPPGAs due to p'_{NL} at the time of tornado genesis or failure for the near-field reveal large, positive accelerations arcing around the east side of the developing vortices. These accelerations are due to the presence of (a) the strong low-level updraft causing large vertical vorticity tendencies aloft (i.e., term 2 in Eq. 2.1) and (b) near-surface convergence at the surface associated with the rear-flank gust front (i.e., term 1 in Eq. 2.1). In some instances, negative VPPGAs are collocated with the surface vortex at the time of tornado genesis or failure (e.g., Fig. 2.13c). This signal is due to the development of intense ζ at the surface and a corresponding downward VPPGA due to p'_{NL}. Prior to this

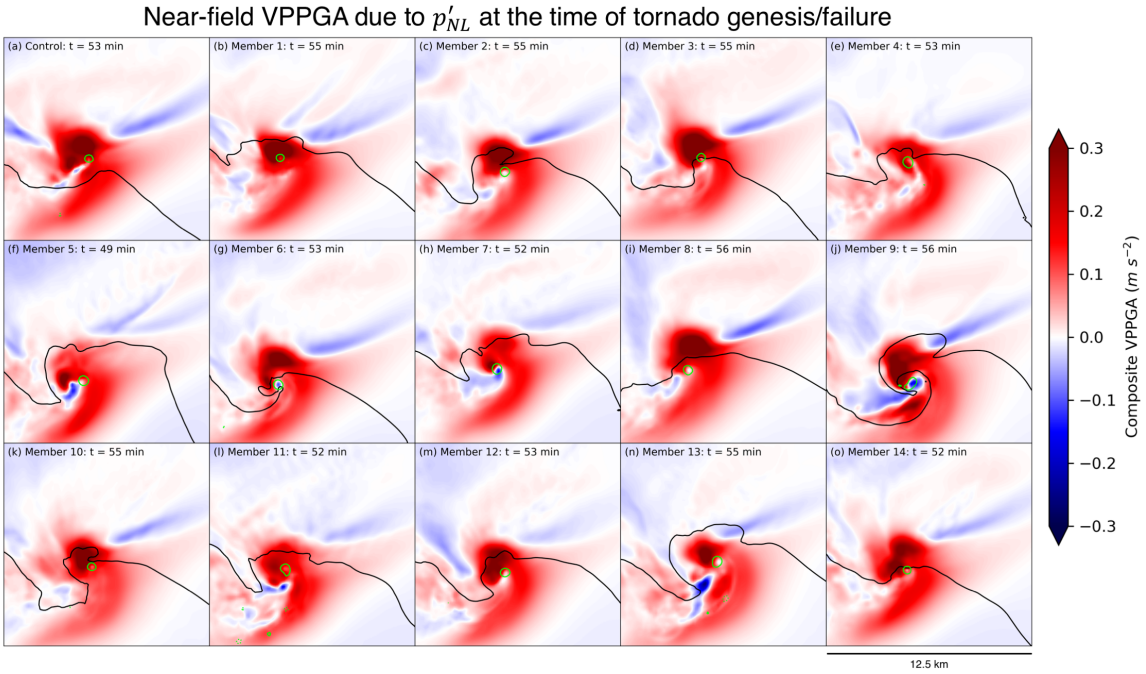

Figure 2.13: Composite vertical pressure perturbation gradient acceleration (VPPGA) due to non-linear, dynamic pressure perturbations (p'_{NL}, shaded) and composite 10 dBZ reflectivity (black contour) in the 15 near-field ensemble members. The VPPGA is composited during the ten minutes preceding tornado genesis or failure. As in Fig. 2.4, variables are plotted at the time of tornado genesis or failure for each member. Surface vertical vorticity exceeding 0.1 s^{-1} at the time of tornado genesis or failure is contoured in green.

signal appearing, these vortices develop within the broader region of positive VPPGAs.

Comparing composite VPPGAs due to p'_{NL} in the far- and near-field ensembles yields striking differences (Figs. 2.13 and 2.14). While the spatial structures of the VPPGAs in the far-field ensemble are similar to those in the near-field ensemble, they are weaker. This results in weaker updrafts less capable of stretching near-surface vertical vorticity to tornadic strength. Within this ensemble, the five tornadic members generally appear to have

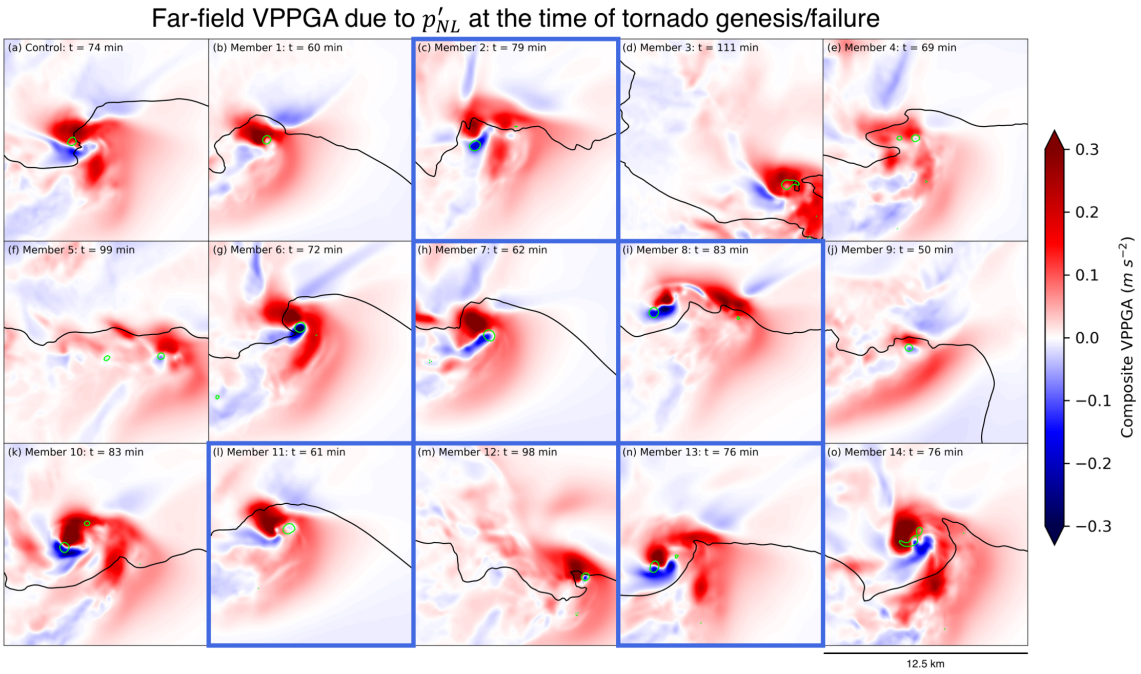

Figure 2.14: As in Fig. 2.13 except for the 15-member far-field ensemble. The five tornadic members are outlined in blue.

stronger VPPGAs due to p'_{NL} than the nontornadic members, although some nontornadic members contain large VPPGFAs as well (e.g., Fig. 2.14k, o).

2.4 Discussion

The near-field ensemble in this study is configured identically to that in Coffer and Parker (2017) except for slight variations in the grid size. All members of the near-field ensemble created in both studies produced tornadoes within minutes of each other, indicating that the error growth arising from infinitesimal differences (like the slight variation in grid size used here) has not yet reached a state in which the storm-scale details are inherently unpredictable. This is typical for cloud-model simulations of supercells up to about two hours (Cintineo and Stensrud 2013). Once supercell simulations reach a state in which differences in storm-scale features, like mesocyclones, arising from very small differences

in the initial state become large on scales of tens of minutes and kilometers, attribution to differences in the initial condition becomes difficult. This underscores the need to use an ensemble approach to ensure representative results (Potvin et al. 2017).

An ensemble approach is also useful for examining the range of possible outcomes, in this case, with respect to storm evolution in a homogeneous environment. Anecdotal evidence is sufficient to state that some environments that seem very supportive of tornadoes may produce none, while others produce outbreaks in which nearly every storm is tornadic. Markowski and Richardson (2017) used this context to ask: "do the storms on these days somehow all have optimal cold pool strengths and shapes (i.e., heat sink characteristics)? [...] Or is there something about some environments—yet to be discovered—that can make storms much less sensitive to the details of their cold pools?" In this case, several storms were simulated in essentially the same environments such that variations between them are attributable to storm-scale variability. The ensembles displayed different magnitudes and modes of variability, especially with respect to surface θ_ρ' (Figs. 2.8c, 2.9b, and 2.12) and low-level updraft characteristics (Figs. 2.8b and 2.9a). Furthermore, although both environments seemed very supportive of tornadoes based on known ingredients, one environment promoted intense surface vortex development and sustenance every time while the other did so much less frequently (e.g., Markowski and Richardson 2017). *In my case, this is due to the production of stronger low-level updrafts and intense dynamic lift as well as the restraint of cold outflow away from the developing surface vortex in the near-field ensemble*. Is it possible that in these cases the low-level updraft becomes so strong that it is able to intensify surface circulations to tornadic strength regardless of any negative buoyancy (i.e., the second question posed above)? Or is this environment capable of restraining colder outflow away from developing vortices such that weaker low-level updrafts are still able to produce tornadoes (i.e., the first question posed above)?

One interesting finding was that it was that the failure of the far-field ensemble to produce tornadoes was not due to an inability to produce strong vortices but rather to *sustain*

them. This may be linked with the presence of surging outflow in a few of the far-field ensemble members. Greater variability in near-surface ζ and θ'_ρ southeast of the vortex (Fig. 2.11) as the gust front in a few members surges there (e.g., Fig. 2.7d,g,m). This would support a rapidly strengthening surface vortex as the gust front "wraps up" beneath the low-level updraft followed by rapid weakening as the surface vortex is surrounded by colder outflow and/or displaced from the overlying low-level updraft. In the near-field ensemble, the coldest outflow air appears more restrained to the northwest of the surface vortex (Fig. 2.6) and would be less likely to negatively influence tornado genesis and maintenance.

The results of this experiment reveal two ensembles that drastically differ in terms of sustained vortices; all members in the near-field ensemble produced tornadoes while only 33% of members in the far-field ensemble produced tornadoes. Given larger low-level directional and speed shear, the near-field wind profile is thought to be more conducive for rapid mesocyclone development and tornado production (Thompson et al. 2007). However, both the near- and far-field soundings were derived from observations in the inflow of tornadic supercells (Parker 2014). Thus, it is interesting that the far-field ensemble only produces tornadoes 33% of the time. Why?

We generally find warmer outflow in the tornadic supercells than the nontornadic supercells. This is consistent with observed outflow temperature deficits in tornadic and nontornadic supercells (Markowski et al. 2002; Grzych et al. 2007; Hirth et al. 2008); however, the deficits in both ensembles in this study are consistent with those observed in the outflow of tornadic supercells. Storm outflow temperature is related to boundary-layer relative humidity in the environment within which the storm resides (e.g., Rasmussen and Blanchard 1998; Rasmussen 2003; Markowski et al. 2003; Thompson et al. 2003; Craven et al. 2004; Markowski and Richardson 2009); higher boundary-layer relative humidity leads to less evaporative cooling within storm-scale downdrafts, resulting in relatively warmer outflow compared to downdrafts experiencing more evaporative cooling (Kumjian 2011; French et al. 2015). Outflow temperature in the vicinity of the surface vortex is also related to

the degree to which the rear-flank gust front is restrained by environmental winds (e.g., Rotunno et al. 1988; Xue 2000; Stensrud et al. 2005; Guarriello et al. 2018). This could explain why the range of θ_ρ' near the vortex in the near-field ensemble was much smaller than that in the far-field ensemble. We also find significantly stronger low-level updrafts in the near-field ensemble, both in the vicinity of the developing vortex and across the entire storm for the duration of the simulations. This finding along with differences in low-level VPPGAs between the two ensembles resembles the findings of Coffer and Parker (2017) and Coffer et al. (2017) with respect to the near-field tornadic and near-field nontornadic composite VORTEX2 soundings (Parker 2014). However, there is a subtle difference in how the VPPGAs are realized. They attributed the stronger updrafts in the near-field tornadic ensemble to larger initial, low-level streamwise horizontal vorticity resulting from a critical angle closer to 90° (i.e. a larger ratio of streamwise to crosswise horizontal vorticity; Esterheld and Giuliano 2008) along parcels bound for the updraft, whereas parcels in the near-field nontornadic ensemble contained less streamwise vorticity because of larger critical angles. While the low-level streamwise vorticity is larger in the entirely-tornadic near-field ensemble here, as it is in Coffer et al. (2017), the larger streamwise vorticity does not result from a critical closer to 90°, but rather larger vertical wind shear and storm-relative winds[6] (Fig. 2.15), resulting from storm-environment modifications (Parker 2014, Wade et al. 2018).

Obviously, the thresholds used to define a "tornado" in these simulations are arbitrary. However, differences in "tornado" production between the ensembles are largely insensitive to variations in all of these thresholds except for the time criteria. If the time criteria (vortex lifetime $\geq$ 2 minutes) is neglected, 12 of 15 far-field members produced a "tornado"; these intense, short-lived vortices may represent observed, short-lived tornadoes. All "tornadoes" in the near-field members, however, last around 15+ minutes. This shows that even if the intense, short-lived vortices in the far-field ensemble are interpreted as

[6]This is consistent with analyses of tornadic and nontornadic proximity soundings in con.

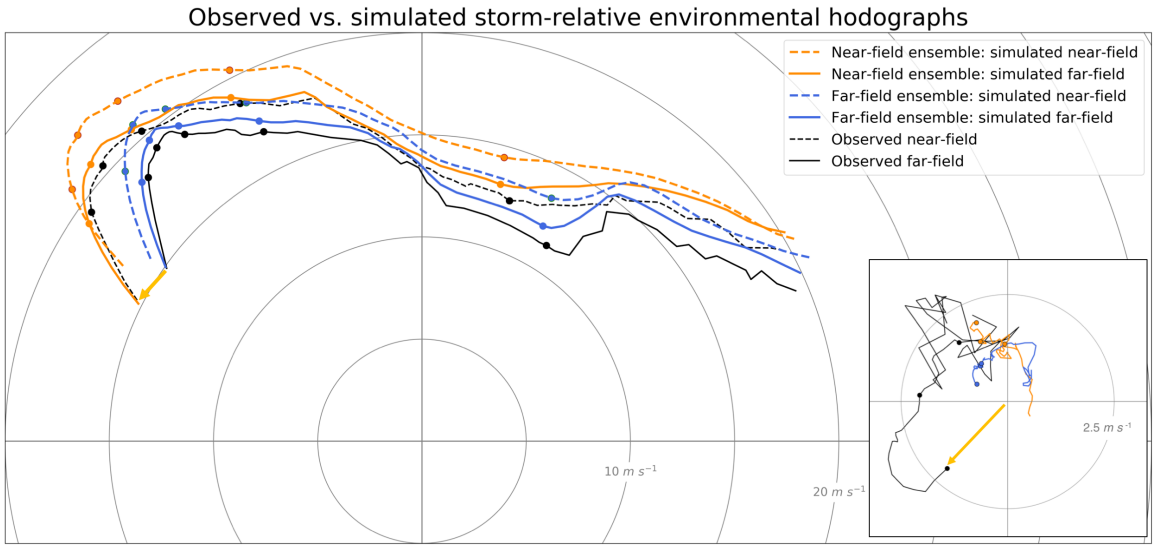

Figure 2.15: Observed (black) and simulated (orange and blue) hodographs in the near- (dashed) and far-field (solid) environments. The observed hodographs (black) are the composite VORTEX2 near- and far-inflow hodographs. These are identical to those plotted in Fig. 2.3 of this study and in Fig. 12 of Parker (2014). Two composite hodographs extracted from the far-field ensemble are plotted in blue, and two extracted from the near-field ensemble are plotted in orange. Each of these four hodographs is a composite of 15 hodographs at either the "near-field" (40 km southeast of the mid-level updraft) or "far-field" (80 km southeast of the mid-level updraft) at the time of tornado genesis or failure for each ensemble member within either ensemble (near-field or far-field). Filled markers indicate heights of 100, 250, 500, 1000, and 3000 m AGL. The hodographs are plotted from 10–6000 m AGL and are storm-relative (i.e., storm motion is at the origin). The inset shows the difference between the near-field and far-field wind components for each case (observations, far-field ensemble, or near-field ensemble) plotted in hodograph-space. The yellow arrow indicates how this difference is plotted. Filled markers in this inset indicate heights of 10, 500, and 1000 m AGL.

tornadoes, significant differences in vortex production exist between the two ensembles, namely in the longevity of the intense surface vortices.

Along these lines, in a separate suite of seven far-field ensemble members emulating the model configuration of Coffer et al. (2017), using 100 m horizontal grid spacing in the inner domain, an updated version of the NSSL microphysics scheme included in release r19.8 of CM1, and an adaptive time step (with a large time step of approximately 1 s during the key time period), all seven members produce tornadoes that meet the definition outlined in Section 2, including many that are as intense as vortices in the near-field ensemble. Further sensitivity tests showed that the shorter time step used herein compared to the adaptive time step in Coffer et al. (2017) possibly leads to increased implicit diffusion within the fifth-order advection scheme and weaker magnitude vortices. In addition to the storm-scale details discussed above, this may explain why vortices in the far-field ensemble do not consistently meet the time criteria outlined in Section 2. While the differences between the near- and far-field ensembles in Section 3 are robust for the given model configuration (i.e., the far-field ensemble has weaker, shorter-lived vortices compared to the near-field ensemble), these sensitivity tests provide further evidence of the arbitrary nature of "tornado" thresholds and the sensitivity of tornadogenesis to seemingly minor model configuration differences in an idealized framework.

Using the near- and far-field tornadic VORTEX2 environments in this study allows us to investigate the impact of these storm-environment modifications (e.g., Nowotarski and Markowski 2016; Wade et al. 2018) on simulated supercell evolution and potential impacts on the volatility of tornadogenesis in each ensemble. The ensemble initialized in the far-field, tornadic environment in this study produced fewer tornadoes than the ensemble initialized in the near-field, nontornadic environment in Coffer et al. (2017). In addition to the fact that the far-field ensemble produced fewer tornadoes than the near-field ensemble, this comparison suggests that *storm-environment feedbacks can create a local environment*

more supportive of tornado potential. The main caveat to this conclusion is that the enhancement of the near-field environment with respect to the far-field may not be solely due to storm-environment interactions. The presence of environmental heterogeneities would play a role as well, especially if an outflow boundary or warm front was present between the near- and far-field profiles. Smaller scale inhomogeneities like horizontal convective roles or gravity waves may also play a role in modulating the near-field environment. Separating these influences from storm-environment modifications was not examined in this study but should be the focus of future work to better understand how storms may modify different environments.

So, did the near-field environment in the simulations evolve in a similar manner? Fig. 2.15 shows that storm-environment modifications to the wind profile are indeed captured in these ensembles. Simulated modifications are similar to those depicted in the near- and far-field composite environments, except in the lowest 1 km AGL. In this layer, modification in the composite near-field resulted in backing and strengthening winds, whereas the simulated modifications resulted in mostly changes in wind speed, not direction. It is not clear why the simulated near-field low-level winds do not back, but it is noteworthy that Wade et al. (2018), in a comparison of near-simultaneous near- and far-field supercell soundings also did not show backing in the near-field winds, only an increase in speed. Therefore, sufficient observational uncertainty still exists on how storms truly modify their environments to know how well CM1 represents these processes.

This study also featured EOF analysis at the time of tornado genesis or failure. To the authors' knowledge, this type of analysis has not previously been performed on high-resolution model output of supercells. The leading modes of variability of ζ, θ_ρ', and wind direction revealed important storm-scale variability (Figs. 2.11 and 2.12). These regions are associated with physical characteristics of the storm, including the locations of storm-generated boundaries and environmental inflow. In particular, the leading EOFs for the near-field ensemble revealed a boundary extending from the vortex northward into the core

of the storm. This boundary was more prominent in the near-field ensemble with a westward gradient in variability of ζ, θ'_ρ, and wind direction (although each of these gradients were not collocated) along with a broad cyclonic wind shift. This is consistent with the presence of a vorticity river or streamwise vorticity current emanating from the core of the supercell and extending southward toward the vortex. These boundaries have been recently identified in multiple supercell simulations and, in some cases, linked with tornado potential. Some preliminary observational studies have showed the possible existence of a vorticity river or SVC in real supercells (e.g., Murdzek et al. 2018; Schueth and Weiss 2018). In both ensembles in this study, especially the near-field ensemble, *this boundary was consistently manifested in near-surface model output and demarcated regions of greater and lesser storm-scale variability in the EOF analyses*.

2.5 Summary

This study addresses the following questions:

1. What patterns of variability exist between storms forming in essentially the same environment?

2. Is the volatility of tornadogenesis different in the near- and far-field VORTEX2 environments?

3. If so, what drives differences in the volatility of tornadogenesis in these environments?

To address these questions, two high-resolution ensembles of simulations were performed using CM1. A horizontal grid spacing of 125 m was sufficient to resolve supercellular low-level mesocyclones and tornado-like vortices. The two 15-member ensembles were created using the near- and far-field tornadic composite environments from VORTEX2 (Parker 2014) and applying small perturbations—within observational error—to the base-state hodographs.

Each member in both ensembles produced a right-moving supercell. Tornado genesis and failure criteria were used to establish the time of these events in each member. All of the near-field members produced a tornado, yet only five of the far-field members produced a tornado. Spatial and temporal composites as well as EOF analyses were created to assess storm-scale variability and features related to the volatility of tornadogenesis in both environments. Based on the results, I present the following conclusions.

- *The range of possible storms, at least in terms of tornado production, differs in different environments. In this case, the volatility of tornadogenesis in the near-field ensemble was much smaller than in the far-field ensemble*.

- *Larger storm-scale variability exists in the far-field ensemble than in the near-field ensemble*. Compared to the near-field ensemble, increased variance in θ'_ρ and surface wind direction were evident primarily to the northeast of the surface vortex, upstream of the low-level mesocyclone.

- *The near-field ensemble contained stronger low-level VPPGAs due to p'_{NL} and warmer outflow in the vicinity of the developing vortex*. This may be linked to differences in the volatility of tornadogenesis between the two ensembles.

- *A storm-scale boundary to the north of the vortex was evident in the near-field ensemble and was not as clear in the far-field ensemble*. In the near-field ensemble, increased variance in θ'_ρ and surface wind directions were present within storm outflow to the west of the boundary and decreased variance was present in storm-cooled inflow air to the east. This is consistent with the location of some boundaries noted in recent high-resolution supercell simulations, including the streamwise vorticity current, vorticity river, and left-flank convergence boundary.

Overall, these findings shed light on the variety of storms that are possible within a given environment with observational error in vertical wind profiles, how those storms vary in terms of storm-scale evolution, and ultimately how that impacts tornado potential

in those environments. A critical assumption in this study is that the differences between the near- and far-field ensembles and conclusions derived from them are solely related to the effects of storm-environment modification. It is possible that environmental heterogeneities were present in the VORTEX2 cases, like outflow boundaries or warm fronts, that also modified the local environment to result in one with enhanced tornado potential. Future work should focus on the representativeness of simulated storm-environment feedbacks (in both research and operational models) and pre-existing mesoscale variability using observed soundings in idealized experiments. Finally, ongoing studies using these ensembles focus on the physical processes influencing the volatility of tornadogenesis, including differences in low-level updraft strength and near-surface characteristics upstream of the mesocyclone.

Chapter 3

Relationships between environmental parameters and evolving supercell motion

3.1 Introduction and Background

The evolution of a supercell thunderstorm and associated severe hazards are strongly related to the background environment within which the storm forms. Given discrete convection initiation, supercell formation is generally expected if the background environment contains sufficient convective available potential energy (CAPE; $\geq$ 1000 J kg^{-1}), vertical wind shear (0–6 km AGL shear $\geq$ 15–20 m s^{-1}), and 0–3 km storm-relative helicity (SRH; $\geq$ 100 m^2 s^{-2}). These general thresholds (not met stringently in all cases) have been found in multiple studies analyzing soundings in the vicinity of supercells (e.g., Rasmussen and Blanchard 1998; Thompson et al. 2003; Craven et al. 2004). These studies also noted additional differences between environments supporting supercells and those supporting ordinary cells or marginal supercells, including lower lifted condensation levels, greater 0–1 km shear magnitudes and upper-tropospheric storm-relative flow, and larger 0–3 km CAPE. These parameters and others derived from them (like the supercell composite parameter, energy helicity index, etc.) are used to predict supercell development days in advance as well as supercell evolution once a storm has formed.

The physical processes driving these relationships have been well explored. Numerous theoretical and numerical studies have shown that increased SRH is associated with greater streamwise horizontal vorticity that, when acted upon by an updraft, is tilted into the vertical within the mid-level mesocyclone (e.g., Lilly 1982; Weisman and Klemp 1982; Davies-Jones 1984; Lilly 1986). In addition to the magnitude of streamwise horizontal vorticity, SRH is also modified by storm-relative wind speed; to this end, greater storm-relative

wind speeds have been shown to increasingly favor supercell development (e.g., Droegemeier et al. 1993; Thompson et al. 2003) by promoting wider updrafts (**?**), which limits the deleterious effects of hydrometeor loading and entrainment (Peters et al. 2019; Peters et al. 2020). Updraft speeds are also influenced by the buoyant accelerations represented by environmental CAPE values. Finally, lower lifted condensation levels are associated with greater boundary-layer relative humidity; all else being equal, this yields greater CAPE and a deeper effective storm-inflow layer. These processes contribute to a stronger, deeper updraft closer to the surface more capable of modifying environmental wind shear to acquire supercellular characteristics.

For obvious reasons, many studies of modeled or observed supercell proximity soundings have focused on differences between tornadic and nontornadic environments. The general consensus is that supercellular tornado potential is largely influenced by boundary-layer humidity and low-level shear; this finding is consistent across multiple observational (e.g., Rasmussen and Blanchard 1998; Rasmussen 2003; Thompson et al. 2003; Craven et al. 2004; Parker 2014; Wade et al. 2018; con) and modeling (e.g., Markowski and Richardson 2014; Coffer and Parker 2017) studies, especially when differentiating between nontornadic and significantly tornadic (EF-2+) supercells.

Less work has focused on the influence of the environment on supercell behavior in time. One defining characteristic of supercells is their longevity, and while they contain single, quasi-steady updrafts during their entire lifespan, changes in storm intensity occur. A few studies have examined how changes in the background environment incite changes in supercell behavior. Richardson et al. (2007) used an idealized framework to examine the influence of horizontally varying environmental vertical shear on updraft development and found that multicell systems intensified into more organized, bow echo structures when the entire storm system moved into increasing shear. Ziegler et al. (2010) used a similar approach to simulate supercell evolution moving from a weakly capped region into a cold boundary layer and inversion region. Some studies have used the base-state substitution

technique (Letkewicz et al. 2013) to examine how temporal changes in the background environment influence a mature supercell (e.g., Coffer and Parker 2015; Davenport and Parker 2015; Davenport et al. 2019). Others have analyzed observations in the vicinity of intensifying or dissipating supercells and attributed these evolutionary paths, including tornado production (e.g., Klees et al. 2016), to changes in environmental SRH, convective inhibition, and vertical wind profiles (e.g., Davenport and Parker 2015; Gropp and Davenport 2018).

This study has a similar goal of relating supercell behavior to environmental characteristics except I specifically focus on the motion of the supercell during the first 1–2 hours after initiation. If storm motion is only influenced by advection, it should align with the mean wind in the layer of the atmosphere that the storm occupies. However, numerous studies have documented the tendency for "large and intense" (Browning 1964) cells to move to the right of the mean wind (e.g., Newton and Katz 1958). This is due to small-scale pressure perturbations that form in the vicinity of the cell, as expressed in Eq. 2.1. Recall that the first two terms on the right-hand side of Eq. 2.1 represent p'_{NL} and the third represents p'_L. In environments with a straight hodograph, p'_L results in cell propagation downshear (Rotunno and Klemp 1982). In a typical environment characterized by some component of southerly flow at all levels, this scenario yields a storm motion to the right of the mean wind and (typically) faster than the mean wind due to the combined effects of advection and propagation. In environments with a clockwise-curving hodograph, p'_L results in both propagation downshear as well as propagation to the right of the mean shear vector (Rotunno and Klemp 1982; Rotunno and Klemp 1985). This scenario yields a storm motion to the right of the mean wind but (typically) slower than the mean wind due to both advection and propagation (see Fig. 3 of Rotunno and Klemp 1982). Finally, p'_{NL} influences storm motion by enhancing both the right and left flanks of the initial updraft. This occurs as initially horizontal vorticity in the environment is tilted upwards along the flanks of the updraft, yielding vertical vorticity maxima (of both signs) aloft. These result in $p'_{NL} < 0$ aloft,

upward-pointing VPPGAs, and enhanced updrafts. The combination of linear and non-linear effects (to some degree) leads to storm-splitting in environments containing veering vertical wind shear (Rotunno and Klemp 1982; Rotunno and Klemp 1985; Weisman and Klemp 1982; Weisman and Klemp 1984); in environments with unidirectional vertical wind shear, the storm split is due entirely to non-linear pressure perturbations.

These processes may occur as early as the first 20–30 minutes after initial cell development, when interactions between the storm-scale updraft and background vertical wind shear result in horizontal pressure perturbation gradients across the cell (Rotunno and Klemp 1982). Rotunno and Klemp (1982) showed that both linear and nonlinear effects influenced cell motion within the first 15 minutes in environments with veering vertical wind shear. They found nonlinear forcing to favor storm splitting and the linear forcing to preferentially favor the right flank, resulting in an "early rightward bias" with respect to the mean wind. In the case of a straight hodograph, cell splitting was attributed solely to nonlinear forcing. In the aforementioned studies, cell splitting was generally noted 20–60 minutes into each simulation (Rotunno and Klemp 1985; Weisman and Klemp 1982; Weisman and Klemp 1984). Numerous studies have examined the motion of supercells after this developmental phase and related it to environmental conditions (Maddox 1976; Colquhoun 1980; Davies and Johns 1993; Davies 1998; Rasmussen and Blanchard 1998). Bunkers storm motion (Bunkers et al. 2000) is typically used today to help anticipate this eventual storm motion and is used to calculate environmental parameters (like SRH) that depend on storm motion.

These topics were revisited in Weisman and Rotunno (2000) in light of discrepencies between storm motion-updraft rotation relationships (e.g., Davies-Jones 1984) and updraft-shear interactions (e.g., Rotunno and Klemp 1982; Rotunno and Klemp 1985). They found that initial cells tended to move generally in the direction of, but slower than, the 0–6 km AGL mean wind during the first 40 minutes (Weisman and Rotunno (2000), see their Fig. 4). By 80 minutes, all cases moved significantly rightward with respect to the mean wind,

"consistent with the development of the rotational updraft after 40 minutes". This is revisited later when they state that the deviant propagation develops within 30–60 minutes "as the nonlinear feedbacks are developing" (Weisman and Rotunno 2000). Ultimately, Weisman and Rotunno (2000) concluded that vertical forcing terms are significantly nonlinear but that the linear terms have more effect as hodograph curvature is added. On the other hand, Davies-Jones (2002) found the nonlinear terms to contribute very little to deviant motion with respect to linear forcing.

Some analysis by Bluestein and Parker (1993) partially addresses observed cell motion and environmental characteristics during the developmental phase of supercells. They analyzed WSR-57 microfilm data from 61 supercells occurring from 1971–1986 to define modes of isolated, severe convection initiating along the dryline in the Southern Plains. Part of their work documented the mean wind, initial cell motion during the first 30 minutes after the first radar echo, and later cell motion in a 40–minute window centered on the time of the first occurrence of severe weather. Fig. 3.1 shows these results grouped by development types (see Fig 1. in Bluestein and Parker 1993), revealing that in all cases the initial cell motion was significantly slower than the 0–6 km AGL pressure-weighted mean wind.

These findings leave questions regarding storm motion during supercell development unanswered, including:

- How long does it take for a developing supercell to turn right? How is this timescale influenced by environmental characteristics?
- Is the initial cell motion (prior to the right turn) generally aligned with the mean wind? Are deviations in initial cell motion from the mean wind related to environmental characteristics?
- Are the answers to the above questions different for supercells destined to be tornadic or nontornadic?

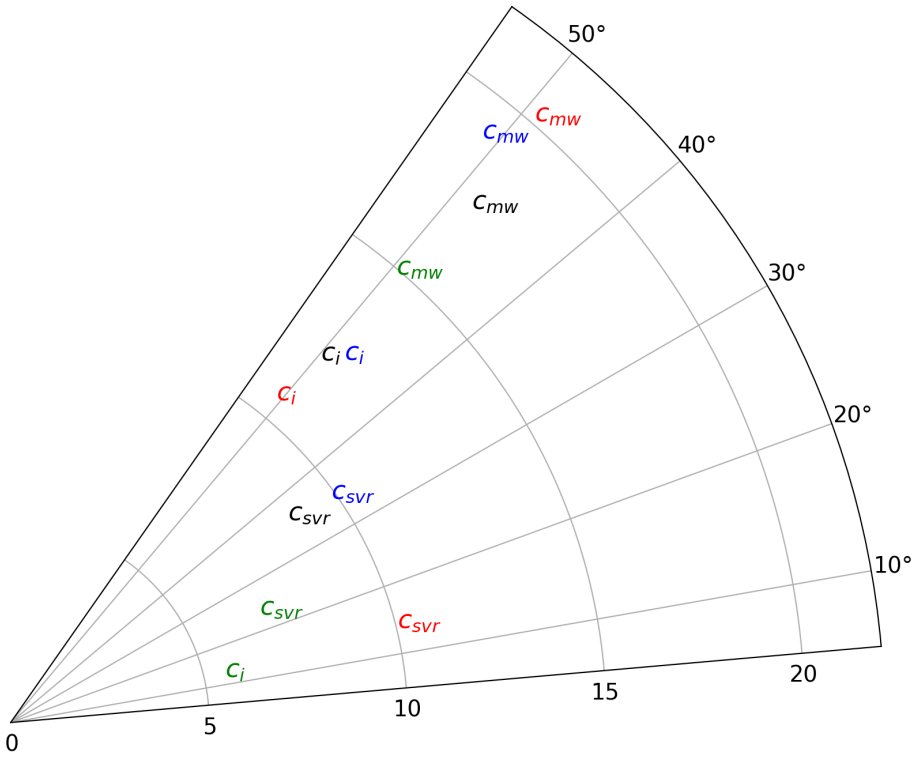

Figure 3.1: Observed supercell storm motions documented by Bluestein and Parker (1993). Subscripts indicate storm motion derived from the 0–6 km AGL pressure weighted mean wind from the closest sounding and surface observations (c_{mw}), observed radar-derived storm motion during the first 30 minutes after the echo appeared (c_i), and observed storm motion averaged over a 40-minute window centered on the time of the first occurrence of severe weather (c_{svr}). Colors indicate the type of supercellular development (see Fig. 1 of Bluestein and Parker 1993); black represents isolated cases (n = 37), red represents pair cases (n = 6), blue represents line segment cases (n = 8), and green represents cluster cases (n = 5).

This study explores these questions using data from a compilation of hundreds of soundings collected during past field experiments (con). These data have greater temporal and vertical resolution than traditional sounding data, thus offering increased precision of environmental parameters in important regions of the atmosphere like the boundary layer. These findings lend insight into physical processes governing these relationships and will compliment experimental products like the NSSL Warn-on-Forecast System to better predict supercell morphology in real-time operations.

3.2 Data and Methods

The main source of data used here includes the compilation of soundings presented in con. This study synthesized data from 902 soundings collected during 13 field campaigns from 1994–2019 in the vicinity of 216 supercells.[1] The data were extensively quality controlled (objectively and manually) and the native 1–2 Hz observations were interpolated to a vertical grid spacing of 10 m, yielding much larger vertical resolution than traditional radiosonde data. con used this novel dataset to assess relationships between the background environment and supercellular tornado potential as well as environmental heterogeneities present in the inflow region of the storm. In this study here, the soundings that are deemed to be representative of the storm environment are used to relate the environment to supercell evolution focusing on the relationships between sounding variables and storm motion at the time of the sounding. Interested readers are referred to con for more information about the construction of this sounding dataset.

This study also makes use of storm track data compiled by con for the 216 supercells mentioned above. WSR-88D level II data was manually scrutinized for each case to ensure that supercell characteristics (e.g., a hook echo, bounded weak echo region, or mesocyclone) persisted for at least 60 minutes. Meeting that criteria, the lat/lon of the supercell

[1] Storm tracks were analyzed for all 220 storms presented in con.

updraft were manually recorded using the NCEI Weather and Climate Toolkit at every volume time (around every 5.5 minutes) from the first echo to when the supercell dissipated or merged with other storms and/or could not be identified. Storm motion was calculated using a 30-minute average of the bearing and great circle distance between successive updraft coordinates, and tornado occurrence or lack thereof was noted at every volume time based on SPC Severe Weather Database files and NWS Storm Data.

A key focus of this study involves the time elapsed between the first echo and the right turn of the storm. Given the sample size (n = 220) and different storm motions within this entire sample, a subjective method based solely on the storm track (i.e., not including environmental information) was used to determine the time at which each storm turned right. This time for each storm was determined independently by myself, Michael Coniglio, and Erik Rasmussen. Of the 220 storms, we agreed exactly on the time of the right turn (or the lack of a right turn) in nearly one third of them (71 storms). In 60% of storms (n = 133), we either all identified no right turn or identified the same right-turn period but were separated in time by no more than 15 minutes. Of the remaining 87 storms, at least one of us failed to agree with the others on either the occurrence of a right turn or the specific time of a right turn (within 15 minutes of the other coauthors).[2] Because of this, the analysis presented in this paper was performed three times, each using the right-turn times identified by a different coauthor. My results do not qualitatively differ across these experiments. Quantitative results differ slightly and are mentioned in the text when they either impact statistical significance or are deemed relevant for operational purposes. Of the 220 supercells in the dataset, the first author found 169 to exhibit clear right turns during their lifespan. The analysis presented here is based off of these right-turn times.

Multiple sounding parameters are evaluated in this study and related to the supercellular right turn, including the pressure-weighted and non-pressure-weighted mean wind in various layers, Bunkers storm motion, surface-based and mixed-layer CAPE and CIN, 0–3

[2]Plots of each storm's track and time of the right turn from each coauthor are available as online supplemental material.

km AGL CAPE, mixed-layer LCL, and kinematic variables in various layers including the mean storm-relative wind speed and streamwise and crosswise horizontal vorticity components. Not every sounding is suitable for calculating all of these variables. In general, sounding data are not used if (a) there are no data below 500 m AGL or (b) data are not available within 100 m of the top of a specified layer (e.g., no data within 2900–3100 m AGL when calculating mean storm-relative wind speed in the 0–3 km AGL layer). To maintain sampling independence, only one sounding is selected in cases for which more than one sounding was launched on a storm. Randomly changing which sounding is selected does not qualitatively change the results. The data are presented in the next section and are broken into two subsets, tornadic and nontornadic. The sounding parameter is considered "tornadic" if it was launched in the vicinity of a supercell that produced a tornado at any point during its life cycle. The number of soundings plotted in each subset are displayed in the upper-right corner of each figure.

3.3 Results

3.3.1 Characteristics of the right turn

General characteristics of the right turn for this collection of 169 supercells are shown in Table 3.2. Across all storms, the mean time of the right turn was 43.8 minutes with a standard deviation of 28.3 minutes. The range of the time of the right turn across all storms was 10–190 minutes. These values did not differ significantly between tornadic (n = 90) and nontornadic (n = 79) supercells. Mean storm motions during the first 20 minutes of the storm's lifecycle (initial), the 20-minute period prior to the time of the right turn (pre-turn), and the 20-minute period following the time of the right turn (post-turn) are also shown. These motions are rotated such that the initial storm motion for each storm is aligned with the x-axis (270°). Tornadic storms tend to move faster than nontornadic storms ($> 1\ m\ s^{-1}$) during the initial, pre-turn, and post-turn phases. Tornadic storms slow slightly

more (around 30%) during the right turn than nontornadic storms, while nontornadic storms exhibit a slightly larger turn to the right of pre-turn motion (by about 2°).

	Time of the right turn (minutes)				Storm motion (m s^{-1} / degrees)			
	Mean	St. Dev.	Min.	Max.	Initial	Pre-turn	Post-turn	Difference
All storms (169)	43.8	28.3	10.0	190.0	12.9 / 270.0	12.8 / 273.3	12.6 / 291.7	-0.19 / -18.3
Tornadic (90)	43.9	30.7	10.0	190.0	13.5 / 270.0	13.3 / 273.2	13.1 / 290.6	-0.21 / 17.4
Nontornadic (79)	43.7	25.2	10.0	145.0	12.2 / 270.0	12.1 / 273.5	12.0 / 292.9	-0.16 / 19.4

Figure 3.2: General characteristics of all storms (n = 169) as well as the tornadic (n = 90) and nontornadic (n = 79) subsets identified using the right-turn times selected by the first author. Storm motions include the storm speed ($m\ s^{-1}$) followed by storm direction (degrees).

The time of tornadogenesis is probably more strongly influenced by storm-scale details (rather than environmental conditions) than the time of the right turn, but some general characteristics of the time of tornadogenesis were examined. Of the 90 tornadic supercells that exhibited a right turn, the mean time from initial cell development to tornadogenesis was roughly 98.72 minutes with a standard deviation of 55.69 minutes. The time of tornadogenesis ranged from as low as 15 minutes after cell development to 285 minutes. Fig. 3.3 shows scatter plots of the time duration between the time of the right turn and the time of tornadogenesis and other storm characteristics, including the change in speed and direction during the right turn as well as the time of the right turn. Do storms that undergo larger changes in direction during the right turn produce tornadoes more quickly after they turn to the right? No. Do storms that undergo larger changes in speed during the right turn produce tornadoes more quickly after they turn to the right? No. Although the mean post-turn speed is less than the mean pre-turn speed for the tornadic supercells (e.g. Table 3.2), many of the storm speeds increased after the right turn. Finally, do storms that take longer to turn to the right produce tornadoes more or less quickly after they finally turn to

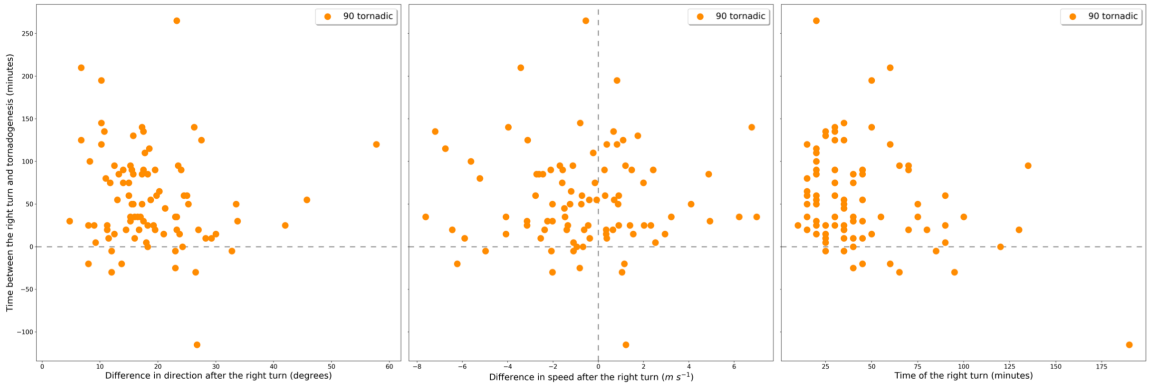

Figure 3.3: Time between the right turn and tornadogenesis plotted against different storm characteristics for the 90 tornadic storms, including (a) difference in direction before and after the right turn, (b) difference in speed before and after the right turn, and (c) the time of the right turn. The differences were calculated by subtracting the mean storm speed or direction in the 20 minutes prior to tornadogenesis from the mean speed or direction in the 20 minutes after tornadogenesis. 11 storms produced a tornado before turning to the right; these storms are plotted in panel (c) but were excluded from the linear regression calculation for this plot.

the right? No. Linearly regressing some of these scatter plots yielded negatively-sloped trend lines, but r^2 values less than 0.01 behoove their omission from these figures.[3]

Thus, it appears that there are no significant differences in the right-turn characteristics described above between tornadic and nontornadic supercells. These findings are not surprising given observed storm-scale similarities between tornadic and nontornadic supercells (e.g., Markowski et al. 2011). Thus far, I have only analyzed storm characteristics and not taken environmental information into account. The influences of different environmental conditions on right-turn characteristics are explored in the next section.

[3]Of the 90 tornadic supercells that exhibited a clear right turn, 79 of them produced a tornado after the right turn and 11 produced a tornado before the right turn. These 11 storms were not included in the analysis relating the time of the right turn to the duration between the right turn and tornadogenesis.

3.3.2 Environmental influences on characteristics of the right turn

If the initial cell is advected by the flow and not influenced by cell propagation, its motion should be close to the mean wind in the vertical layer occupied by the cell. The non-pressure-weighted 0–6 km AGL layer is commonly used here, and is also used in the Bunkers storm motion calculation (Bunkers et al. 2000). Fig. 3.4 shows a kernel density estimation (KDE) of the distributions of initial cell motion for tornadic (orange) and nontornadic (blue) supercells. KDE is a smoothing method that assigns each data point a shape (or "kernel"), which can then be integrated across the domain to produce smoothed, two-dimensional maps (e.g., Anderson-Frey et al. 2016). Rather than showing scatter plots containing hundreds of points, I show KDEs to more clearly show denser regions and differences between distributions. In Fig. 3.4, "initial" motion refers to the average cell motion during the first 20 minutes of its lifespan. Initial cell motion in each case was rotated so that the 0–6 km AGL mean wind pointed along the positive x axis. The mean wind was then subtracted from the initial cell motion in each case. After disregarding soundings with insufficient data for the mean-wind calculation and selecting only one sounding for each storm (to maintain sampling independence), initial cell motions were matched with 184 soundings (94 tornadic and 90 nontornadic)[4]. Fig. 3.4 shows that both tornadic and nontornadic supercells move slower than the mean wind speed during the first 20 minutes of their lifecycle. There is a signal that tornadic supercells move slower (with respect to the mean wind) than nontornadic supercells; in fact, roughly 50% slower (although this difference is not statistically significant). With regard to direction, both tornadic and nontornadic supercells move roughly 1–2 $m\,s^{-1}$ to the right of the 0–6 km AGL pressure-weighted mean wind. This directional deviance is very similar between the tornadic and nontornadic subsets.

[4]For storms near which more than one sounding was launched, changing the sounding used in this analysis does not qualitatively change the results.

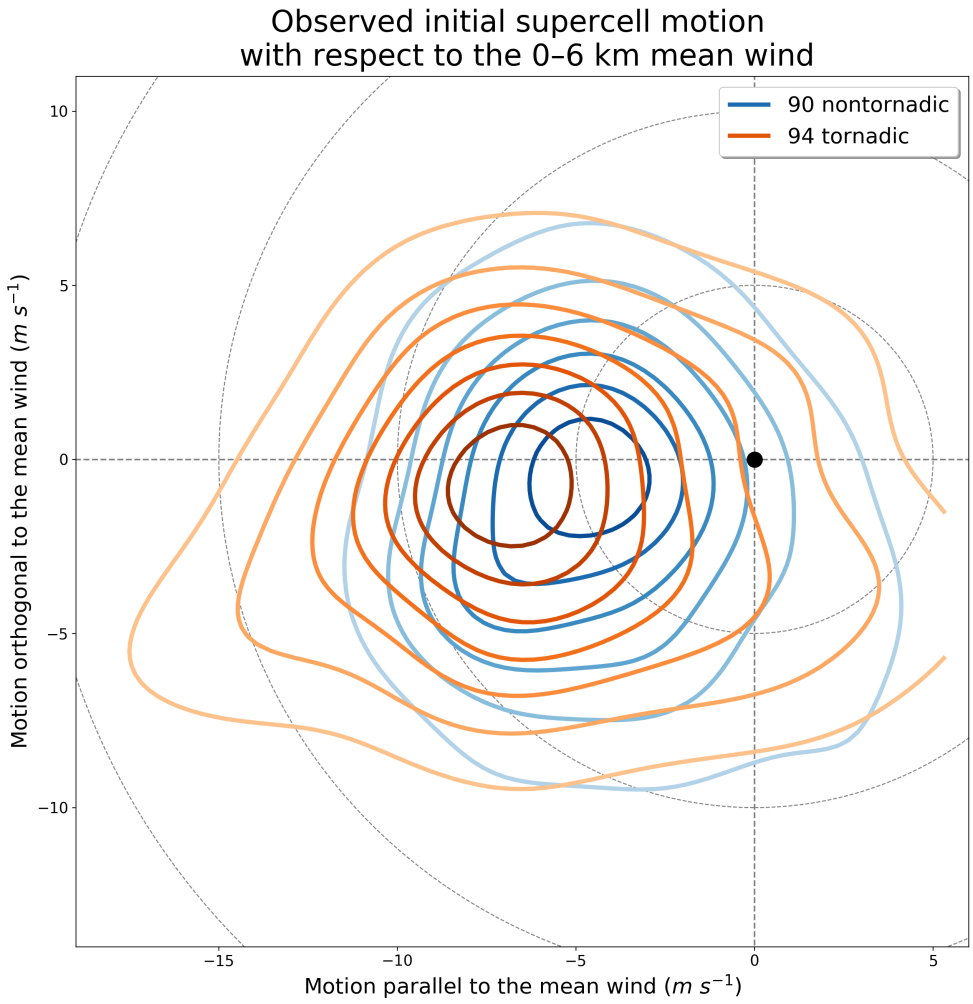

Figure 3.4: Kernel density estimation (KDE) of the initial storm motions of the 90 nontornadic and 94 tornadic supercells with respect to the 0–6 km non-pressure-weighted mean wind. Contours represent constant KDE values, with the maximum density of storm motions for each subset located in each bullseye. The tornadic subset is plotted in red and the nontornadic subset is plotted in blue. Slight color variations across the range are added to highlight maxima and the differences between the subsets. The mean wind was derived from the first available sounding launched on the storm. The black dot at the center of the plot represents the mean wind in each case. Values above and below the x-axis represent initial storm motion to the left or right of the mean wind, respectively, and values to the left or right of the y-axis represent motions that were slower or faster than the mean wind.

The mean wind was calculated in other layers from 0–2 to 0–10 km AGL, both pressure weighted and not, to test their relationship to the initial cell motion. Subjectively, initial cell motions best matched the 0–6 km AGL mean subject to the differences described above. When using layers closer to the surface (e.g., 0–2 and 0–4 km AGL) cells initially moved well to the right of the mean wind, and when using deeper layers (e.g., 0–8 and 0–10 km AGL) cells generally moved in the same direction as the mean wind but storm motions were slower than the mean wind. These trends were expected given characteristically veering wind shear with height and these plots are not shown.

Bunkers storm motion (Bunkers et al. 2000) is commonly used to predict the motion of right- and left-moving supercells in supportive environments using only the environmental wind profile. Fig. 3.5, similar to Fig. 3.4 except normalized around Bunkers right storm motion, shows that Bunkers right storm motion provides a good estimate of the post-turn storm motion (average storm motion during the 20-minute period after the turn) for the supercells in this dataset. This is true for both tornadic and nontornadic supercells. There is a small trend for both tornadic and nontornadic right-moving supercells to move faster than Bunkers storm motion.

3.3.3 Convective available potential energy (CAPE) and inhibition (CIN)

Next, different measurements of CAPE were compared to the time of the right turn. Surface-based CAPE (SBCAPE) and CIN (SBCIN) are shown first (see Fig. 3.6). Of the 902 proximity soundings, 873 were sufficient for calculating SBCAPE and SBCIN, which were then paired with their corresponding tornadic or nontornadic supercell. Of the 169 supercells that exhibited a right turn, sounding data were collected in the vicinity of 165 of them (86 tornadic and 77 nontornadic). To assure independent samples, in cases where more than one sounding was launched on the same storm, SBCAPE and SBCIN from only the first sounding is plotted in Fig. 3.6. If data from this sounding were insufficient to calculate SBCAPE and SBCIN, the next sounding was attempted, and so on. In this case, this

technique yielded SBCAPE and SBCIN calculations in the vicinity of all 165 supercells. Environmental SBCAPE near the tornadic and nontornadic supercells ranges from 0 to > 5000 $J\ kg^{-1}$ while SBCIN ranges from 0 to < -600 $J\ kg^{-1}$. These distributions are similar between the tornadic (orange) and nontornadic (blue) subsets. No clear relationships exist between the amount of SBCAPE or SBCIN and the time of the right turn for either tornadic or nontornadic supercells.

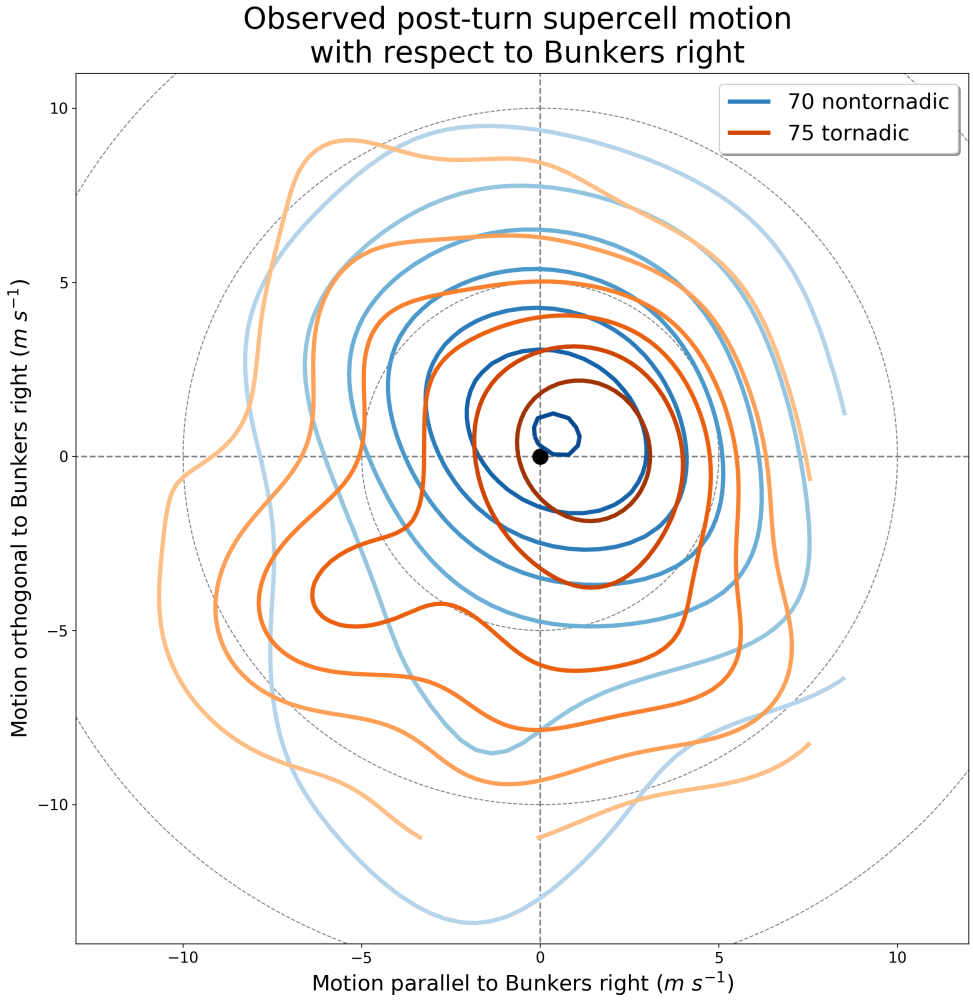

Figure 3.5: As in Fig. 3.4 except for post-turn storm motions compared to Bunkers right storm motion for 70 nontornadic and 75 tornadic storms.

Mixed-layer CAPE (MLCAPE) and CIN (MLCIN), calculated using mixed conditions in the lowest 100 hPa, were evaluated in the same way (Fig. 3.7). The range of MLCAPE values is similar to that of SBCAPE, while MLCIN values range from 0 to around -400 $J\ kg^{-1}$. Based on Fig. 3.7, no clear relationships exist between the amount of MLCAPE or MLCIN and the time of the right turn for either tornadic or nontornadic supercells.

Thinking that the time of the right turn may be more strongly influenced by low-level buoyancy, I examined 0–3 km AGL CAPE next. The surface parcel was used for this calculation, and findings are shown in Fig. 3.8. 0–3 km AGL CAPE values ranged from 0 to 200 $J\ kg^{-1}$, and the distributions of 0–3 km AGL CAPE with respect to the time of the right turn were similar between tornadic and nontornadic supercells. Based on Fig. 3.8, no clear relationships exist between the amount of 0–3 km AGL CAPE and the time of the right turn.

We also examined the possible influence of boundary-layer humidity on the time of the right turn, analyzed here in terms of the mixed-layer lifted condensation level (MLLCL). No significant trends exist (Fig. 3.9), whether outliers are excluded or not (e.g., the sounding with a MLLCL near 4500 m). The means of the MLLCLs in the tornadic (1182 m) and nontornadic (1438 m) subsets are statistically different at the 99% confidence level.

3.3.4 Vertical wind shear

In environments with non-zero crosswise horizontal vorticity, the right turn (or split) of the main updraft occurs as the result of non-linear pressure perturbations (p'_{nl}) enhancing the right and left flanks (with respect to the environmental shear). This occurs as the main updraft tilts initially horizontal vortex lines into the vertical, promoting the maximum collocation of vertical vorticity and vertical velocity along the initial updraft flanks. Subsequently, both flanks are enhanced by p'_{nl} due to fluid extension (in all environments), and the right flank is favored due to p'_{nl} in environments with veering vertical wind shear with height. Thus, I hypothesized that the timing of the right turn would be inversely related to

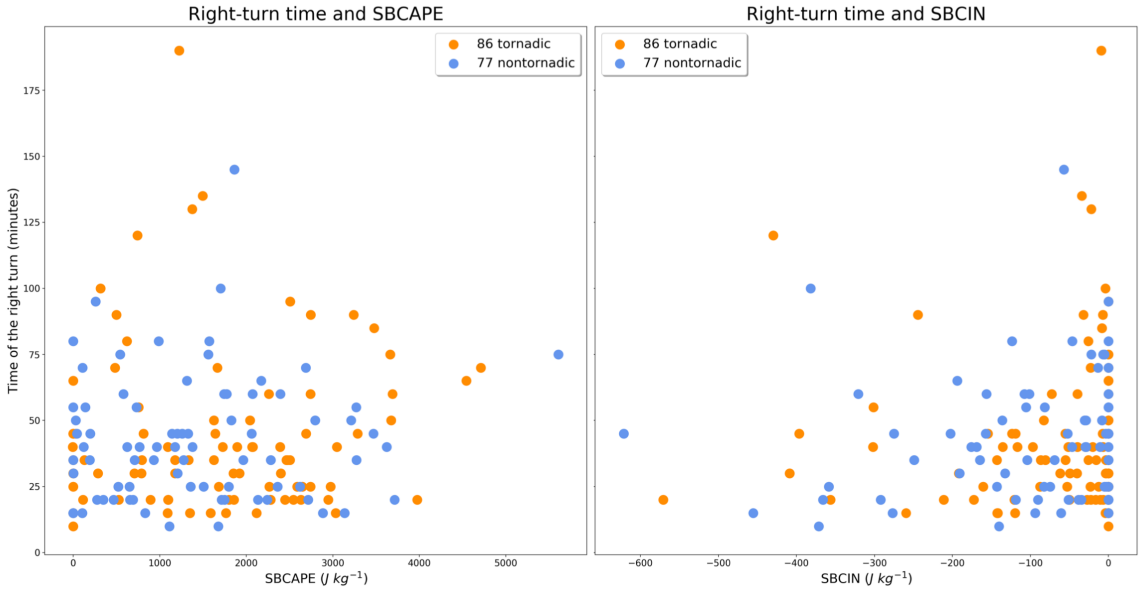

Figure 3.6: Scatter plots showing the time of the right turn against (a) SBCAPE and (b) SBCIN for 86 tornadic and 77 nontornadic storms. Tornadic points are blue, and nontornadic ones are orange.

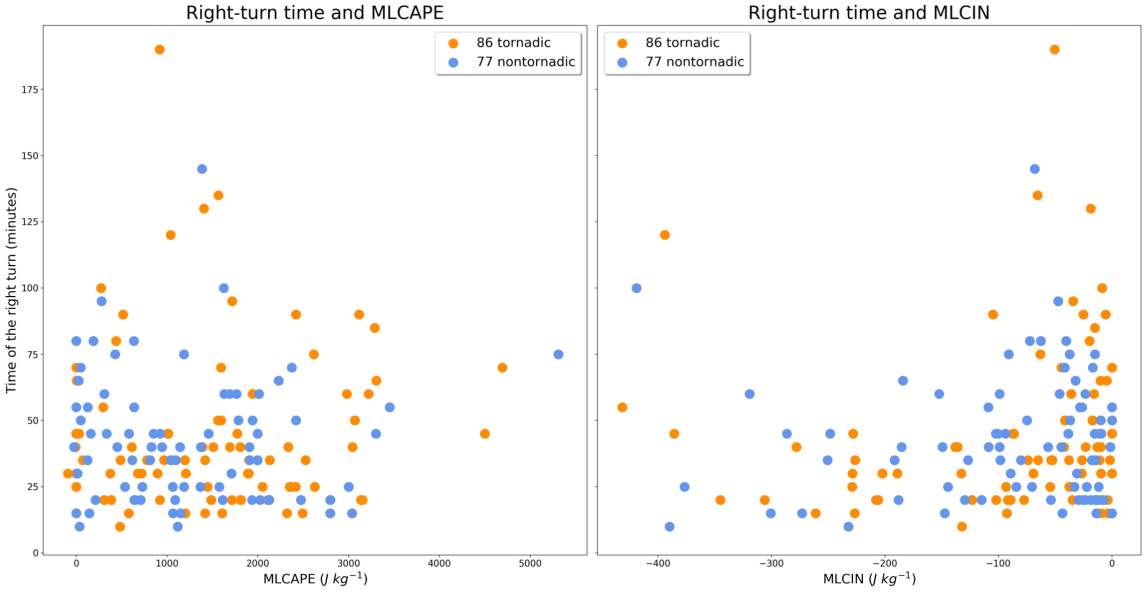

Figure 3.7: As in Fig. 3.6 except for (a) MLCAPE and (b) MLCIN.

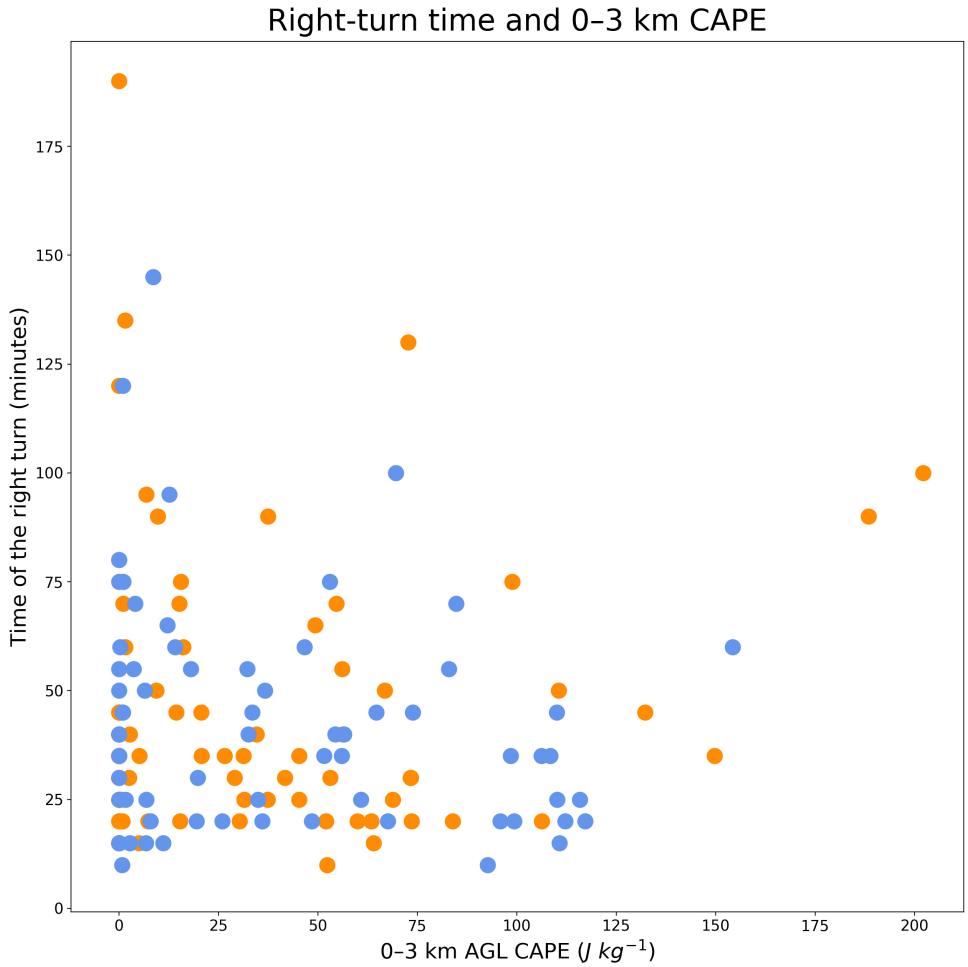

Figure 3.8: As in Fig. 3.7a except for 0–3 km AGL SBCAPE.

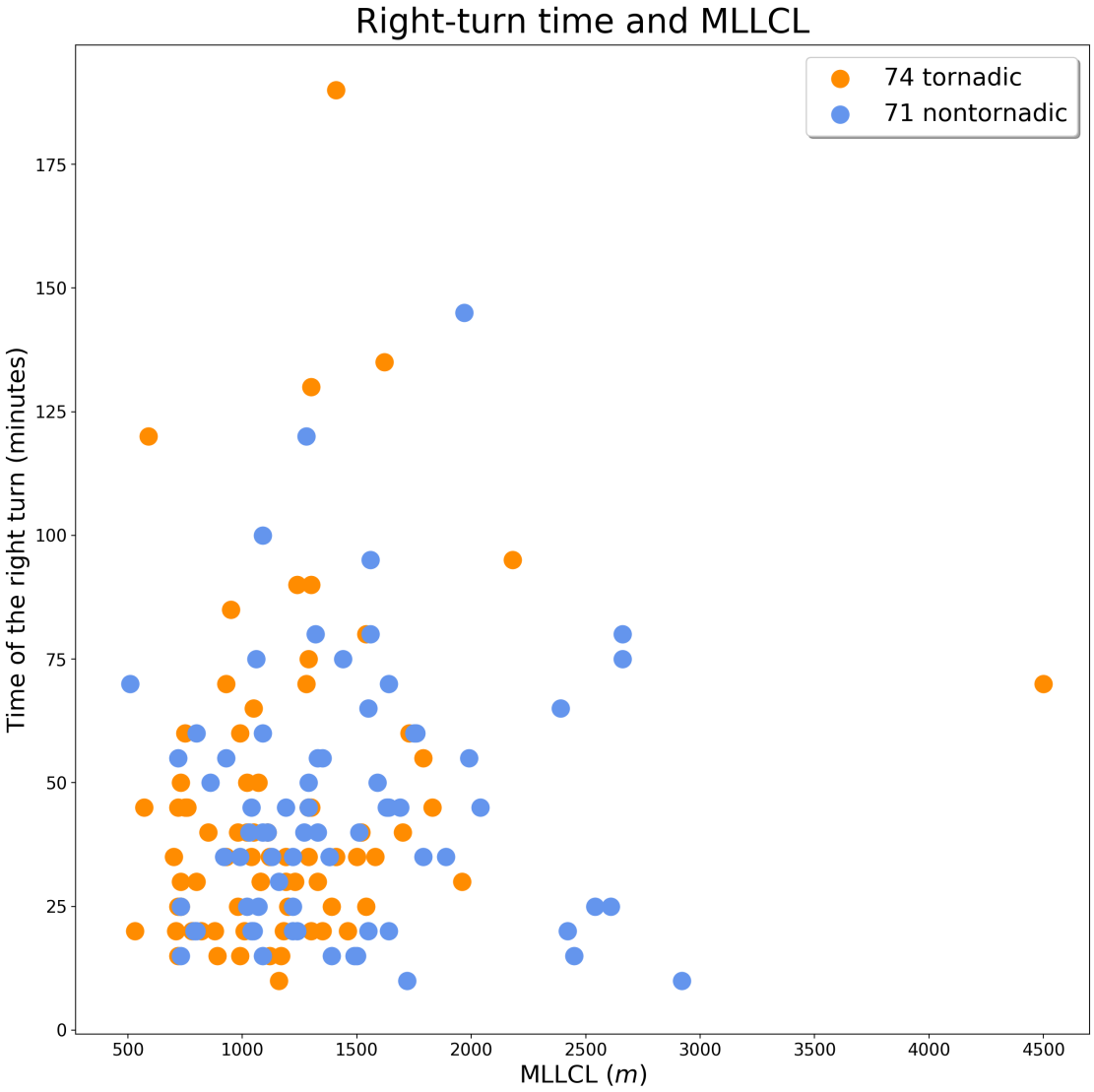

Figure 3.9: As in Fig. 3.8 except for MLLCL.

the amount of initially streamwise, low-level horizontal vorticity in the environment, often measured in terms of storm-relative helicity (SRH). It is important to note that, in addition to streamwise vorticity magnitude, SRH is also a function of storm-relative wind speed and that the separate influences of streamwise vorticity magnitude and storm-relative wind speed may influence supercell characteristics differently (e.g., Peters et al. 2020). I analyze each component separately here. For completeness, I test the hypothesis that the timing of the right turn would be inversely related to the amount of initially crosswise, low-level horizontal vorticity.

Fig. 3.10 shows scatter plots of the time of the right turn in the tornadic and nontornadic supercell subsets with respect to the mean storm-relative wind magnitudes in various layers of the environment. The mean storm-relative wind vector in each layer was found by calculating the layer-mean ground-relative wind vector and subtracting the observed, initial storm motion vector (i.e., the average storm motion vector during the first 20 minutes of the storm's lifespan). In the three layers analyzed, 0–0.5, 0–1, and 0–3 km AGL, there are no statistically significant relationships between the mean storm-relative wind magnitude and the time of the right turn. Storm-relative wind magnitudes decrease with extent from the surface from a mean near 15.0 $m\ s^{-1}$ in the 0–0.5 km AGL layer to roughly 8.2 $m\ s^{-1}$ in the 0–3 km AGL layer (note the difference in the x-axis limits). The differences in mean storm-relative wind magnitudes between the tornadic and nontornadic environments are negligible in the three layers analyzed here.

Streamwise vorticity magnitudes are analyzed next and exhibit a similar correlation (or lack thereof) to the time of the right turn (Fig. 3.11). The mean horizontal vorticity magnitude was found in each layer by calculating the horizontal vorticity vector from the vertical wind profile (assuming no horizontal gradients in w) at each sounding level within the layer and then evaluating the mean. Then, mean streamwise horizontal vorticity was found by projecting the mean horizontal vorticity vector onto the mean storm-relative wind vector. There is no significant relationship between the time of the right turn and mean

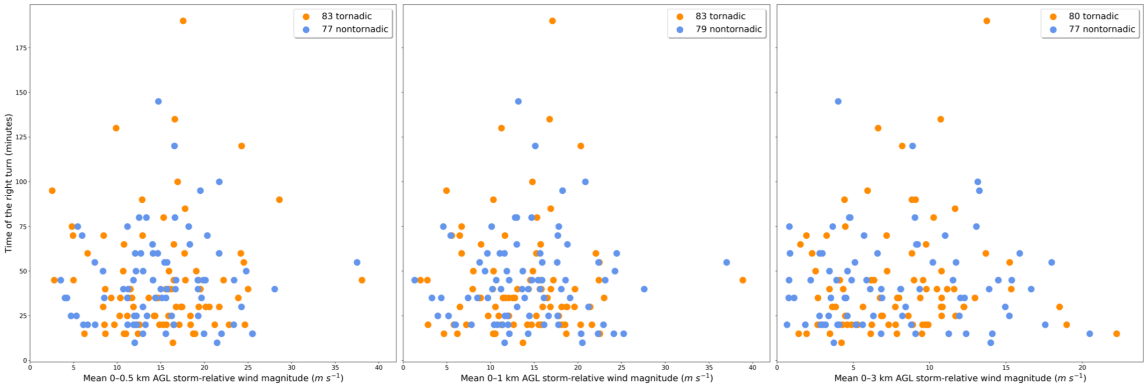

Figure 3.10: As in Fig. 3.9 except for (a) 0–0.5 km AGL, (b) 0–1 km AGL, and (c) 0–3 km AGL mean storm-relative wind magnitude.

streamwise vorticity magnitude in any of the layers shown (0–0.5 km, 0–1 km, and 0–3 km AGL). Again, slightly negative trends are present in some of these layers, especially 0–1 km AGL, but r^2 values are still around 0.02. An interesting result is that, while no significant trend exists, environments containing 0–1 km AGL mean streamwise vorticity of roughly 0.01–0.015 s^{-1} or larger tend to be associated with supercellular right turns roughly 65 minutes or less into the storm's lifecycle. Only one storm exceeds this threshold (turning right at 120 minutes) within this regime. (In the analyses using the right-turn times found by the second and third authors, three or four storms exceed this threshold, but the same qualitative result is consistent.) Mean 0–1 km AGL streamwise vorticity values less than this are associated with a wider range of right-turn times.

Mean streamwise vorticity magnitudes increase in both tornadic and nontornadic environments as the analyzed layer gets thinner and closer to the surface. In fact, horizontal vorticity magnitudes are roughly three times larger in the 0–0.5 km AGL layer than in the 0–3 km AGL layer (0.015 s^{-1} and 0.004 s^{-1}; note the differences in the x-axis limits). Based on two-tailed Monte Carlo tests, the mean streamwise vorticity magnitude in the 0–1 and 0–3 km AGL layers is significantly larger in tornadic environments than in nontornadic environments at the 95% confidence level. Interestingly, the difference in 0–0.5 km AGL

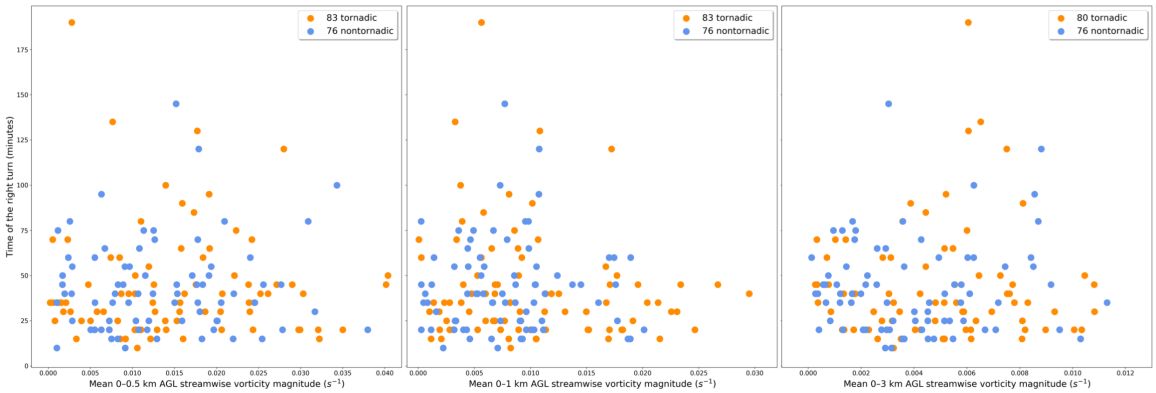

Figure 3.11: As in Fig. 3.10 except for mean streamwise horizontal vorticity magnitude in each layer.

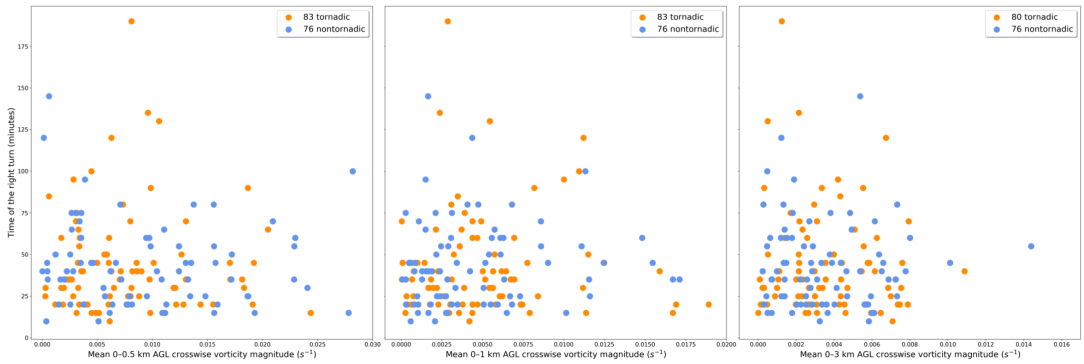

Figure 3.12: As in Fig. 3.11 except for mean crosswise horizontal vorticity magnitude in each layer.

streamwise horizontal vorticity between tornadic and nontornadic environments is not significant. The difference between the tornadic and nontornadic means maximizes in the 0–1 km AGL layer with the tornadic environments containing roughly 0.002 s^{-1} greater mean streamwise horizontal vorticity (0.012 s^{-1} in the tornadic environments and 0.010 s^{-1} in the nontornadic environments). These differences exist in the analyses performed on the right-turn times found by each author.

Is the amount of crosswise vorticity present in the environment related to the time of the right turn? Based on Fig. 3.12, it appears not. Similar to streamwise vorticity, mean crosswise vorticity increases as the analyzed layer gets thinner and closer to the surface. Interestingly, mean crosswise vorticity magnitudes are not significantly different between the tornadic and nontornadic subsets in any of these layers.

3.4 Discussion

Of the 220 supercell tracks in this database, the authors found between 169–211 that turned right. Why didn't all of the supercells turn right? A number of factors influence storm motion, perhaps the most prevalent being the presence of environmental heterogeneities like storm-generated boundaries, fronts, horizontal convective rolls, etc. Boundaries like these are often accompanied by a local maximum in surface vertical vorticity, upward motion, and wind shear, all of which may enhance the environment in terms of supercell potential and alter the storm motion. Spatial or temporal environmental changes may also occur along the storm tracks in the absence of any well-defined boundaries, for example, as the storm gradually moves into a region containing more or less vertical wind shear or CAPE, or as the boundary layer gradually cools and decouples near sunset. Furthermore, intra-storm characteristics like cold pool properties, updraft pulses, precipitation distribution, etc., or influences from other nearby storms all influence supercell motion in a complex manner. In the remaining storms, I hypothesize that some of these factors influenced storm

motion enough to offset the expected impacts of linear and non-linear pressure perturbations.

While it did not influence the findings of this study, it is interesting that such a range of right-turn identifications existed between the three coauthors. Many of the discrepancies were small and still fell within the same general right-turn period. Others did not and involved inflections along the storm track that one or two of us believed was a right turn while the other(s) did not. A somewhat consistent signal was for these disagreements to occur when an inflection in the storm path was present in the first 10–20 minutes of the storm's lifetime. A goal of a future study is identifying under what conditions these "early turns" occur and the physical processes (perhaps related to linear pressure perturbations) responsible for them.

Of the environmental parameters examined here in the vicinity of 169 right-turning tornadic and nontornadic supercells, none exhibited a strong correlation to the time of the right turn. This was not completely surprising given the spread of sounding distances and angles from the target supercell and the fact that storm-environment modifications likely resulted in a somewhat heterogeneous environment across the inflow region (e.g., Wade et al. 2018; con). This would tend to suppress the relationships I seek. To help address this, I performed linear regressions at various distances and angles from the storm across the inflow sector, which did not reveal any significant variations in trends in any particular region (not shown). However, this analysis was not ideal because multiple soundings from the same storm were included (in order to gather sufficient data near each distance and angle from the storm). It's probably more important, though, that this analysis included soundings launched during any phase of the supercell's life cycle. Restraining the sounding analysis by distance and angle from the storm as well as time into the storm's life cycle resulted in insufficient data to examine any relationships. In summary, readers should not conclude from this study that characteristics of the right turn in supercells are not related to environmental conditions. Analysis of soundings in the inflow region targeting specific

phases of the supercell life cycle, specifically the developmental phase, may reveal stronger relationships between environmental parameters and the storm characteristics examined here.

While I did not find significant relationships between the time of the right turn and the amount of streamwise vorticity in various layers of the environment, I did find a general threshold of 0–1 km AGL streamwise vorticity separating groups of storms that either took much more or much less time to turn right (see Fig. 3.11). Environments containing less than around 0.012–0.015 s^{-1} mean streamwise horizontal vorticity supported a larger range of supercell right-turn times than those containing more streamwise vorticity. Except for one tornadic outlier, every storm in an environment characterized by 0.015 s^{-1} mean 0–1 km AGL streamwise horizontal vorticity turned right in 60 minutes or less. Similar analysis of environmental 0–1 km SRH revealed a very similar threshold around 300 m^2 s^{-2}; except for the one tornadic outlier, environments with this much 0–1 km SRH or greater supported right turns within 60 minutes or less. While this should not be interpreted as a hard threshold for supercell right-turn times, this finding is relevant for forecasters predicting supercell development and path in real-time operations.

We also found a lack of a significant difference between low-level crosswise horizontal vorticity in the environments of tornadic and nontornadic supercells. This is interesting given that larger streamwise vorticity (and associated SRH) has long been associated with stronger low-level updrafts in turn supporting increased tornado potential. Some studies like Coffer and Parker (2017) specifically explore the detrimental effects of larger low-level crosswise vorticity on robust low-level mesocyclones. Perhaps the ratio of streamwise to crosswise vorticity is not as important as the total magnitude of streamwise vorticity; this would be consistent with my finding that 0–1 and 0–3 km AGL streamwise vorticity was significantly larger in tornadic than nontornadic environments. This remains an active area of research in the community and further work should continue to explore the physical

processes relating environmental vorticity orientation to low-level mesocyclone characteristics.

On average, the observed storm motion during the first 20 minutes of the storm's life cycle was to the right of the mean wind (pressure-weighted and not) in all layers examined. The fact that developing cells immediately move to the right of the mean wind suggests that linear pressure perturbations largely influence cell motion during this period. In environments with veering vertical wind shear, this process favors updraft propagation downshear as well as to the right of the shear vector. Fig. 3.13 shows a small, negative trend (r^2 near 0.03) between 0–6 km AGL vertical wind shear and the initial cell deviance orthogonal to the mean wind in both the tornadic and nontornadic subsets (correlation coefficient near 0.2 for both). I compared initial cell motions to various wind vector differences, similarly to Fig. 3.4, and found the 0–1.5 km AGL wind vector difference to best align with initial cell motion for both tornadic and nontornadic supercells (see Fig. 3.14). This is plausible given the commonly large shear vectors in this layer collocated with a maximum in updraft speeds within the developing cell, but the physical processes governing this relationship require further investigation.

3.5 Summary

This study analyzed 902 soundings and and 220 storm tracks that were observed during field campaigns from 1994–2019. These soundings contain larger vertical resolution than daily sonde launches, especially in the lowest 1–2 km AGL. This dataset is used to examine relationships between environmental conditions and supercell characteristics, particularly related to the right turn. This study mainly focused on addressing the following questions:

- How long does it take for a developing supercell to turn right? How is this timescale influenced by environmental characteristics?

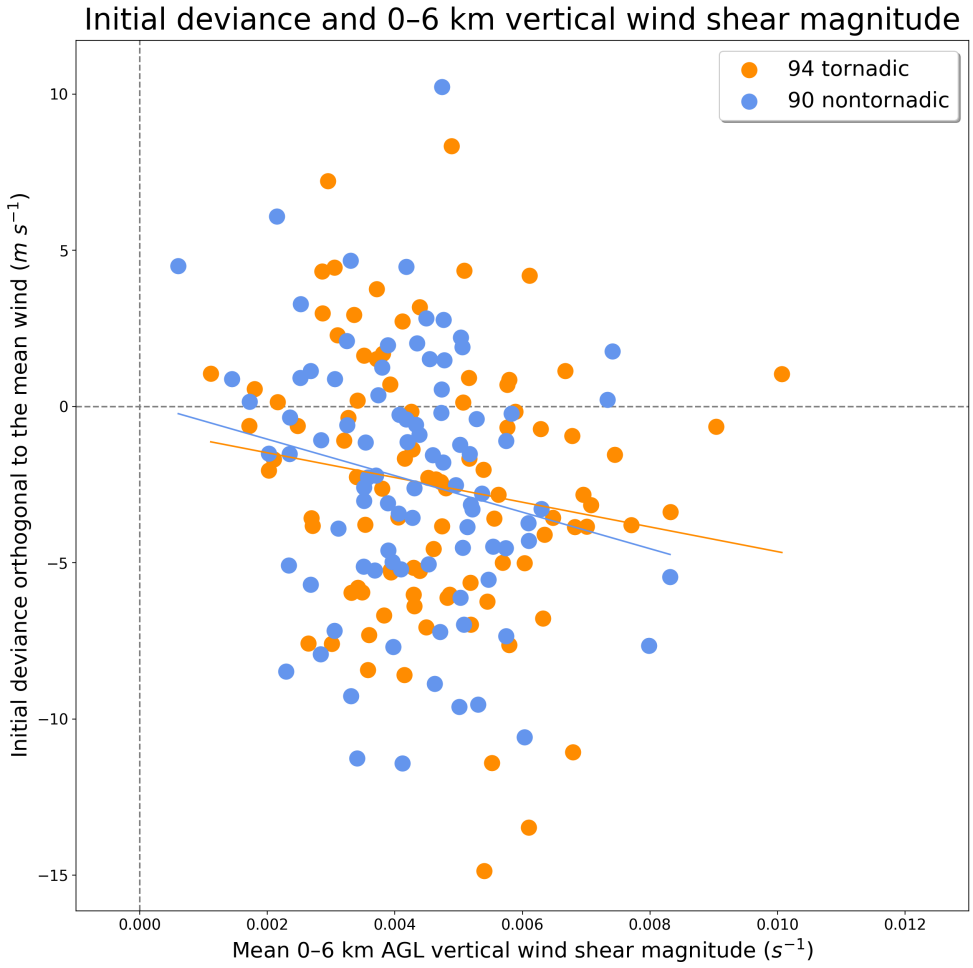

Figure 3.13: Scatter plot of the deviance of the initial cell motion from the mean wind and 0–6 km AGL shear magnitude. Tornadic points are plotted in orange, and nontornadic ones in blue. Negative deviances indicate motion to the right of the mean wind, and positive deviances indicate motion to the left.

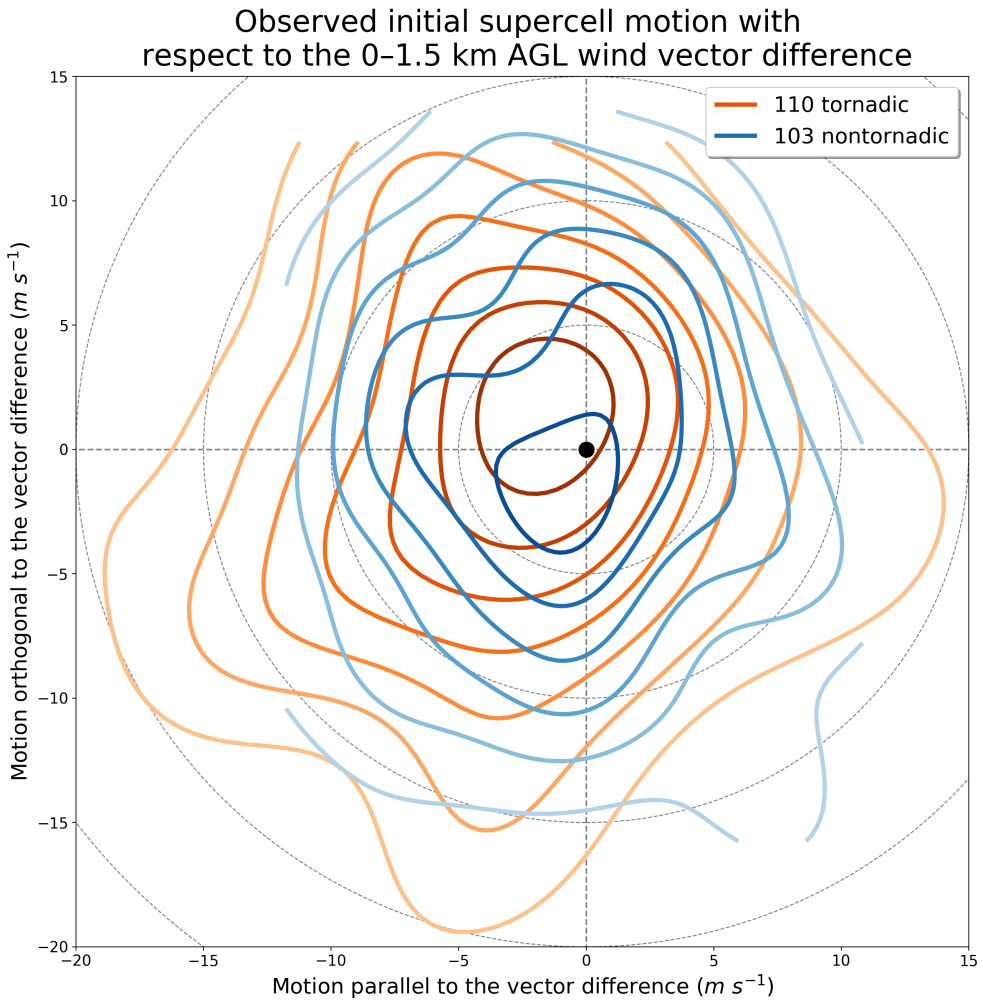

Figure 3.14: As in Fig. 3.4 except for initial cell motions normalized around the 0–1.5 km AGL environmental wind vector difference.

- Is the initial cell motion (prior to the right turn) generally aligned with the mean wind? If not, is the initial cell motion generally related to other environmental conditions?

- Are the answers to the above questions different for supercells destined to be tornadic or nontornadic?

General storm characteristics between tornadic and nontornadic storms were not significantly different. In particular, the time between cell appearance on radar and the right turn was roughly 44 minutes with a standard deviation of 25–30 minutes. On average, storms tended to slow slightly (around 0.2 $m\ s^{-1}$) and deviate 17–20° (with respect to initial motion) during the right turn. These results are readily applicable for operational forecasters, field coordinators, and others in predicting the time of the right turn, resulting storm motion, and development of supercellular hazards.

Initial cell motion is to the right of the mean wind in any layer. This differs from the findings of some other observational studies, like Bluestein and Parker (1993) and Weisman and Rotunno (2000), that found initial cell motion to generally align with the 0–6 km mean wind direction. However, this early rightward deviance is consistent with theory in that linear pressure perturbations act to promote updraft propagation downshear and, in environments with veering vertical wind shear, to the right of the shear vector. Even in environments with a straight hodograph and southerly flow component, linear pressure perturbations due to updraft-in-shear effects will result in initial updraft motion to the right of the mean wind (see Fig. 3.15).[5] Furthermore, given that equal shear magnitudes result in equal vector differences between the mean wind and initial cell motion due to advection and linear propagation, greater ground-relative flow will result in a greater ground-relative angle between the mean wind and initial cell motion. In other words, the degree of initial cell deviance from the 0–6 km mean wind is proportional to ground-relative wind speeds.

[5]In environments with a straight hodograph and northerly flow component, this effect results in initial updraft motion to the left of the mean wind.

This is relevant for predicting the motion of developing supercells in real-time using environmental information.

Consistent with Rotunno and Klemp (1982), this process was evident as early as 20 minutes after the cells first appeared on radar. By this time, cells forming in the curved-hodograph case moved well to the right of the 1.5 km AGL shear vector (Rotunno and Klemp 1982, see their Fig. 6). However, the simulated supercells in Weisman and Rotunno (2000) tended to move in the same direction as the mean wind, but more slowly, during the first 40 minutes and did not turn right until the 40–80 minute time frame. Across the environments composited here, cell motion during the first 20 minutes was best approximated by the 0–1.5 km AGL vector wind difference. This result is relevant for real-time predictions of initial cell motion in supercell environments.

I did not find significant relationships between any environmental parameters examined here and the time of the supercellular right turn. As discussed above, this does not mean that these relationships do not exist. It is possible that these relationships exist on scales that I am unable to resolve in this study, especially temporal ones. This may also be due to the subjective techniques that me, Michael Coniglio, and Erik Rasmussen used to identify the time of the right turn. Soundings close to the storm and prior to the right turn should be examined, but placing those restraints on this dataset yields a sample size too small to detect any meaningful trends.

These findings motivate further examination of environmental conditions and supercell characteristics during their developmental phase. Observations from field campaigns targeting the inflow of developing supercells will be important here. Idealized modelling would be a useful tool to explore these relationships by controlling storm initialization and various environmental conditions of interest. Hopefully, future studies like these will continue to yield insight into how environmental conditions influence supercell development and how these relationships may be useful for real-time prediction up to hours into the future once a cell develops.

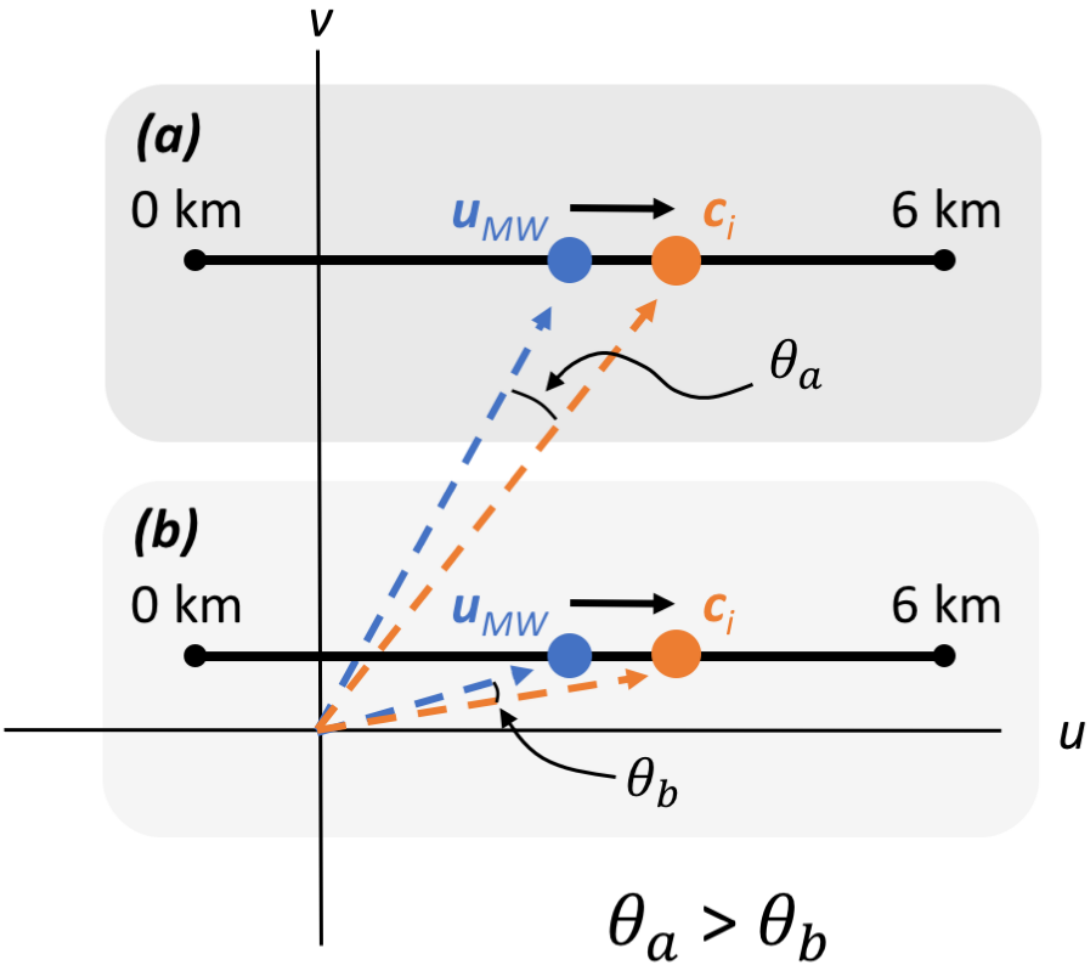

Figure 3.15: Schematic summarizing the effects of advection and linear propagation on initial updraft motion in two idealized, straight-hodograph cases. The shear profiles in (a) and (b) are identical; the only difference is that ground-relative winds are faster in (a). The non-pressure-weighted 0–6 km AGL mean wind is shown indicated by the blue circle. This is the theoretical initial cell motion if it was only influenced by advection (dashed blue arrow). The downshear acceleration due to propagation by linear pressure perturbation effects is indicated by the two small, black arrows. The initial cell motion due to both advection by the mean wind and propagation downshear due to p'_L is indicated by the orange dot and dashed vector (C_i). This yields a greater angle between U_{MW} and C_i for greater ground-relative wind speeds (θ_a) than weaker ground-relative wind speeds (θ_b).

Chapter 4

Conclusions and future work

Multifaceted advancements have been made in our understanding of supercell processes and their relation to the background environment in an effort to better predict supercell hazards. Due to their potentially substantial impacts on damage to property and life, much of this work has focused on discriminating between conditions that support supercellular tornadoes from those that do not. These include studies compositing environments observed in the vicinity of supercells over several years, analyses of high-resolution observations targeting specific region of supercell thunderstorms, theoretical approaches derived from the equations of motion, and high-resolution modelling studies, among others. These findings have yielded relationships between supercellular tornado potential and the background environment as well as the physical processes that may be responsible those relationships. Ultimately, the goal is to then translate these findings to operational communities to increase real-time predictive skill, share more effective products with broadcasters, emergency managers, the public, and other audiences, and ultimately better protect life and property.

The work presented in this dissertation lies in the beginning of that spectrum in identifying how storm-scale characteristics vary in different environments, specifically processes related to tornado potential and other supercellular traits like the time of the right turn. In particular, the following questions were posed:

- What patterns of variability in storm characteristics and tornado potential exist between storms forming in essentially the same environment?

- Is the volatility of tornadogenesis different in the near- and far-field VORTEX2 environments?

- If so, what drives differences in the volatility of tornadogenesis in these environments?

- How long does it take for a developing supercell to turn right? How is this timescale influenced by environmental characteristics?

- Is the initial cell motion (prior to the right turn) generally aligned with the mean wind? Are deviations in initial cell motion from the mean wind related to environmental characteristics?

- How large is the difference between initial cell motion and right-moving supercell motion? How does this difference relate to the difference between the 0–6 km pressure-weighted mean wind and Bunkers estimated storm motion?

- Are the answers to the above questions different for supercells destined to be tornadic or nontornadic?

High-resolution numerical modelling output and novel observational sounding datasets are used to address these questions. The following conclusions are presented from these analyses:

- *Different amounts of storm-scale variability exist in different background environments, ultimately influencing supercellular tornado potential*. Using an idealized framework to control the base-state across two ensembles of supercells, one environment supported tornado production more consistently than the other. That is to say, not every supercell forming in an environment supporting tornado production may become tornadic, and some supercells forming in an environment not as supportive of tornado production may still become tornadic.

- *Environmental controls on the range of intra-storm stochasticity influences the development of storm-scale processes related to tornado potential*. In one environment, greater intra-storm stochasticity occurred and led to more variable updraft strength,

outflow buoyancy, and tornado production. In the other, less intra-storm stochasticity was favored and led to the more consistent development of intense low-level updrafts, warmer surface outflow, and tornadoes. In particular, these storms featured a kinematic and thermodynamic gradient extending northward from the surface vortex into the core of the storm, reminiscent of the location of a left-flank boundary identified in several recent studies.

- *On average, around 45 minutes elapse between the first appearance of a supercell on radar and the time that it turns to the right, with a standard deviation of 25–30 minutes*. This time scale is immediately relevant for better predicting supercell morphology and the development of severe hazards in time.

- *No significant relationships were found between environmental conditions and the time of the supercellular right turn*. This suggests that details like the time of the right turn may be strongly influenced by storm-scale characteristics that aren't strongly related to environmental conditions. Small-scale environmental inhomogeneities that are difficult to observe may also play a large role in the time of the right turn. More targeted observations of the environment near the developing storm before it turns to the right may yield more significant relationships.

- *Initial cell motion (prior to the right turn) tended to best align with the environmental 0–1.5 km AGL shear vector*. This is consistent with theoretical work showing enhanced vertical forcing downshear of an updraft due to linear pressure perturbations. This finding is relevant for forecasting the motion of cells developing in environments supportive of supercells.

These results are significant with respect to previous studies of supercellular environments and tornado potential in that they address *the variability of storm-scale processes within certain environments and especially the time scales on which these processes operate*. The modelling approach here was the first to examine the variability of tornado

production in supercells due to storm-environment modification (assuming that no storm-external boundaries were present between the near- and far-field). I found that, in the case of the VORTEX2 composite environment, storm-environment modifications yielded a local environment much more favorable for tornado production near the supercell. The observational analysis here was the first to synthesize supercell track with high-resolution sounding data collected during field campaigns, specifically related to characteristics of the supercellular right turn. I found the average time scale between convective initiation and the right turn, a possible relationship between environmental streamwise vorticity and the time of the right turn, and interesting differences between tornadic and nontornadic environments that warrant further investigation.

The multifaceted observational- and modelling-based research approach here will continue to be used in the future to explore relationships between supercellular environments, storm-scale characteristics, and tornado potential. From an observational standpoint, several datasets exist (or are possible to collect in the short-term) that will be useful. Near- and far-field environmental sounding data will continue to be collected during the second phase of the TORUS field campaign and hopefully after that in future campaigns. Analyzing these soundings will increase our understanding of how supercells modify their environments, the degree to which these modifications depend on supercell and environmental characteristics, and the physical processes responsible for these modifications. Low-level, in-situ observations were collected from the Windsond platform during the first field phase of TORUS and will continue next year. These missions target the forward-flank of supercells in search of storm-scale boundaries (like the one noted in the modelling study presented here) and characteristics influencing the strength of the low-level updraft and associated tornado potential. Lidar data will also continue to be collected in the near- and far-field of supercells, providing high-resolution observations of temporal variations in the boundary layer as the storm approaches. These data may be supplemented by data from

mobile mesonet platforms and unmanned aircraft systems to effectively diagnose the state of the boundary layer within supercell inflow.

Short-term modelling efforts will continue to use the two ensembles of supercells presented here to identify the physical processes influencing tornado production (or the lack thereof) across the two environments. Are the relevant processes different between the two environments, and are they different between different storms within the same environment? How do these processes influence storm organization to increase tornado potential? Future work will also focus on examining influences on supercell morphology, especially during the developmental period. In particular, controls on convective initiation and environmental conditions will be performed to diagnose the relative effects of intra-storm and environmental details on supercell characteristics, like the time of the right turn.

There are some avenues for theoretical work as well, namely in diagnosing the relative influences of various forcing terms on supercell right-turn characteristics and cell motion. Producing an analytical model for these storm-scale details would yield insight into what terms may be more important in different environments and result in different storm behaviors.

Ultimately, this work continues previous efforts to better understand relationships between the environments, storm-scale characteristics, and tornado potential of supercell thunderstorms. In an effort to more directly contribute to forecast skill, conclusions were drawn that most directly relate to operational forecasting. More studies like these should be encouraged in the future to relate theoretical findings to forecasting techniques and product issuance to different audiences before and during severe weather events.

Bibliography

, ????: Insights into supercells and their environments from three decades of targeted radiosonde observations.

Anderson-Frey, A. K., Y. P. Richardson, A. R. Dean, R. L. Thompson, and B. T. Smith, 2016: Investigation of near-storm environments for tornado events and warnings. *Weather and Forecasting*, **31 (6)**, 1771–1790.

Barnes, S. L., 1978: Oklahoma thunderstorms on 29–30 april 1970. part i: Morphology of a tornadic storm. *Monthly Weather Review*, **106 (5)**, 673–684.

Beck, J., and C. Weiss, 2013: An assessment of low-level baroclinity and vorticity within a simulated supercell. *Monthly weather review*, **141 (2)**, 649–669.

Bluestein, H. B., and S. S. Parker, 1993: Modes of isolated, severe convective storm formation along the dryline. *Monthly weather review*, **121 (5)**, 1354–1372.

Blumberg, W. G., K. T. Halbert, T. A. Supinie, P. T. Marsh, R. L. Thompson, and J. A. Hart, 2017: Sharppy: An open-source sounding analysis toolkit for the atmospheric sciences. *Bulletin of the American Meteorological Society*, **98 (8)**, 1625–1636.

Bretherton, C. S., C. Smith, and J. M. Wallace, 1992: An intercomparison of methods for finding coupled patterns in climate data. *Journal of climate*, **5 (6)**, 541–560.

Brown, M., and C. J. Nowotarski, 2019: The influence of lifting condensation level on low-level outflow and rotation in simulated supercell thunderstorms. *Journal of the Atmospheric Sciences*, **76 (5)**, 1349–1372.

Browning, K. A., 1964: Airflow and precipitation trajectories within severe local storms which travel to the right of the winds. *Journal of the Atmospheric Sciences*, **21 (6)**, 634–639.

Browning, K. A., and F. Ludlam, 1962: Airflow in convective storms. *Quarterly Journal of the Royal Meteorological Society*, **88 (376)**, 117–135.

Bryan, G. H., and J. M. Fritsch, 2002: A benchmark simulation for moist nonhydrostatic numerical models. *Monthly Weather Review*, **130 (12)**, 2917–2928.

Bunkers, M. J., B. A. Klimowski, J. W. Zeitler, R. L. Thompson, and M. L. Weisman, 2000: Predicting supercell motion using a new hodograph technique. *Weather and forecasting*, **15 (1)**, 61–79.

Cintineo, R. M., and D. J. Stensrud, 2013: On the predictability of supercell thunderstorm evolution. *Journal of the atmospheric sciences*, **70 (7)**, 1993–2011.

Coffer, B. E., and M. D. Parker, 2015: Impacts of increasing low-level shear on supercells during the early evening transition. *Monthly Weather Review*, **143 (5)**, 1945–1969.

Coffer, B. E., and M. D. Parker, 2017: Simulated supercells in nontornadic and tornadic vortex2 environments. *Monthly Weather Review*, **145 (1)**, 149–180.

Coffer, B. E., and M. D. Parker, 2018: Is there a "tipping point" between simulated nontornadic and tornadic supercells in vortex2 environments? *Monthly Weather Review*, **146 (8)**, 2667–2693.

Coffer, B. E., M. D. Parker, J. M. Dahl, L. J. Wicker, and A. J. Clark, 2017: Volatility of tornadogenesis: An ensemble of simulated nontornadic and tornadic supercells in vortex2 environments. *Monthly Weather Review*, **145 (11)**, 4605–4625.

Coffer, B. E., M. D. Parker, R. L. Thompson, B. T. Smith, and R. E. Jewell, 2019: Using near-ground storm relative helicity in supercell tornado forecasting. *Weather and Forecasting*, **34 (5)**, 1417–1435.

Colquhoun, J., 1980: A method of estimating the velocity of a severe thunderstorm using the vertical wind profile in the storm's environment. *Conference on Weather Forecasting and Analysis, 8 th, Denver, CO*, 316–323.

Craven, J. P., H. E. Brooks, J. A. Hart, and Coauthors, 2004: Baseline climatology of sounding derived parameters associated with deep, moist convection. *Natl. Wea. Dig*, **28 (1)**, 13–24.

Dahl, J. M., 2017: Tilting of horizontal shear vorticity and the development of updraft rotation in supercell thunderstorms. *Journal of the Atmospheric Sciences*, **74 (9)**, 2997–3020.

Dahl, J. M., M. D. Parker, and L. J. Wicker, 2014: Imported and storm-generated near-ground vertical vorticity in a simulated supercell. *Journal of the Atmospheric Sciences*, **71 (8)**, 3027–3051.

Davenport, C. E., and M. D. Parker, 2015: Impact of environmental heterogeneity on the dynamics of a dissipating supercell thunderstorm. *Monthly Weather Review*, **143 (10)**, 4244–4277.

Davenport, C. E., C. L. Ziegler, and M. I. Biggerstaff, 2019: Creating a more realistic idealized supercell thunderstorm evolution via incorporation of base-state environmental variability. *Monthly Weather Review*, **147 (11)**, 4177–4198.

Davies, J. M., 1998: On supercell motion in weaker wind environments. *Preprints, 19th Conf. on Severe Local Storms, Minneapolis, MN, Amer. Meteor. Soc*, 685–688.

Davies, J. M., and R. H. Johns, 1993: Some wind and instability parameters associated with strong and violent tornadoes: 1. wind shear and helicity. *GMS*, **79**, 573–582.

Davies-Jones, R., 1982a: Observational and theoretical aspects of tornadogenesis. *Intense Atmospheric Vortices*, Springer, 175–189.

Davies-Jones, R., 1984: Streamwise vorticity: The origin of updraft rotation in supercell storms. *Journal of the atmospheric sciences*, **41 (20)**, 2991–3006.

Davies-Jones, R., 2002: Linear and nonlinear propagation of supercell storms. *Journal of the atmospheric sciences*, **59 (22)**, 3178–3205.

Davies-Jones, R., 2015: A review of supercell and tornado dynamics. *Atmospheric Research*, **158**, 274–291.

Davies-Jones, R., and H. Brooks, 1993: Mesocyclogenesis from a theoretical perspective. *Washington DC American Geophysical Union Geophysical Monograph Series*, **79**, 105–114.

Davies-Jones, R. P., 1982b: A new look at the vorticity equation with application to tornadogenesis. *Preprints, 12th Conf. on Severe Local Storms, San Antonio, TX, Amer. Meteor. Soc*, Vol. 249252.

Dawson II, D. T., L. J. Wicker, E. R. Mansell, and R. L. Tanamachi, 2012: Impact of the environmental low-level wind profile on ensemble forecasts of the 4 may 2007 greensburg, kansas, tornadic storm and associated mesocyclones. *Monthly Weather Review*, **140 (2)**, 696–716.

Doswell, C. A., and D. W. Burgess, 1993: Tornadoes and tornadic storms: A review of conceptual models. *Geophysical Monograph-American Geophysical Union*, **79**, 161–161.

Doswell III, C. A., A. R. Moller, and H. E. Brooks, 1999: Storm spotting and public awareness since the first tornado forecasts of 1948. *Weather and forecasting*, **14 (4)**, 544–557.

Droegemeier, K. K., S. M. Lazarus, and R. Davies-Jones, 1993: The influence of helicity on numerically simulated convective storms. *Monthly weather review*, **121 (7)**, 2005–2029.

Esterheld, J. M., and D. J. Giuliano, 2008: Discriminating between tornadic and non-tornadic supercells: A new hodograph technique. *E-Journal of Severe Storms Meteorology*, **3 (2)**.

French, M. M., P. S. Skinner, L. J. Wicker, and H. B. Bluestein, 2015: Documenting a rare tornado merger observed in the 24 may 2011 el reno–piedmont, oklahoma, supercell. *Monthly Weather Review*, **143 (8)**, 3025–3043.

Glickman, T., and Z. Walter, 2000: Glossary of meteorology. amer. meteor. soc., 855 pp.

Gropp, M. E., and C. E. Davenport, 2018: The impact of the nocturnal transition on the lifetime and evolution of supercell thunderstorms in the great plains. *Weather and Forecasting*, **33 (4)**, 1045–1061.

Grzych, M. L., B. D. Lee, and C. A. Finley, 2007: Thermodynamic analysis of supercell rear-flank downdrafts from project answers. *Monthly weather review*, **135 (1)**, 240–246.

Guarriello, F., C. J. Nowotarski, and C. C. Epifanio, 2018: Effects of the low-level wind profile on outflow position and near-surface vertical vorticity in simulated supercell thunderstorms. *Journal of the Atmospheric Sciences*, **75 (3)**, 731–753.

Hastings, R., and Y. Richardson, 2016: Long-term morphological changes in simulated supercells following mergers with nascent supercells in directionally varying shear. *Monthly Weather Review*, **144 (2)**, 471–499.

Hirth, B. D., J. L. Schroeder, and C. C. Weiss, 2008: Surface analysis of the rear-flank downdraft outflow in two tornadic supercells. *Monthly weather review*, **136 (7)**, 2344–2363.

Klees, A. M., Y. P. Richardson, P. M. Markowski, C. Weiss, J. M. Wurman, and K. K. Kosiba, 2016: Comparison of the tornadic and nontornadic supercells intercepted by vortex2 on 10 june 2010. *Monthly Weather Review*, **144 (9)**, 3201–3231.

Klemp, J. B., and R. Rotunno, 1983: A study of the tornadic region within a supercell thunderstorm. *Journal of the Atmospheric Sciences*, **40 (2)**, 359–377.

Kumjian, M., 2011: Precipitation properties of supercell hook echoes. *E-Journal of Severe Storms Meteorology*, **6 (5)**.

Lemon, L. R., and C. A. Doswell III, 1979: Severe thunderstorm evolution and mesocyclone structure as related to tornadogenesis. *Monthly Weather Review*, **107 (9)**, 1184–1197.

Letkewicz, C. E., A. J. French, and M. D. Parker, 2013: Base-state substitution: An idealized modeling technique for approximating environmental variability. *Monthly weather review*, **141 (9)**, 3062–3086.

Lilly, D., 1982: The development and maintenance of rotation in convective storms. *Intense Atmospheric Vortices*, Springer, 149–160.

Lilly, D. K., 1986: The structure, energetics and propagation of rotating convective storms. part ii: Helicity and storm stabilization. *Journal of the atmospheric sciences*, **43 (2)**, 126–140.

Lorenz, E. N., 1956: Empirical orthogonal functions and statistical weather prediction.

Maddox, R. A., 1976: An evaluation of tornado proximity wind and stability data. *Monthly Weather Review*, **104 (2)**, 133–142.

Mansell, E. R., 2010: On sedimentation and advection in multimoment bulk microphysics. *Journal of the atmospheric sciences*, **67 (9)**, 3084–3094.

Mansell, E. R., C. L. Ziegler, and E. C. Bruning, 2010: Simulated electrification of a small thunderstorm with two-moment bulk microphysics. *Journal of the Atmospheric Sciences*, **67 (1)**, 171–194.

Markowski, P., C. Hannon, J. Frame, E. Lancaster, A. Pietrycha, R. Edwards, and R. L. Thompson, 2003: Characteristics of vertical wind profiles near supercells obtained from the rapid update cycle. *Weather and forecasting*, **18 (6)**, 1262–1272.

Markowski, P., and Y. Richardson, 2011: *Mesoscale meteorology in midlatitudes*, Vol. 2. John Wiley & Sons.

Markowski, P., Y. Richardson, and G. Bryan, 2014: The origins of vortex sheets in a simulated supercell thunderstorm. *Monthly Weather Review*, **142 (11)**, 3944–3954.

Markowski, P., and Coauthors, 2012a: The pretornadic phase of the goshen county, wyoming, supercell of 5 june 2009 intercepted by vortex2. part i: Evolution of kinematic and surface thermodynamic fields. *Monthly weather review*, **140 (9)**, 2887–2915.

Markowski, P., and Coauthors, 2012b: The pretornadic phase of the goshen county, wyoming, supercell of 5 june 2009 intercepted by vortex2. part ii: Intensification of low-level rotation. *Monthly weather review*, **140 (9)**, 2916–2938.

Markowski, P. M., 2008: A comparison of the midlevel kinematic characteristics of a pair of supercell thunderstorms observed by airborne doppler radar. *Atmospheric research*, **88 (3-4)**, 314–322.

Markowski, P. M., and G. H. Bryan, 2016: Les of laminar flow in the pbl: A potential problem for convective storm simulations. *Monthly Weather Review*, **144 (5)**, 1841–1850.

Markowski, P. M., T. P. Hatlee, and Y. P. Richardson, 2018: Tornadogenesis in the 12 may 2010 supercell thunderstorm intercepted by vortex2 near clinton, oklahoma. *Monthly Weather Review*, **146 (11)**, 3623–3650.

Markowski, P. M., Y. Richardson, M. Majcen, J. Marquis, and J. Wurman, 2011: Characteristics of the wind field in three nontornadic low-level mesocyclones observed by the doppler on wheels radars. *E-Journal of Severe Storms Meteorology*, **6 (3)**.

Markowski, P. M., and Y. P. Richardson, 2009: Tornadogenesis: Our current understanding, forecasting considerations, and questions to guide future research. *Atmospheric Research*, **93 (1-3)**, 3–10.

Markowski, P. M., and Y. P. Richardson, 2014: The influence of environmental low-level shear and cold pools on tornadogenesis: Insights from idealized simulations. *Journal of the Atmospheric Sciences*, **71 (1)**, 243–275.

Markowski, P. M., and Y. P. Richardson, 2017: Large sensitivity of near-surface vertical vorticity development to heat sink location in idealized simulations of supercell-like storms. *Journal of the Atmospheric Sciences*, **74 (4)**, 1095–1104.

Markowski, P. M., J. M. Straka, and E. N. Rasmussen, 2002: Direct surface thermodynamic observations within the rear-flank downdrafts of nontornadic and tornadic supercells. *Monthly weather review*, **130 (7)**, 1692–1721.

Markowski, P. M., J. M. Straka, E. N. Rasmussen, and D. O. Blanchard, 1998: Variability of storm-relative helicity during vortex. *Monthly weather review*, **126 (11)**, 2959–2971.

May, R., S. Arms, P. Marsh, E. Bruning, and J. Leeman, 2017: Metpy: A python package for meteorological data. *Unidata, Accessed*, **31**.

Mercer, A. E., C. M. Shafer, C. A. Doswell III, L. M. Leslie, and M. B. Richman, 2012: Synoptic composites of tornadic and nontornadic outbreaks. *Monthly Weather Review*, **140 (8)**, 2590–2608.

Murdzek, S. S., E. N. Rasmussen, and M. D. Flournoy, 2018: Mobile mesonet observations near vorticity rivers in supercells. *29th Conf. on Severe Local Storms*, Stowe, VT, Amer. Meteor. Soc., P96.

Naylor, J., and M. S. Gilmore, 2012: Convective initiation in an idealized cloud model using an updraft nudging technique. *Monthly weather review*, **140 (11)**, 3699–3705.

Newton, C. W., and S. Katz, 1958: Movement of large convective rainstorms in relation to winds aloft. *Bulletin of the American Meteorological Society*, **39 (3)**, 129–136.

Nowotarski, C. J., and P. M. Markowski, 2016: Modifications to the near-storm environment induced by simulated supercell thunderstorms. *Monthly Weather Review*, **144 (1)**, 273–293.

Orf, L., R. Wilhelmson, B. Lee, C. Finley, and A. Houston, 2017: Evolution of a long-track violent tornado within a simulated supercell. *Bulletin of the American Meteorological Society*, **98 (1)**, 45–68.

Parker, M. D., 2014: Composite vortex2 supercell environments from near-storm soundings. *Monthly Weather Review*, **142 (2)**, 508–529.

Parker, M. D., and J. M. Dahl, 2015: Production of near-surface vertical vorticity by idealized downdrafts. *Monthly Weather Review*, **143 (7)**, 2795–2816.

Peters, J. M., C. J. Nowotarski, and H. Morrison, 2019: The role of vertical wind shear in modulating maximum supercell updraft velocities. *Journal of the Atmospheric Sciences*, **76 (10)**, 3169–3189.

Peters, J. M., C. J. Nowotarski, J. P. Mulholland, and R. L. Thompson, 2020: The influences of effective inflow layer streamwise vorticity and storm-relative flow on supercell updraft properties. *Journal of the Atmospheric Sciences*.

Potvin, C. K., E. M. Murillo, M. L. Flora, and D. M. Wheatley, 2017: Sensitivity of supercell simulations to initial-condition resolution. *Journal of the Atmospheric Sciences*, **74 (1)**, 5–26.

Rasmussen, E. N., 2003: Refined supercell and tornado forecast parameters. *Weather and Forecasting*, **18 (3)**, 530–535.

Rasmussen, E. N., and D. O. Blanchard, 1998: A baseline climatology of sounding-derived supercell andtornado forecast parameters. *Weather and forecasting*, **13 (4)**, 1148–1164.

Rasmussen, E. N., J. M. Straka, M. S. Gilmore, and R. Davies-Jones, 2006: A preliminary survey of rear-flank descending reflectivity cores in supercell storms. *Weather and forecasting*, **21 (6)**, 923–938.

Richardson, Y. P., K. K. Droegemeier, and R. P. Davies-Jones, 2007: The influence of horizontal environmental variability on numerically simulated convective storms. part i: Variations in vertical shear. *Monthly weather review*, **135 (10)**, 3429–3455.

Richman, M. B., 1980: Map typing patterns associated with potential urban enhanced precipitation. Ph.D. thesis, University of Illinois at Urbana-Champaign.

Roberts, B., M. Xue, A. D. Schenkman, and D. T. Dawson, 2016: The role of surface drag in tornadogenesis within an idealized supercell simulation. *Journal of the Atmospheric Sciences*, **73 (9)**, 3371–3395.

Rotunno, R., 1981: On the evolution of thunderstorm rotation. *Monthly Weather Review*, **109 (3)**, 577–586.

Rotunno, R., and J. Klemp, 1985: On the rotation and propagation of simulated supercell thunderstorms. *Journal of the Atmospheric Sciences*, **42 (3)**, 271–292.

Rotunno, R., and J. B. Klemp, 1982: The influence of the shear-induced pressure gradient on thunderstorm motion. *Monthly Weather Review*, **110 (2)**, 136–151.

Rotunno, R., J. B. Klemp, and M. L. Weisman, 1988: A theory for strong, long-lived squall lines. *Journal of the Atmospheric Sciences*, **45 (3)**, 463–485.

Rotunno, R., P. M. Markowski, and G. H. Bryan, 2017: "near ground" vertical vorticity in supercell thunderstorm models. *Journal of the Atmospheric Sciences*, **74 (6)**, 1757–1766.

Schaefer, J. T., and C. A. I. Doswell, 1984: Empirical orthogonal function expansion applied to progressive tornado outbreaks. *Journal of the Meteorological Society of Japan. Ser. II*, **62 (6)**, 929–936.

Schenkman, A., M. Xue, and M. Hu, 2014: Tornadogenesis within numerically simulated 8 may 2003 oklahoma city tornadic supercell storm. *J. Atmos. Sci*, **71**, 130–154.

Schueth, A., and C. C. Weiss, 2018: Comparing observations and simulations of the streamwise vorticity current in a tornadic supercell storm. *29th Conf. on Severe Local Storms*, Stowe, VT, Amer. Meteor. Soc., 3B.6.

Stensrud, D. J., M. C. Coniglio, R. P. Davies-Jones, and J. S. Evans, 2005: Comments on "'a theory for strong long-lived squall lines' revisited". *Journal of the Atmospheric Sciences*, **62 (8)**, 2989–2996.

Thompson, R. L., and R. Edwards, 2000: An overview of environmental conditions and forecast implications of the 3 may 1999 tornado outbreak. *Weather and forecasting*, **15 (6)**, 682–699.

Thompson, R. L., R. Edwards, J. A. Hart, K. L. Elmore, and P. Markowski, 2003: Close proximity soundings within supercell environments obtained from the rapid update cycle. *Weather and Forecasting*, **18 (6)**, 1243–1261.

Thompson, R. L., C. M. Mead, and R. Edwards, 2007: Effective storm-relative helicity and bulk shear in supercell thunderstorm environments. *Weather and forecasting*, **22 (1)**, 102–115.

Trapp, R., E. Mitchell, G. Tipton, D. Effertz, A. Watson, D. Andra Jr, and M. Magsig, 1999: Descending and nondescending tornadic vortex signatures detected by wsr-88ds. *Weather and forecasting*, **14 (5)**, 625–639.

Wade, A. R., M. C. Coniglio, and C. L. Ziegler, 2018: Comparison of near-and far-field supercell inflow environments using radiosonde observations. *Monthly Weather Review*, **146 (8)**, 2403–2415.

Wakimoto, R. M., and H. Cai, 2000: Analysis of a nontornadic storm during vortex 95. *Monthly weather review*, **128 (3)**, 565–592.

Weisman, M. L., and J. B. Klemp, 1982: The dependence of numerically simulated convective storms on vertical wind shear and buoyancy. *Monthly Weather Review*, **110 (6)**, 504–520.

Weisman, M. L., and J. B. Klemp, 1984: The structure and classification of numerically simulated convective stormsin directionally varying wind shears. *Monthly Weather Review*, **112 (12)**, 2479–2498.

Weisman, M. L., and R. Rotunno, 2000: The use of vertical wind shear versus helicity in interpreting supercell dynamics. *Journal of the atmospheric sciences*, **57 (9)**, 1452–1472.

Wicker, L. J., and R. B. Wilhelmson, 1995: Simulation and analysis of tornado development and decay within a three-dimensional supercell thunderstorm. *Journal of the atmospheric sciences*, **52 (15)**, 2675–2703.

Wurman, J., D. Dowell, Y. Richardson, P. Markowski, E. Rasmussen, D. Burgess, L. Wicker, and H. B. Bluestein, 2012: The second verification of the origins of rotation in tornadoes experiment: Vortex2. *Bulletin of the American Meteorological Society*, **93 (8)**, 1147–1170.

Xue, M., 2000: Density currents in two-layer shear flows. *Quarterly Journal of the Royal Meteorological Society*, **126 (565)**, 1301–1320.

Ziegler, C. L., 1985: Retrieval of thermal and microphysical variables in observed convective storms. part 1: Model development and preliminary testing. *Journal of the atmospheric sciences*, **42 (14)**, 1487–1509.

Ziegler, C. L., E. R. Mansell, J. M. Straka, D. R. MacGorman, and D. W. Burgess, 2010: The impact of spatial variations of low-level stability on the life cycle of a simulated supercell storm. *Monthly weather review*, **138 (5)**, 1738–1766.